

---


Electronic Theses and Dissertations, 2004-2019

---

2010

## Hurricane Wind Speed And Rain Rate Measurements Using The Airborne Hurricane Imaging Radiometer (hirad)

Ruba Amarin  
*University of Central Florida*

 Part of the [Electrical and Electronics Commons](#)  
Find similar works at: <https://stars.library.ucf.edu/etd>  
University of Central Florida Libraries <http://library.ucf.edu>

This Doctoral Dissertation (Open Access) is brought to you for free and open access by STARS. It has been accepted for inclusion in Electronic Theses and Dissertations, 2004-2019 by an authorized administrator of STARS. For more information, please contact [STARS@ucf.edu](mailto:STARS@ucf.edu).

---

### STARS Citation

Amarin, Ruba, "Hurricane Wind Speed And Rain Rate Measurements Using The Airborne Hurricane Imaging Radiometer (hirad)" (2010). *Electronic Theses and Dissertations, 2004-2019*. 4223.  
<https://stars.library.ucf.edu/etd/4223>

**HURRICANE WIND SPEED AND RAIN RATE MEASUREMENTS USING THE  
AIRBORNE HURRICANE IMAGING RADIOMETER (HIRAD)**

by

RUBA AKRAM AMARIN  
M.S. University of Central Florida, 2006

A dissertation submitted in partial fulfillment of the requirements  
for the degree of Doctor of Philosophy  
in the School of Electrical Engineering and Computer Science  
in the College of Engineering and Computer Science  
at the University of Central Florida  
Orlando, Florida

Spring Term  
2010

Major Professor: W. Linwood Jones

© 2010 Ruba Akram Amarin

## ABSTRACT

This dissertation presents results for an end-to-end computer simulation of a new airborne microwave remote sensor, the Hurricane Imaging Radiometer, HIRAD, which will provide improved hurricane surveillance. The emphasis of this research is the retrieval of hurricane-force wind speeds in the presence of intense rain and over long atmospheric slant path lengths that are encountered across its wide swath. Brightness temperature ( $T_b$ ) simulations are performed using a forward microwave radiative transfer model (RTM) that includes an ocean surface emissivity model at high wind speeds developed especially for HIRAD high incidence angle measurements and a rain model for the hurricane environment. Also included are realistic sources of errors (e.g., instrument NEDT, antenna pattern convolution of scene  $T_b$ , etc.), which are expected in airborne hurricane observations. Case studies are performed using 3D environmental parameters produced by numerical hurricane models for actual hurricanes. These provide realistic “nature runs” of rain, water vapor, clouds and surface winds from which simulated HIRAD  $T_b$ 's are derived for various flight tracks from a high altitude aircraft. Using these simulated HIRAD measurements, Monte Carlo retrievals of wind speed and rain rate are performed using available databases of sea surface temperatures and climatological hurricane atmospheric parameters (excluding rain) as *a priori* information. Examples of retrieved hurricane wind speed and rain rate images are presented, and comparisons of the retrieved parameters with the numerical model data are made. Statistical results are presented over a broad range of wind and rain conditions and as a function of path length over the full swath.

*I have roomed the bonds of earth that sings  
And danced the skies on laughter with silvered wings  
Of sun split clouds – done a hundred things*

*But*

*Never found as good as your heart strings  
For you who flourished blossoms of love in my heart*

*“SALEM”*

*Your beloved wife, Ruba*

... ..

*To the person who...*

*...offered up his life for me*

*...sheltered me through the rain*

*...was there to lean on*

*...was a friend was a love*

*it takes someone special to be a mom and a dad*

*DAD*

*MOM*

*Your beloved daughter, Ruba*

## **ACKNOWLEDGEMENT**

I would like to express my deep and sincere gratitude to my advisor, mentor and supporter, Dr. Linwood Jones for his understanding, encouraging and personal guidance that provided a good basis for the present dissertation. Through his vision I learned that everything is possible if I believe in my own capabilities. Thank you for making me a better and a stronger person.

I am deeply grateful to Mr. James Johnson for all his important support throughout this work and for always guiding me during my first steps into HIRAD studies. I will always remember your famous saying of having a good start with everything I do.

I warmly thank my committee members, Dr. Takis Kasparis, Dr. Parveen Wahid, Dr. Christopher Ruf, Dr. Timothy Miller and Dr. Svetla Hristova, for their guidance and advice. I would like to thank my family for their love, encouragement and support that carried me through my entire life and made me stronger each day. Also, I am thankful to my CFRSL team members for their continuous assistance.

Special thanks go to my special guardian angels Suleiman and Diala for lifting my feet when my own wings had trouble remembering how to fly.

This work was accomplished with the sponsorship of NASA and NOAA through Ms. Robbie Hood, formerly NASA and currently NOAA, and Dr. Timothy Miller, of the NASA Marshall Space Flight Center. Also, I would like to acknowledge the HIRAD development team from

Marshall Space Flight Center, University of Michigan, and NOAA's Hurricane Research Division for their technical support through the HIRAD development. I wish to acknowledge the financial support provided by the HIRAD project. This work was funded under Subcontract SUB2006-226 with the Von Braun Center for Science and Innovation, Inc., Huntsville, AL, in collaboration with NASA/Marshall Space Flight Center and NOAA in the development of the HIRAD instrument.

## TABLE OF CONTENTS

LIST OF FIGURES .....	x
LIST OF TABLES .....	xvii
LIST OF SYMBOLS/ACRONYMS .....	xviii
CHAPTER 1 : INTRODUCTION .....	19
1.1 Hurricane Surveillance.....	19
1.1.1 Stepped Frequency Microwave Radiometer.....	21
1.1.2 HIRAD.....	22
1.2 Dissertation Objectives .....	23
1.3 HIRAD Simulation Architecture .....	25
1.4 Dissertation Contents .....	28
CHAPTER 2 : RADIOMETER SYSTEM.....	30
2.1 HIRAD Aircraft Instrument.....	30
2.1.1 HIRAD Antenna .....	32
2.1.2 HIRAD Mechanical Configuration.....	34
2.2 Equivalent Pushbroom Radiometer System.....	36
2.3 Equivalent Pushbroom Phased Array .....	38
CHAPTER 3 : FORWARD MODEL SIMULATION .....	43
3.1 Oceanic Remote Sensing .....	43



3.2	Sea Surface Emissivity Model .....	45
3.3	Rain Absorption Coefficient .....	49
3.4	Hurricane Radiative Transfer Model .....	51
3.4.1	MM5 Numerical Hurricane Model Data Description .....	53
3.4.2	Simulation Geometry .....	59
3.4.3	Hurricane Atmospheric Model .....	60
3.5	Antenna Brightness Temperature .....	64
CHAPTER 4 : GEOPHYSICAL RETRIEVAL ALGORITHM.....		72
4.1	Antenna Pattern Correction.....	73
4.2	Atmospheric Treatment .....	82
4.3	HIRAD Retrieval Algorithm.....	85
CHAPTER 5 : RESULTS .....		89
5.1	Retrieved Wind Speed and Rain Rate Error Statistics.....	90
5.2	Individual Error Source Assessment.....	104
5.2.1	Perfect Retrieval.....	105
5.2.2	Imperfect Sea Surface Temperature Knowledge .....	107
5.2.3	Rain Errors .....	109
5.2.4	Imperfect Atmosphere Parameter Knowledge.....	111
5.2.5	Antenna Pattern Correction Errors.....	113

5.2.6	Random Errors .....	115
CHAPTER 6 : CONCLUSION.....		118
6.1	Summary and Conclusion.....	118
6.2	Future Work.....	120
APPENDIX A. SYNTHETIC THINNED ARRAY RADIOMETER (STAR) .....		122
A.1	Aperture Taper and Pattern Shaping.....	122
A.2	Image Reconstruction Simulations .....	124
APPENDIX B. PLANAR ARRAY.....		129
APPENDIX C. CFRSL EMISSIVITY MODEL FIGURES.....		141
APPENDIX D. RADTB MICROWAVE RADIATIVE TRANSFER MODEL .....		143
APPENDIX E. RESULTS .....		146
REFERENCES .....		170

## LIST OF FIGURES

Figure 1.1 HIRAD provides wide swath imaging of hurricane surface wind and rain rate. ....	23
Figure 1.2 HIRAD top-level end-to-end simulation. ....	26
Figure 1.3 Simulation of HIRAD $T_b$ measurements. ....	27
Figure 1.4 HIRAD retrieval algorithm block diagram. ....	28
Figure 2.1 Block diagram of the HIRAD aircraft instrument. ....	31
Figure 2.2 (a) Schematic of HIRAD array with active elements shown in black, (b) Cross-sectional sketch of stacked-patch antenna (not drawn to scale). ....	33
Figure 2.3 HIRAD array antenna (back side) and MIC receivers during integration and test. ....	35
Figure 2.4 HIRAD in the flight pallet. ....	35
Figure 2.5 Equivalent real-aperture pushbroom radiometer system with 41 beams cross-track. .	36
Figure 2.6 Co-Pol patterns at 6.6 GHz frequency for 0 deg and 60 deg scan beams. Panel - a shows wide-angle patterns and panel -b shows expanded main beam patterns. ....	39
Figure 2.7 X-Pol patterns at 6.6 GHz frequency for 0 deg and 60 deg scan beams. Panel - a shows wide-angle patterns and panel -b shows expanded main beam patterns. ....	40
Figure 2.8 HIRAD squared beam pattern and phased array tapered beam patterns at 0 and 60 deg for 6.6 GHz. ....	42
Figure 3.1 Brightness temperature signal as seen by an airborne radiometer. ....	44
Figure 3.2 The CFRSL ocean surface emissivity model for SST = 300 Kelvin: (a) horizontal and (b) vertical polarization at 4 GHz and wind speeds of 6, 20, 40 and 70 m/s from El-Nimri et al., 2010 [10]. ....	48
Figure 3.3 Rain absorption coefficients for HIRAD frequencies. ....	50

Figure 3.4 Rain transmissivity for a typical 5 km rain height for (a) Nadir-viewing, and (b) 60 deg-viewing.....	51
Figure 3.5 Forward (RadTb) atmospheric model. ....	52
Figure 3.6 Hurricane Frances surface fields at hour 20 on 31 August, 2004 for: (a) wind field (m/s) and (b) rain rate field (mm/hr).....	55
Figure 3.7 Hurricane Frances 2D slices of: (a) rain in mm/hr, (b) cloud liquid water in gm/m <sup>3</sup> and (c) water vapor in gm/m <sup>3</sup> . ....	57
Figure 3.8 Sea surface temperature field in Celsius. ....	58
Figure 3.9 HIRAD 3dB footprint on the ocean surface. Note that this figure distorts the slightly elliptical IFOV because of the different axis scales.....	60
Figure 3.10 Example: forward radiative transfer model simulation for rain rate. ....	61
Figure 3.11 Frances wind field (m/s) with three HIRAD cross-track scans 1, 2 and 3 indicated. ....	62
Figure 3.12 Simulated cross-track brightness temperature scenes for (a) scan 1 in the eyewall region, (b) scan2 is through the center of the eye and (c) scan 3 is taken at the outer edge of the eyewall region. Left-hand panels are H-Pol and right-hand are V-Pol.....	63
Figure 3.13 Apparent temperature distribution [9].....	64
Figure 3.14 Co-Pol zero boresight pattern beam efficiency for (a) 4 GHz (b) 5 GHz (c) 6 GHz and (d) 6.6 GHz with the red cross identifying the first null beam efficiency. ....	66
Figure 3.15 Integrated X-Pol brightness fraction ( $\gamma$ ).....	68
Figure 3.16 Co-Pol and X-Pol patterns at Nadir (left panel) and 60 deg (right panel) beam positions for (a) 4 GHz and (b) 6.6 GHz. ....	69

Figure 3.17 Comparison between $T_A$ (solid line) and $T_{\text{aph}}$ (dashed line) at all frequencies for (a) scan 1, (b) scan 2 and (c) scan 3. ....	71
Figure 4.1 HIRAD retrieval algorithm block diagram.....	73
Figure 4.2 Correlation of $T_A$ and $T_{\text{bVconv}}$ brightness temperatures for 4 GHz (left panel) and 6.6 GHz (right panel) for (a) Nadir, (b) $\pm 30$ deg and (c) $\pm 60$ deg. The color-bar refers to the integrated RR values in km-mm/hr.....	75
Figure 4.3 Main-lobe and side-lobe contributions to the antenna temperature $T_A$ [9]. ....	76
Figure 4.4 Antenna sidelobe brightness contributions above the antenna boresight for 4 GHz (left panel) and 6.6 GHz (right panel) for (a) Nadir, (b) $\pm 30$ deg and (c) $\pm 60$ deg. The color-bar refers to the integrated rain rate km-mm/hr. ....	78
Figure 4.5 Antenna sidelobe brightness contributions below the antenna boresight for 4 GHz (left panel) and 6.6 GHz (right panel) for (a) Nadir, (b) $\pm 30$ deg and (c) $\pm 60$ deg. The color-bar refers to the integrated rain rate values km-mm/hr. ....	79
Figure 4.6 Comparison between $T_{\text{corr}}$ (solid line) and $T_{\text{aph}}$ (dashed line) at all frequencies for cross-track brightness temperature scenes(a) scan 1, (b) scan 2 and (c) scan 3. ....	81
Figure 4.7 Retrieval radiative transfer model for calculating rain emission.....	82
Figure 4.8 Hurricane atmosphere climatology (a) Clouds and (b) water vapor absorption coefficient profiles in Np/km averaged in 5 km annuli rings. ....	84
Figure 4.9 Retrieved wind speed (left panel) and rain rates (right panel) for (a) scan 1, (b) scan 2, and (c) scan 3. ....	87
Figure 5.1 Frances simulated wind measurements for three Fig-4's.....	91

Figure 5.2 Nature run (a) wind speed (m/s) and (b) integrated rain rate (km-mm/hr) for Leg 1 (left panel) and Leg 2 (right panel).....	92
Figure 5.3 Scatter plot comparisons for (a) wind speed and (b) rain rate for eight legs.....	94
Figure 5.4 Histograms of the differences in (a) wind speed and (b) rain rate for eight legs. ....	95
Figure 5.5 RMS retrieved wind speed errors (m/s) for (a) Leg 1 and (b) Leg 2.....	97
Figure 5.6 RMS retrieved integrated rain rate errors (%) for (a) Leg 1 and (b) Leg 2.....	97
Figure 5.7 RMS retrieved wind speed error surfaces (m/s) for (a) Nadir (b) $\pm 30$ deg and (c) $\pm 60$ deg.....	100
Figure 5.8 RMS wind speed errors (m/s) at Nadir for four wind speed bins $\pm 5$ m/s.....	102
Figure 5.9 RMS wind speed errors (m/s) at $\pm 30$ deg for four wind speed bins $\pm 5$ m/s.....	103
Figure 5.10 RMS wind speed errors (m/s) at $\pm 60$ deg for four wind speed bins $\pm 5$ m/s.....	104
Figure 5.11 For Frances Leg 1 (a) Surface wind field (m/s) and (b) RMS wind speed errors (m/s). .....	106
Figure 5.12 For Frances Leg 1 (a) Surface wind field (m/s), (b) relative SST difference (Celsius), (c) correlation between RMS wind speed errors and differences in SST and (d) RMS wind speed errors (m/s).....	108
Figure 5.13 For Frances Leg 1 (a) Surface wind field (m/s), (b) integrated rain rate (km-mm/hr) and (c) RMS wind speed errors (m/s). ....	110
Figure 5.14 For Frances Leg 1 (a) Surface wind field (m/s) and (b) RMS wind speed errors (m/s). .....	112
Figure 5.15 For Frances Leg 1 (a) Surface wind field (m/s) and (b) RMS wind speed errors (m/s). .....	114

Figure 5.16 For Frances Leg 1 (a) Surface wind field (m/s) and (b) RMS wind speed errors (m/s). .....	116
Figure. A.1 Synthesized antenna patterns for uniform, triangular and Blackman tapers at 6.6 GHz. ....	124
Figure. A.2 Frances wind field (m/s), HR 24, 31 August, 2004. ....	125
Figure. A.3 $T_b$ profiles at 4 and 6.6 GHz for (a) scan 1, (b) scan 2 and (c) scan 3. ....	127
Figure. B.1 Planar array geometry. ....	129
Figure. B.2 Co-Pol and X-Pol composite element patterns at (a) 4 GHz, (b) 5 GHz, (c) 6 GHz and (d) 6.6 GHz. ....	133
Figure. B.3 Co-Pol patterns at 4 and 6.6 GHz frequencies for (a) 0 deg and 60 deg scan beams and (b) zoomed portion of the main beam. ....	135
Figure. B.4 X-Pol patterns at 4 and 6.6 GHz frequencies for (a) 0 deg and 60 deg scan beams and (b) zoomed portion of the main beam. ....	136
Figure. B.5 Co-Pol uniform and tapered patterns at 6.6 GHz frequency for (a) 0 deg and 60 deg scan beams and (b) zoomed portion of the main beam. ....	139
Figure. B.6 X-Pol uniform and tapered patterns at 6.6 GHz frequency for (a) 0 deg and 60 deg scan beams and (b) zoomed portion of the main beam. ....	140
Figure. C.1 The CFRSL ocean surface emissivity model for SST = 300 Kelvin: (a) horizontal and (b) vertical polarization at all frequencies and wind speeds of 6, 20, 40 and 70 m/s from El-Nimri et al., 2010. ....	142
Figure. D.1 HIRAD radiative transfer model. ....	144

Figure. E.1 Scatter plot comparisons for wind speed (left panel) and rain rate (right panel) for random error (a) 1 Kelvin, (b) 2 Kelvin, (c) 4 Kelvin and (d) 8 Kelvin.....	148
Figure. E.2 Histograms of the differences in wind speed (left panel) and rain rate (right panel) for random error (a) 1 Kelvin, (b) 2 Kelvin, (c) 4 Kelvin and (d) 8 Kelvin.....	151
Figure. E.3 RMS retrieved wind speed errors for Leg 1 (left panel) and Leg 2 (right panel) for random error (a) 1 Kelvin, (b) 2 Kelvin, (c) 4 Kelvin and (d) 8 Kelvin.....	153
Figure. E.4 RMS retrieved wind speed error surfaces at Nadir for random error (a) 1 Kelvin, (b) 2 Kelvin, (c) 4 Kelvin and (d) 8 Kelvin.....	154
Figure. E.5 RMS wind speed errors (m/s) at Nadir for four wind speed bins $\pm 5$ m/s for 1 Kelvin random error.....	155
Figure. E.6 RMS wind speed errors (m/s) at Nadir for four wind speed bins $\pm 5$ m/s for 2 Kelvin random error.....	156
Figure. E.7 RMS wind speed errors (m/s) at Nadir for four wind speed bins $\pm 5$ m/s for 4 Kelvin random error.....	157
Figure. E.8 RMS wind speed errors (m/s) at Nadir for four wind speed bins $\pm 5$ m/s for 8 Kelvin random error.....	158
Figure. E.9 RMS retrieved wind speed error surfaces at $\pm 30$ deg for random error (a) 1 Kelvin, (b) 2 Kelvin, (c) 4 Kelvin and (d) 8 Kelvin. ....	159
Figure. E.10 RMS wind speed errors (m/s) at $\pm 30$ deg for four wind speed bins $\pm 5$ m/s for 1 Kelvin random error.....	161
Figure. E.11 RMS wind speed errors (m/s) at $\pm 30$ deg for four wind speed bins $\pm 5$ m/s for 2 Kelvin random error.....	162



Figure. E.12 RMS wind speed errors (m/s) at $\pm 30$ deg for four wind speed bins $\pm 5$ m/s for 4 Kelvin random error.....	163
Figure. E.13 RMS wind speed errors (m/s) at $\pm 30$ deg for four wind speed bins $\pm 5$ m/s for 8 Kelvin random error.....	164
Figure. E.14 RMS retrieved wind speed error surfaces at $\pm 60$ deg for random error (a) 1 Kelvin, (b) 2 Kelvin, (c) 4 Kelvin and (d) 8 Kelvin. ....	165
Figure. E.15 RMS wind speed errors (m/s) at $\pm 60$ deg for four wind speed bins $\pm 5$ m/s for 1 Kelvin random error.....	166
Figure. E.16 RMS wind speed errors (m/s) at $\pm 60$ deg for four wind speed bins $\pm 5$ m/s for 2 Kelvin random error.....	167
Figure. E.17 RMS wind speed errors (m/s) at $\pm 60$ deg for four wind speed bins $\pm 5$ m/s for 4 Kelvin random error.....	168
Figure. E.18 RMS wind speed errors (m/s) at $\pm 60$ deg for four wind speed bins $\pm 5$ m/s for 8 Kelvin random error.....	169

## LIST OF TABLES

Table 2.1 Comparison of phased array and HIRAD synthesized beams .....	41
Table 3.1 Atmospheric parameters .....	54
Table 5.1 Error Statistics for All Cases .....	98
Table. B.1 Number of cross-track elements at each frequency .....	131
Table. B.2 m and n values at each frequency .....	134
Table. B.3 Co-Pol 0 deg and 60 deg beam scan patterns' characteristics .....	137

## LIST OF SYMBOLS/ACRONYMS

CFRSL	Central Florida Remote Sensing Lab
NASA	National Aeronautics and Space Administration
MSFC	Marshall Space Flight Center
HIRAD	Hurricane Imaging Radiometer
NOAA	National Oceanic and Atmospheric Administration
HRD	Hurricane Research Division
SFMR	Stepped Frequency Microwave Radiometer
GPS	Global Positioning System
STAR	Synthetic Thinned Array Radiometry
RTM	Radiative Transfer Model
MIC	Microwave Integrated Circuit
IFOV	Instantaneous Field of View
RadTb	CFRSL Radiative Transfer Model
EIA	Earth Incidence Angle
TMI	TRMM Microwave Imager
TRMM	Tropical Rainfall Measuring Mission
NSSTC	National Space Science and Technology Center

## **CHAPTER 1 : INTRODUCTION**

The Central Florida Remote Sensing Laboratory, CFRSL, of the School of Electrical Engineering and Computer Science at the University of Central Florida is engaged in research to improve microwave remote sensing techniques for inferring ocean and atmospheric geophysical parameters. A major thrust of this research is technology development for the remote sensing of ocean surface wind speed and rain rate in hurricanes. This effort, under the sponsorship of the National Aeronautics and Space Administration (NASA) Marshall Space Flight Center (MSFC), is to develop the next-generation airborne remote sensor known as the Hurricane Imaging Radiometer (HIRAD) for providing real-time hurricane surveillance for scientific and operational applications. This development is a partnership with NASA MSFC and the National Oceanic and Atmospheric Administration (NOAA) Hurricane Research Division (HRD) and the University of Michigan's Space Physics Research Laboratory and the CFRSL at the University of Central Florida.

### **1.1 Hurricane Surveillance**

Hurricanes have caused more destruction in the United States than any other type of natural disaster, and according to the NOAA National Hurricane Center, the 2005 season was the worst on record, dating from 1851. Twenty seven tropical storms formed and 15 became hurricanes, breaking the old records of 21 tropical storms in 1933 and 12 hurricanes in 1969. Seven of the hurricanes developed to category 3 or higher, and for the first time in a single season, three reached category 5 (Katrina, Rita, and Wilma).

The best way to minimize the social and financial impact of hurricanes is through preparedness, which relies on monitoring storms and improved numerical weather forecasting to predict their growth and movement as they develop and make landfall. The monitoring of storms is accomplished through a variety of remote sensing and in situ measurement techniques. Primarily geostationary satellites with visible and infrared imagery are used to fix the eye location and make surface winds intensity estimates using the Dvorak technique.

Also, when a hurricane is within 24 hrs of making landfall in the continental United States, aircraft flights are made about every 3 hours to geo-locate the eye, measure central pressure, and estimate the maximum sustained surface wind speed. Surface wind estimates are the most important because they are used to classify the intensity of the hurricane, and presently, the airborne Stepped Frequency Microwave Radiometer (SFMR) a nadir looking remote sensor is the state-of-the-art for providing measurements of ocean wind speed and rain rate in real-time during hurricane surveillance flights.

Because the hurricane warnings are based upon the one-minute max sustained surface wind speed, this measurement is of critical importance to NOAA National Hurricane Center's forecasters. The Stepped Frequency Microwave Radiometer (SFMR) has been making these measurements for many years, flying through storms on the NOAA WP-3 aircraft. Calibration of the SFMR in wind speed by collocated comparisons to in-situ wind measurements during the 1998, 1999, and 2001 hurricane seasons has established its reliability as a data source for hurricane research [1].

### 1.1.1 Stepped Frequency Microwave Radiometer

The SFMR uses a nadir-viewing antenna and receiver to measure radio emission (brightness temperature) from the sea surface at six C-band frequencies (4.7 – 7.1 GHz). From these data, surface wind speed and columnar rain rate are simultaneously retrieved using a statistical regression algorithm.

The first SFMR measurements were made from the NOAA Hurricane Research Division (HRD) WC-130 aircraft in Hurricane Allen in 1980 as reported by Jones et al. (1981) [2] and Black and Swift (1984) [3]. Since 1984, surface wind speeds in hurricanes have been routinely monitored using the SFMR on-board the NOAA HRD WP-3D aircraft as described by Uhlhorn and Black (2003) [1]. Further, during the 2008 hurricane season, SFMR became an operational sensor on the US Air Force Reserve 53rd Weather Squadron's C-130 hurricane reconnaissance aircraft for operational tasking by the National Hurricane Center.

Uhlhorn et al. (2007) [4] used Global Positioning System (GPS) dropwindsonde information collected during the active 2005 Atlantic hurricane season to validate the SFMR ocean wind speed retrieval quality over the entire range of expected hurricane wind speeds up to 85 m/s (Saffir-Simpson category 5). They found the operational SFMR ocean wind speed retrieval was within 4 m/s RMS of the dropwindsonde-estimated surface wind speed and within 5 m/s of the aircraft flight-level wind speed measurement extrapolated to 10 m height. Based upon this evaluation SFMR has become the “gold standard” for surface wind speed measurements in hurricanes.

### 1.1.2 HIRAD

In the next decade, a new C-band instrument known as the Hurricane Imaging Radiometer (HIRAD) will likely replace the SFMR [5] as the operational hurricane remote sensor. HIRAD improves over the SFMR by imaging surface wind speed and rain rate over a  $\pm 60$  deg swath, which is approximately equal to three times the aircraft altitude. It will be compatible with high altitude aircraft and unpiloted aerial vehicles and even has potential for future satellite operation.

HIRAD is a hybrid instrument design in the sense that it is a stepped frequency design similar to SFMR plus a Fourier synthesis imager similar to the Lightweight Rainfall Radiometer (LRR). The LRR is an airborne synthetic thinned aperture radiometer that operates at the X-band frequency [6, 7] and provides cross-track imaging through Fourier synthesis software beam forming. HIRAD will widen the restricted, nadir-only coverage of SFMR to a cross-track field of view of  $\pm 60$  deg by providing real aperture imaging along track and by synthesizing brightness temperature imaging cross-track. This technology is currently under development with the first prototype single polarization airborne instrument completed in 2010. HIRAD will provide NOAA with crucial, real time information about the maximum 1-minute sustained wind speed in the hurricane along with vital information about other hurricane meteorological structures. The key to HIRAD's improved performance is its ability to operate as a Fourier synthesis imager at four discrete frequencies (4, 5, 6 and 6.6 GHz) that cover approximately the same C-band octave as the SFMR. Figure 1.1 illustrates the HIRAD measurement swath from an unmanned Global Hawk aircraft.

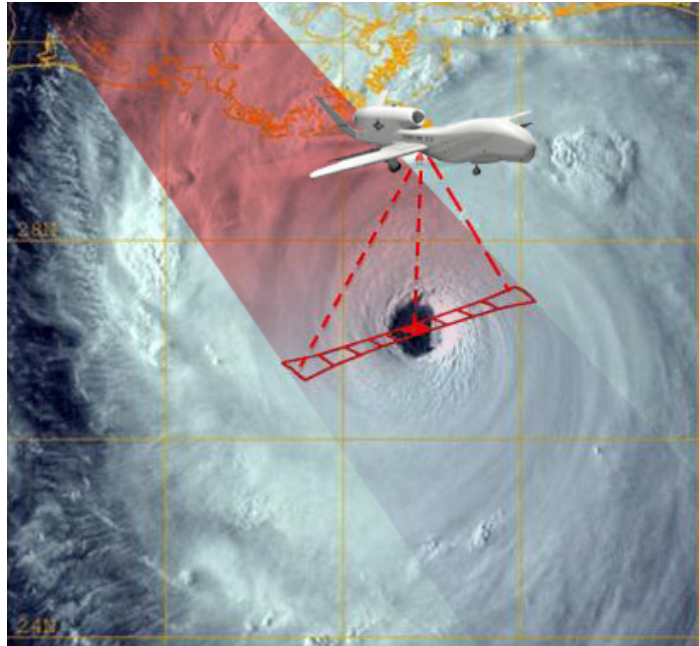


**Figure 1.1 HIRAD provides wide swath imaging of hurricane surface wind and rain rate.**

## 1.2 Dissertation Objectives

This dissertation deals with the remote sensing of wind speed and rain rate in hurricanes, which directly supports the HIRAD instrument development. Through the use of realistic simulations of hurricane surveillance flights over ocean, we are able to predict the wind speed measurement performance of a conceptual pushbroom wide-band radiometer system that has strong similarities with HIRAD. The goal of this research is to use this simulation to characterize the HIRAD hurricane surface wind speed measurement accuracy as a function of wind speed, rain rate and cross-swath location (incidence angle). In this dissertation, we will use proven methods of microwave radiometer measurement modeling in a Monte Carlo simulation to predict



wind speed retrieval errors parametrically with instrument characteristics. In this manner our results are somewhat generic and may be applied to a number of instrument designs including, but not just limited to, HIRAD.

On the other hand, our approach of using a real aperture scanning phased array antenna to produce multiple antenna beams in a pushbroom configuration for wide-swath surface sampling is different from HIRAD that uses synthetic thinned array radiometry (STAR) [8] to synthesize a brightness temperature scene. For the HIRAD project, the image reconstruction algorithm is under development at the University of Michigan and is not available for use in this simulation. Thus, our approach of using a pushbroom radiometer system has the advantage of simplicity of the simulation, which employs well proven microwave radiometry techniques [9]. While the results of our simulation are directly applicable to the HIRAD performance, unfortunately, they do NOT include synthetic aperture radiometry image reconstruction errors. Nevertheless, based upon our experience with STAR image reconstruction, we believe that our antenna pattern correction algorithm used in the wind speed retrieval introduces  $T_b$  errors that are representative of those in the HIRAD image reconstruction. A brief discussion of image reconstruction, including a simplified error analysis, is presented in Appendix A.

Finally, the results of this dissertation will be very beneficial for conducting future flight campaigns (e.g., the 2010 NASA GRIP hurricane field program). HIRAD inversion (wind speed and rain rate retrieval) algorithms don't currently exist except in concept; however, much of this dissertation can be applied to the development and optimization of these algorithms as part of the early flight program. Advances in radiative transfer modeling (RTM) for ocean emissivity in

hurricanes at high incidence angles have been developed at CFRSL to support HIRAD [10]. Examples of retrieved hurricane wind speed and rain rate images are presented in this dissertation (Chapters 4 and 5), and comparisons of the retrieved parameters with the numerical hurricane model data are made. Statistical results are presented over a broad range of wind and rain conditions and as a function of path length over the full swath (Chapter 5).

### 1.3 HIRAD Simulation Architecture

This section presents the HIRAD simulation architecture by describing the key elements in the HIRAD forward model, the retrieval algorithm, and the end-to-end simulation that has been developed for hurricane wind speed and rain rate measurement performance evaluation. Figure 1.2 shows the top level simulation diagram where the HIRAD  $T_b$  measurements from the “Nature Runs” (surface wind and rain fields) are computed and used in the retrieval algorithm to infer both wind speed and rain rate. A comparison between the retrieved results and nature runs are statistically analyzed to determine differences (errors), which are characterized as a function of the mean nature run wind speed and rain rate and as a function of cross-track location (incidence angle).

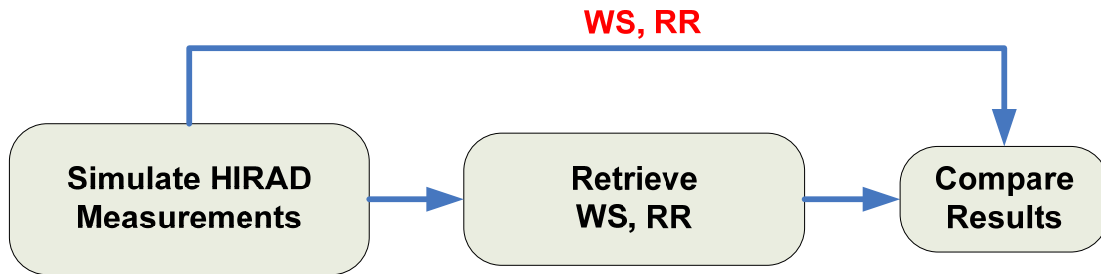


**Figure 1.2 HIRAD top-level end-to-end simulation.**

A more detailed block diagram for “simulating the HIRAD measurements” is given in Fig. 1.3. The first step is performing the geometry module calculations, where the HIRAD pushbroom antenna beams lines-of-sight and surface footprints are calculated. As part of the forward radiative transfer model (RTM), several numerical hurricane model runs are used that provide realistic 3D environmental parameters (rain, water vapor, clouds, temperature and surface winds) from which simulated HIRAD  $T_b$ 's are derived for typical flight tracks from the Global Hawk operating at 20 km altitude. The RTM includes the SFMR rain model for the hurricane environment and an ocean surface emissivity model developed especially for HIRAD high incidence angle measurements [10]. A detailed description is provided in Chapter 3. Also included in the simulation is antenna pattern convolution of the scene  $T_b$ .

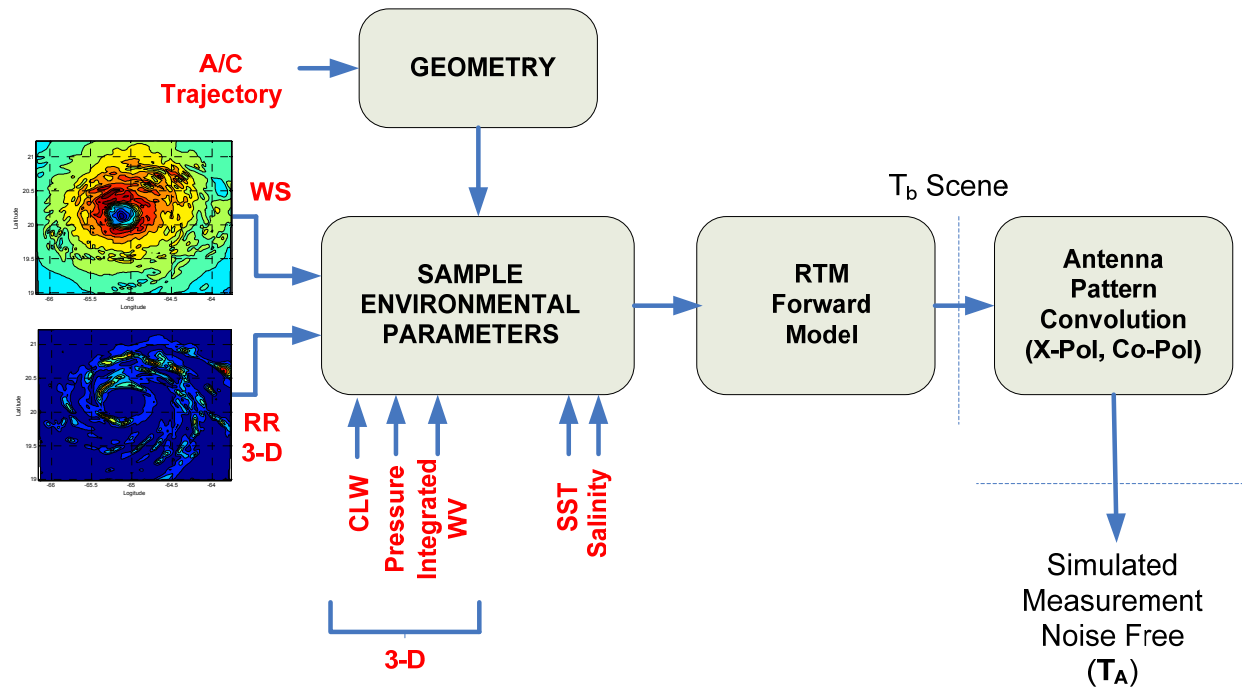


Figure 1.3 Simulation of HIRAD  $T_b$  measurements.

In the HIRAD retrieval algorithm, a different RTM is used with environmental parameters available from independent climatology and data bases parametrically to compute a theoretical modeled brightness temperature matrix over a wide range of possible wind speed, rain rate and incidence angles for the four HIRAD frequencies. The retrieved ocean surface wind speed and rain rate are estimated using the statistical least-squares difference method. In this procedure, the wind speed and rain rate that minimize the difference between the simulated HIRAD  $T_b$  measurements and modeled apparent brightness temperatures across all HIRAD frequencies. Realistic sources of random errors, which are expected in hurricane observations, are added to the simulated HIRAD measurements and the retrievals are performed using a Monte Carlo simulation. The retrieval algorithm is performed using independent available databases of sea

surface temperatures and climatological hurricane atmospheric parameters (excluding rain) as *a priori* information. The retrieval algorithm process is described in Fig. 1.4, and a detailed description of the retrieval algorithm process is provided in Chapter 4 of this dissertation.

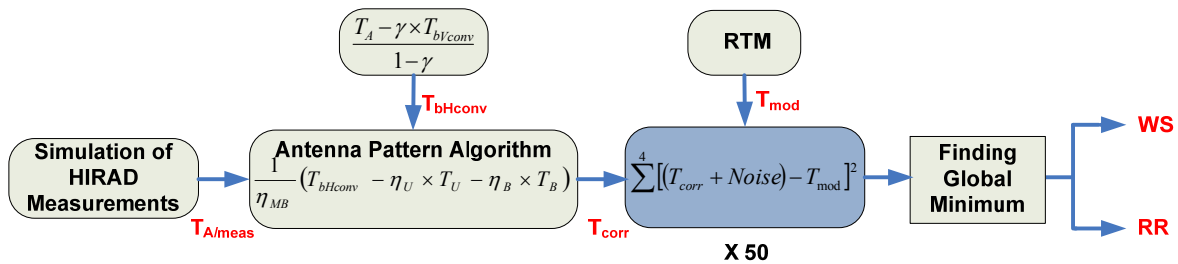


Figure 1.4 HIRAD retrieval algorithm block diagram.

#### 1.4 Dissertation Contents

Chapter 1 provides the description of the dissertation objectives and a brief overview of airborne hurricane surveillance and the HIRAD end-to-end simulation. Chapter 2 describes a conceptual pushbroom radiometer system, which is equivalent to HIRAD. The forward microwave radiative transfer model for hurricanes is presented in Chapter 3, which includes the surface wind speed and atmosphere modeling in addition to the antenna  $T_b$  description. Chapter 4 describes the geophysical HIRAD retrieval algorithm along with detailed results of model validation and sample retrieved wind speed and rain rate results. This chapter also presents the antenna pattern correction algorithm and discusses the different error sources accounted for in the simulation. Extensive simulation results are presented for hurricane Frances in Chapter 5.

Finally, conclusions and recommendations for future studies are presented in Chapter 6. Also, several appendices are provided to give detailed information on several related topics.

## CHAPTER 2 : RADIOMETER SYSTEM

Chapter 2 describes the HIRAD instrument and the simulated hardware configuration of a conceptual pushbroom wide-band radiometer system that is radiometrically equivalent with HIRAD. We begin with a brief description of the HIRAD aircraft instrument (including the array antenna) and then present a comparison between the pushbroom phased array designs that produce the individual beam patterns that are similar to the synthesized beams for HIRAD.

### 2.1 HIRAD Aircraft Instrument

HIRAD is an airborne Synthetic Thinned Array Radiometer (STAR) that uses a thinned planar array antenna to perform a one dimensional (1D) interferometric (cross-track) radiometric imaging of the ocean brightness scene [11]. A stacked patch array element has been designed to resonate at the discrete frequencies of 4, 5, 6 and 6.6 GHz, with  $37 \times 16$  of these elements making up the entire antenna. The planar antenna array is thinned in one dimension so that 10 linear arrays ( $1 \times 16$ ) are cross-correlated to synthesize an aperture 37 elements wide [12]. Figure 2.1 shows the HIRAD instrument block diagram.

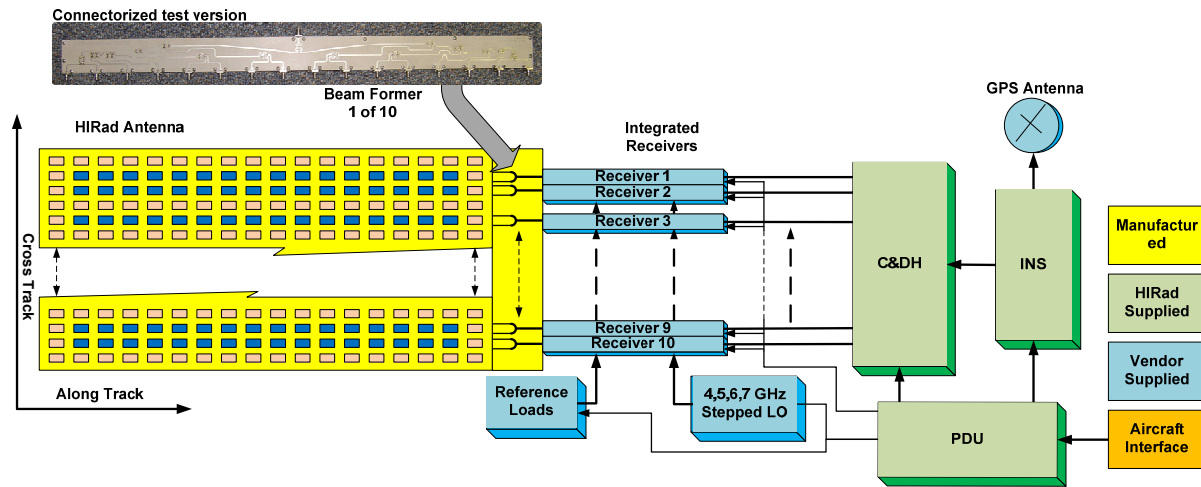


**Figure 2.1 Block diagram of the HIRAD aircraft instrument.**

The signals (blackbody noise emissions) from each of the 10 linear array elements are filtered, amplified, linearly demodulated by dedicated receivers and then digitized. These voltage signals (proportional to the received electric field intensity) are then passed to a signal processing subsystem that performs several functions. All possible pairs of the 10 radiometer signals are cross-correlated using complex multipliers to form the raw, un-calibrated, visibility samples that make up the Level-0 archival data produced by the sensor.

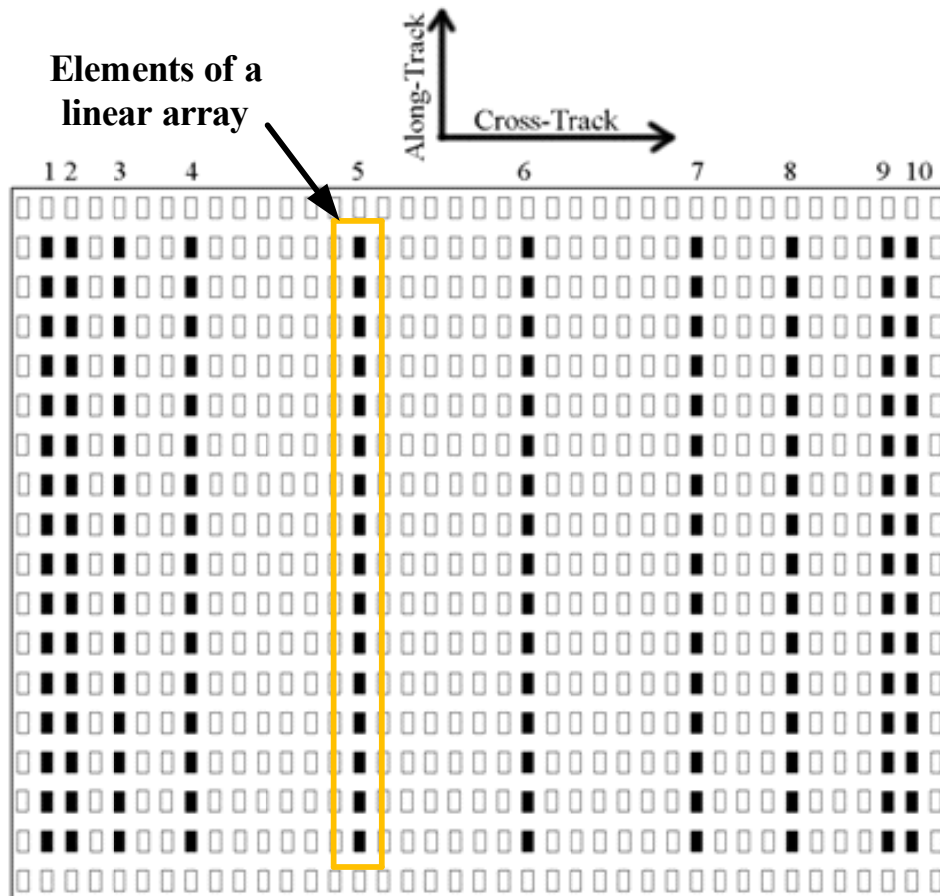
The raw visibility samples are calibrated using internal reference loads, active cold loads, and correlated noise diodes, and calibrated visibilities are converted to an image of brightness temperature ( $T_b$ ) by a least squares inversion of the individual interference patterns that are produced by the cross-correlation of each pair of antenna elements. Thus, HIRAD is a 1-dimensional synthesis pushbroom radiometric imager. Each of the ten linear array antenna elements has a coincident fan beam antenna pattern that is pointed in the nadir direction and aligned on the aircraft cross-track, which is perpendicular to the aircraft axis. The length of the



linear array element defines the along-track angular resolution of the imager, and the cross-track resolution is set by the maximum spacing between linear arrays. Individual pixels in the cross-track direction are produced simultaneously in software by the least squares inversion algorithm (see Appendix A). Pixels are formed along-track, sequentially in time, by the forward motion of the aircraft.

### 2.1.1 HIRAD Antenna

The HIRAD flight antenna has been developed using a  $0.82 \text{ m} \times 0.57 \text{ m}$ , 10 element thinned array with a stacked-patch radiating element as shown in Fig. 2.2. The element spacing in the cross-track direction is optimized to maximize spatial resolution and to limit grating lobes infringing on the field-of-view. The original design was for the highest frequency of 7 GHz. During testing, it was found that a null could occur in the main beam of the along-track pattern. For this reason, the upper frequency was reduced to 6.6 GHz. Therefore, in the final design, a spacing between elements was less than  $\lambda/2$  at 4 GHz and equal to  $\lambda/2$  at 6.6 GHz. With this design, there are no grating lobes at the highest frequency even though there is some aliasing that produces asymmetric beams at the larger incidence angles [12]. A usable field-of-view of  $\pm 60$  deg was selected based on beam broadening and increased antenna X-Pol sensitivity at larger incidence angles. From a viewing altitude of 20 km, the spatial resolution at 6.6 GHz varies between 2 ~ 4 km.



(a)

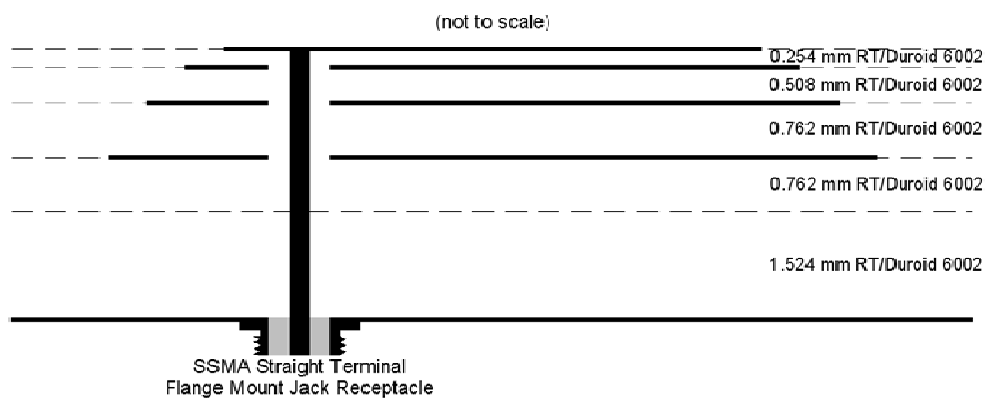
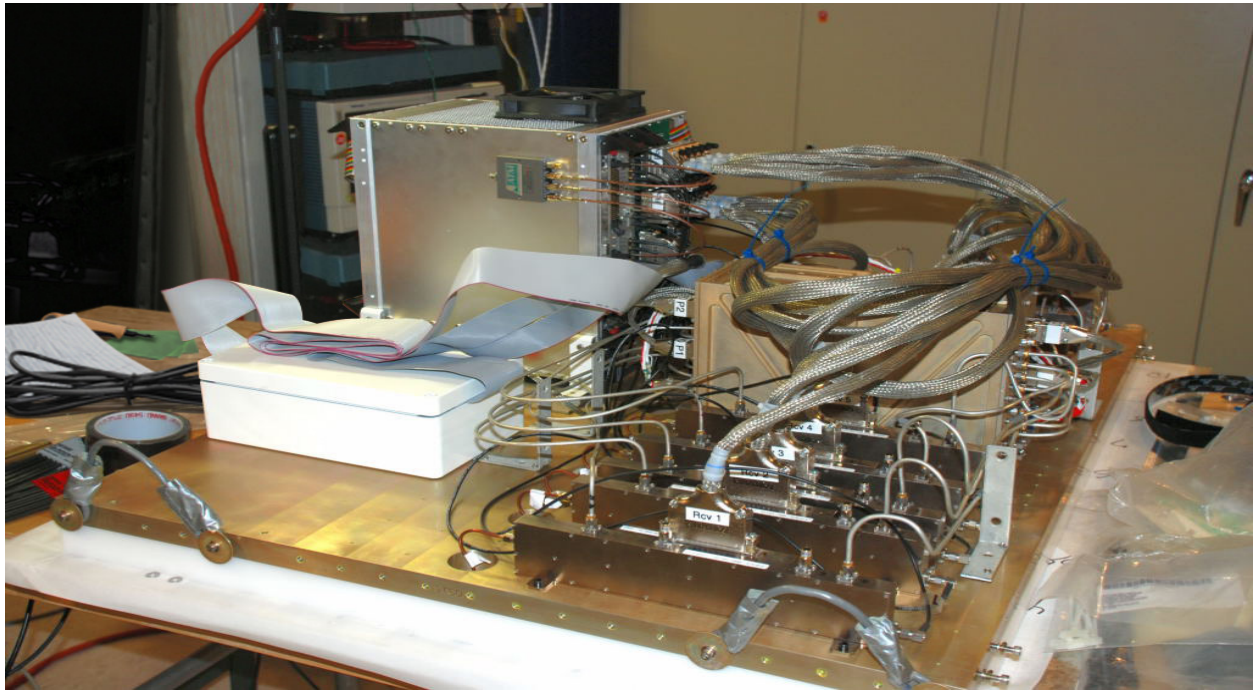


Figure 2.2 (a) Schematic of HIRAD array with active elements shown in black, (b) Cross-sectional sketch of stacked-patch antenna (not drawn to scale).

### 2.1.2 HIRAD Mechanical Configuration

A key mechanical design requirement has been to facilitate HIRAD integration onto a wide variety of aircraft in order to increase opportunities for potential hurricane aircraft missions. Thus, the electronics packaging employs microwave integrated circuit (MIC) technology for the receiver system, which reduces the instrument size by a factor of 3 and the weight by a factor of 10 over hybrid electronic modules with coaxial connectors.

The antenna array is mounted to an isogrid type substrate that will provide a self-stiffened structure in a light weight format for the array/beamformer assembly. The MIC receivers are sized to fit over the back side of the active row of antenna elements (see photo Fig. 2.3). The HIRAD instrument in the flight pallet is shown in Fig. 2.4.



**Figure 2.3 HIRAD array antenna (back side) and MIC receivers during integration and test.**



**Figure 2.4 HIRAD in the flight pallet.**

## 2.2 Equivalent Pushbroom Radiometer System

As discussed in Section 1.2, we will simulate a real aperture pushbroom radiometer equivalent of HIRAD that is illustrated in Fig. 2.5. In the simplest terms, this equivalent system replaces the HIRAD synthetic thinned array imaging with 41 individual antenna beams (with boresight spaced on 3 deg centers  $\pm 60$  deg).

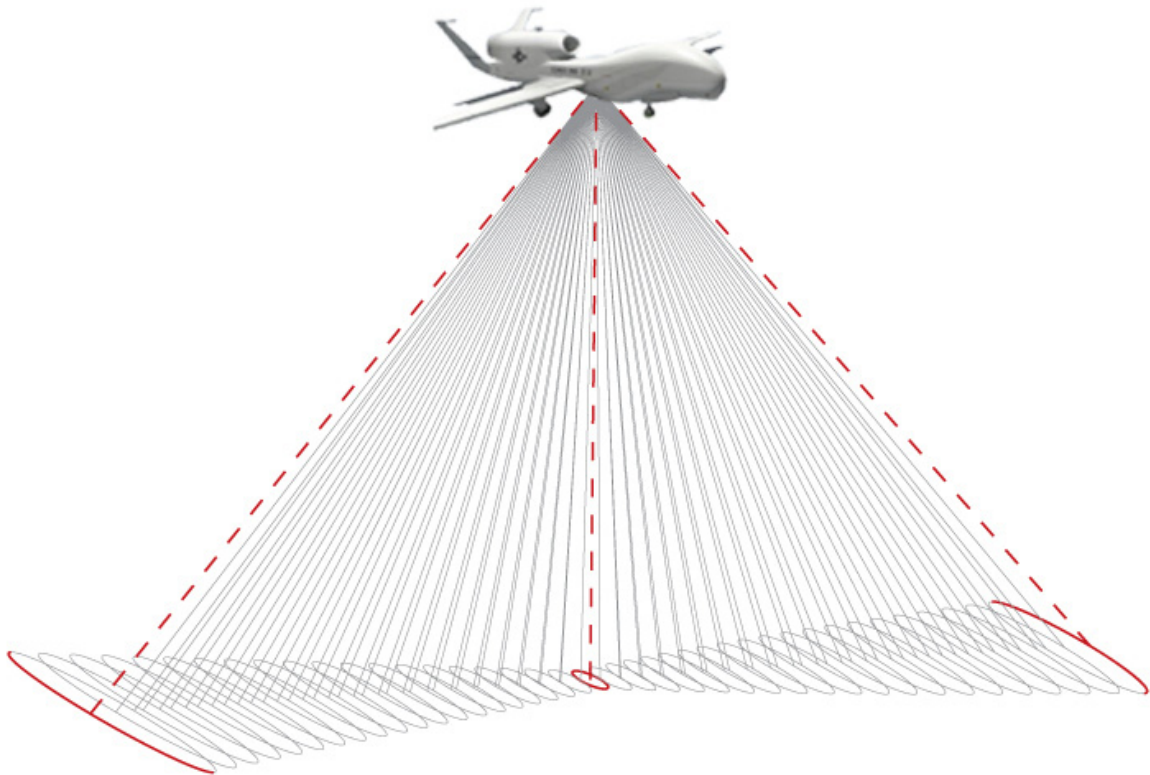


**Figure 2.5 Equivalent real-aperture pushbroom radiometer system with 41 beams cross-track.**

At each frequency, the pushbroom antenna beams are implemented in separate phased array designs that produce beam patterns that are similar to the synthesized beams for HIRAD.

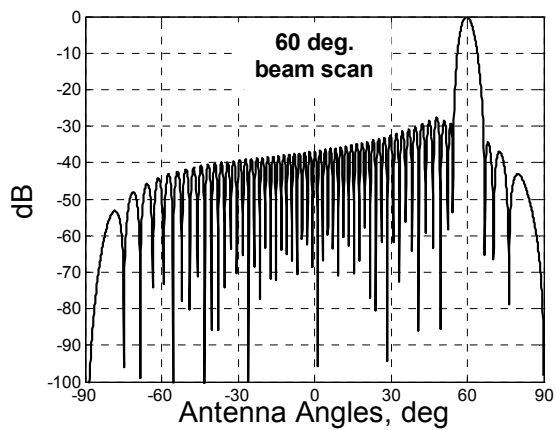
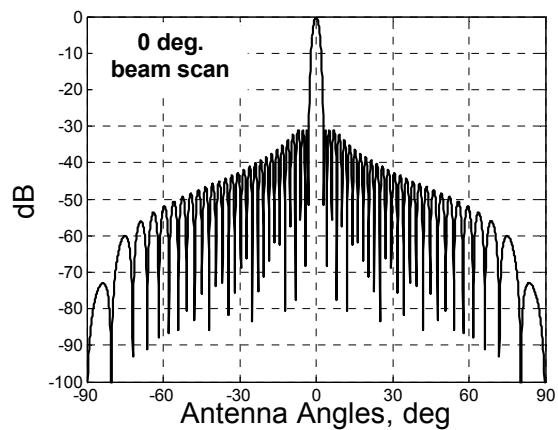
Specifically, there are 4 different antenna designs (one per frequency) and each antenna is a scanning phased array. Thus, the pushbroom patterns are equivalent in terms of the C-band operating frequencies, approximate antenna pattern spatial resolutions, cross-track boresight pointing angles (every 3 deg) and polarization properties.

The HIRAD antenna is designed to measure the horizontally polarized brightness temperature emission from the surface over  $\pm 60$  deg in the cross-track direction. Unfortunately, the sensitivity to unwanted cross-polarized (X-Pol) vertically polarized radiation is not negligible over the full swath and must be considered, especially at the edges of swath. The Co-Pol pattern of the HIRAD linear array element is a symmetric radiation pattern, similar to a cosine ( $\theta$ ), with maximum radiation at  $\theta = 0$ , and the corresponding X-Pol element pattern has a shape similar to a sine ( $\theta$ ) with a null at  $\theta = 0$ . Therefore, at nadir, the X-Pol contribution in HIRAD is minimal and increases with increasing off boresight angles. At 60 deg off boresight angle, the X-Pol level is approximately equal to the Co-Pol level (see Appendix B, Fig. B.2). The X-Pol performance of HIRAD was optimized during the design by controlling the shape of the patches shown in Fig. 2.2 (b), the location of the feed probe and introducing slots that were included in the bottom patches (4 and 5 GHz) to lower the X-Pol in the top two patches (6 and 6.6 GHz).

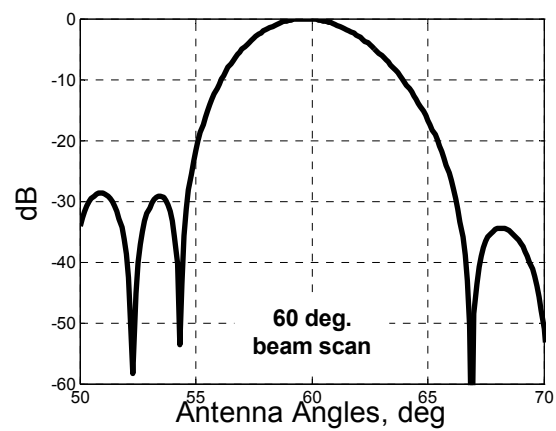
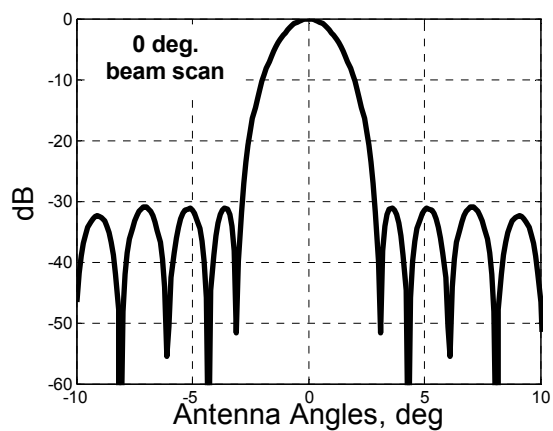
### 2.3 Equivalent Pushbroom Phased Array

When the HIRAD images the brightness temperature scene, we synthesize the equivalent pushbroom beam patterns (Co-Pol and X-Pol) for a real aperture antenna system. We choose to implement this real aperture antenna design as four scanning phased arrays (one for each frequency). Co-Pol and X-Pol patterns are computed at each frequency and for each of the 41 beam positions. These Co-Pol and X-Pol pushbroom patterns are used as part of the simulation forward model “antenna pattern convolution” process described in Chapter 3. Limited examples of the antenna patterns are presented in this section and more details of the antenna design are presented in Appendix B.

Figure 2.6 (a) shows the equivalent pushbroom Co-Pol antenna patterns for 6.6 GHz for the 0 deg (nadir) and 60 deg beam positions. Also shown in panel (b) are the expanded main beam antenna patterns, which illustrates the beam broadening as the antenna scans off the nadir direction. Further the corresponding equivalent pushbroom X-Pol patterns are shown in Fig. 2.7. In the simulation, the ratio of the X-Pol brightness temperature to the total antenna temperature is referred to as  $\gamma$  and is defined in Chapter 3.



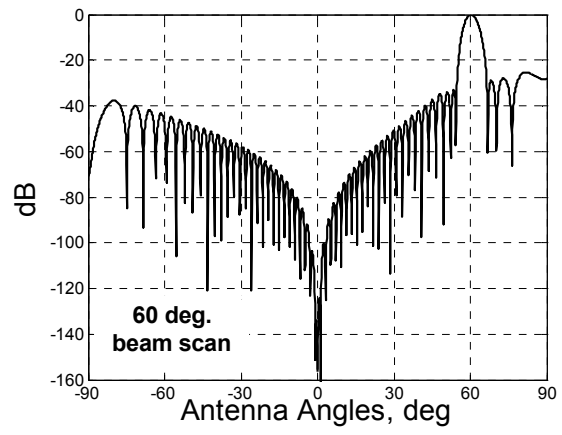
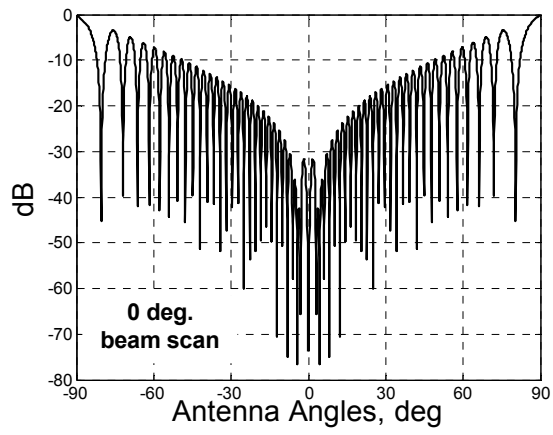
(a)



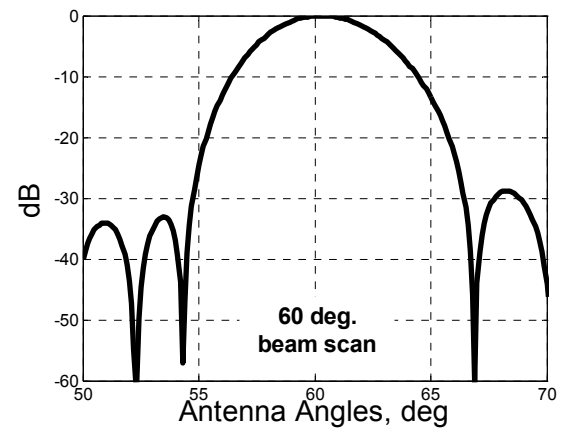
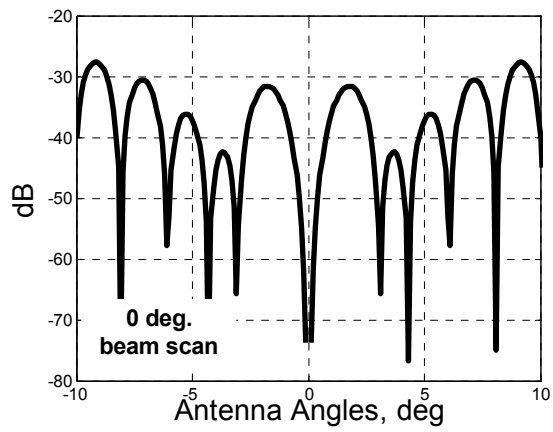
(b)

Figure 2.6 Co-Pol patterns at 6.6 GHz frequency for 0 deg and 60 deg scan beams. Panel - a shows wide-angle patterns and panel -b shows expanded main beam patterns.





(a)



(b)

**Figure 2.7 X-Pol patterns at 6.6 GHz frequency for 0 deg and 60 deg scan beams. Panel - a shows wide-angle patterns and panel -b shows expanded main beam patterns.**

The equivalent pushbroom phased array antenna was designed with main beam patterns that are approximately equal ( $< \times 2$  difference) compared to the synthesized HIRAD half power beamwidth at all boresight angles for all the frequencies. Table 2.1 presents the phased array antenna -3dB and the first null beamwidths along with the beam efficiency values. Also for comparison purposes, it includes the HIRAD synthesized beams -3dB and first null beamwidths. This degree of spatial matching is sufficient to preserve the spatial resolution of wind and rain measurements in this hurricane simulation. Furthermore, exactly matching of the half power beamwidth ratios is unimportant because it does not significantly contribute to measurement errors.

**Table 2.1 Comparison of phased array and HIRAD synthesized beams**

	Frequency, GHz	3dB BW, deg			Null BW, deg		Beam Efficiency, % Phased Array
		Phased Array	Ratio	HIRAD	Phased Array	HIRAD	
0 deg	4	2.6	1.24	2.1	7.2	4.6	93.1
	5	2.2	1.29	1.7	6.0	3.8	93.5
	6	2.2	1.47	1.5	6.0	3.4	93.8
	6.6	2.3	1.64	1.4	6.2	3.0	93.7
60 deg	4	5.2	1.58	3.3	14.7	7.4	95.2
	5	4.5	1.61	2.8	12.4	6.4	92.37
	6	4.4	1.69	2.6	12.2	6	90.57
	6.6	4.5	1.61	2.8	12.6	6.3	91.7

Figure 2.8 shows a comparison between the HIRAD synthesized beam pattern and the corresponding phased array beam at 0 and 60 deg for 6.6 GHz.

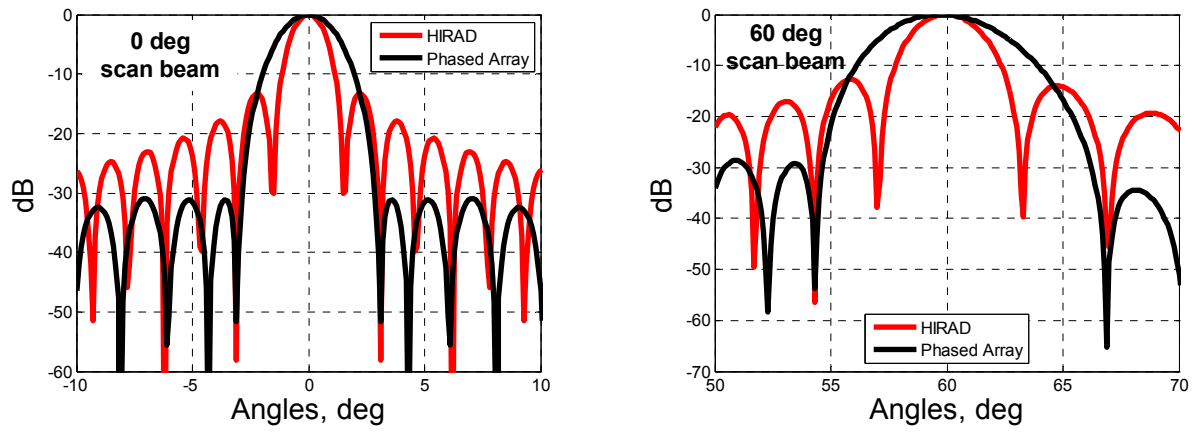


Figure 2.8 HIRAD squared beam pattern and phased array tapered beam patterns at 0 and 60 deg for 6.6 GHz.

## CHAPTER 3 : FORWARD MODEL SIMULATION

This chapter will discuss the forward radiative transfer model that is used to calculate brightness temperature emissions from both the sea surface and the atmosphere. The atmospheric model for hurricanes will be described; and this will be followed by a discussion of the simulation geometry and the antenna brightness temperature. Finally, simulated brightness temperatures will be shown for three typical aircraft passes through hurricane Frances.

### 3.1 Oceanic Remote Sensing

The calculation of blackbody microwave emissions from the earth and atmosphere is described by radiation transfer theory, which is illustrated in Fig. 3.1. The apparent brightness temperature ( $T_{app}$ ) seen by a microwave radiometer viewing the ocean surface through a slightly absorbing atmosphere is composed of three contributions, namely:

1.  $T_{UP}$ , the upwelling atmospheric brightness temperature emitted along the antenna line of sight,
2.  $T_{refl}$ , the sum of the downwelling brightness temperature ( $T_{DOWN}$ ) and the cosmic background ( $T_{cos}$ ) contribution that is specularly reflected from the sea surface, and
3.  $T_{sur}$ , the sea surface brightness temperature.

At the radiometer antenna, these  $T_b$  components combine non-coherently (powers add) as given in (3.1).

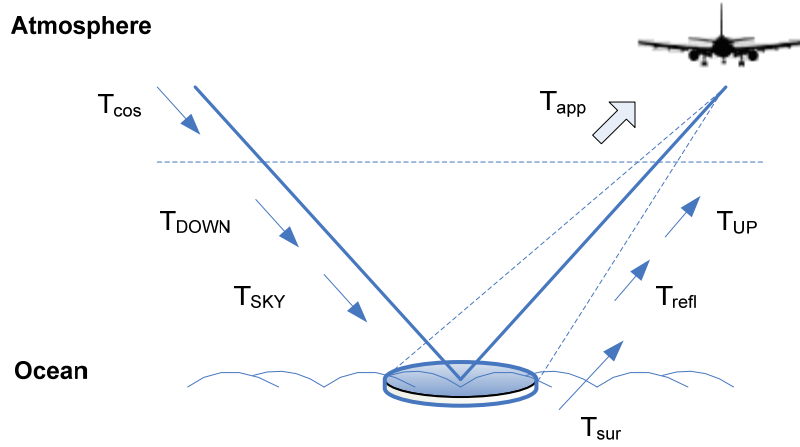


Figure 3.1 Brightness temperature signal as seen by an airborne radiometer.

$$T_{app} = T_{UP} + e^{-\tau} (T_{sur} + T_{refl}), \text{ Kelvin} \quad (3.1)$$

where  $e^{-\tau}$  is the total one-way atmospheric transmissivity. The ability of a microwave radiometer to make observations of surface characteristics, looking through the atmosphere, depends on atmospheric absorption, which is due to oxygen, water vapor, cloud liquid water and rain in the atmospheric column along the line-of-sight.

The three components of brightness temperatures shown in Fig. 3.1 are defined as follows:

$$T_{SKY} = e^{-\tau} * T_{cos} + T_{DOWN} \quad (3.2)$$

$$T_{refl} = (1 - \varepsilon) * T_{SKY} \quad (3.3)$$

$$T_{sur} = \varepsilon * SST \quad (3.4)$$

where  $\varepsilon$  is the sea surface emissivity, SST is the sea surface temperature in Kelvin and  $T_{\text{cos}} = 2.7$  Kelvin is the cosmic microwave background.

### 3.2 Sea Surface Emissivity Model

An improved microwave radiometric ocean surface emissivity model has been developed to support forward radiative transfer modeling of brightness temperature and geophysical retrieval algorithms for HIRAD. This physically based C-band emissivity model [10] extends current model capabilities to hurricane force wind speeds over a wide range of incidence angles. It was primarily developed using brightness temperature observations during hurricanes, which were obtained using the airborne Stepped Frequency Microwave Radiometer.

The ocean surface brightness is usually described by two orthogonal components of the brightness temperature (vertical and horizontal) collected by the radiometer antenna. The CFRSL ocean surface emissivity model adapted a physical based model formation with empirical coefficients, where it divided the total emissivity into two parts, foam part, and foam free part, as shown in (3.5).

$$\varepsilon_{\text{ocean}} = FF\varepsilon_{\text{foam}} + (1 - FF)\varepsilon_{\text{rough}} \quad (3.5)$$

where  $\epsilon_{\text{ocean}}$  represents the total ocean emissivity,  $\epsilon_{\text{foam}}$  is the foam emissivity (depends on wind speed, EIA, and frequency), FF is the foam fraction (% area covered by foam - depends on wind speed only), and  $\epsilon_{\text{rough}}$  is the rough emissivity which is given by (3.6)

$$\epsilon_{\text{rough}} = \epsilon_{\text{smooth}} + \Delta\epsilon_{\text{excess}} \quad (3.6)$$

where  $\epsilon_{\text{smooth}}$  is the smooth emission given by (3.7) using the air-to-ocean Fresnel power reflection coefficient ( $\Gamma$ ), and  $\Delta\epsilon_{\text{excess}}$  is the excess emissivity which depends on the sea surface temperature, frequency, polarization, incidence angle and wind speed.

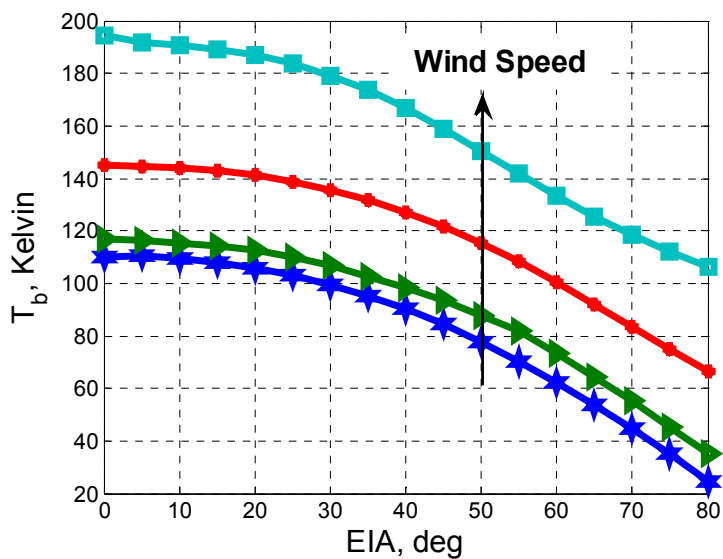
$$\epsilon = 1 - \Gamma \quad (3.7)$$

For wind-roughened ocean surfaces, the microwave emissions depend on both the polarized smooth surface Fresnel power reflection coefficients and the degree of surface roughness. Thus, the specular emissivity is modified by an additive emissivity term to account for roughness effects of ocean waves, which includes the effects of foam produced by the breaking ocean waves.

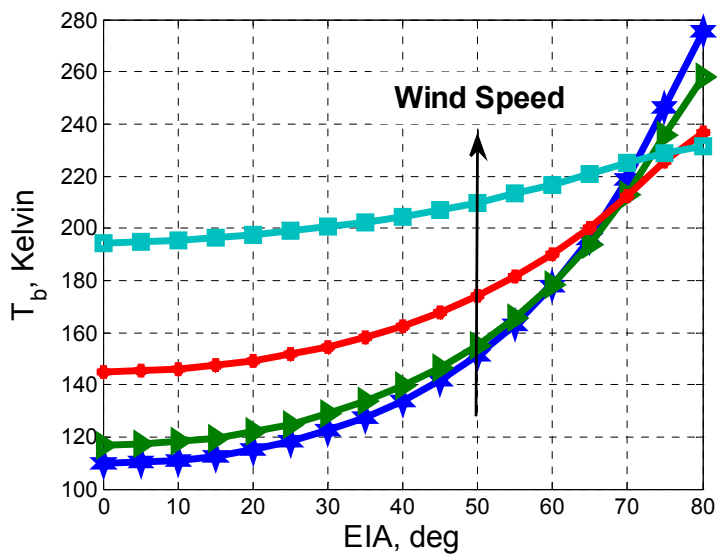
Figure 3.2 shows the CFRSL emissivity model with respect to incidence angle at 4 GHz scaled for a SST = 300 Kelvin for horizontal and vertical polarization and wind speeds of 6, 20, 40 and 70 m/s [10]. This model has been used in the forward and reverse RTM simulations to compute the ocean surface emission that affects two major components of the total brightness temperature ( $T_{\text{refl}}$ ,  $T_{\text{sur}}$ ). This model was developed to satisfy HIRAD geometry requirements for incidence

angles up to and beyond 60 deg and over the whole dynamic range of wind speeds from moderate to hurricane force winds (Cat. 5). The same plots for all HIRAD C-band frequencies are provided in Appendix C.





(a)



(b)

Figure 3.2 The CFRSL ocean surface emissivity model for SST = 300 Kelvin: (a) horizontal and (b) vertical polarization at 4 GHz and wind speeds of 6, 20, 40 and 70 m/s from El-Nimri et al., 2010 [10].

### 3.3 Rain Absorption Coefficient

Rain over the ocean increases the atmosphere absorption and thus “warms” the ocean brightness temperature i.e., surface contribution in (3.1) will be reduced (attenuated) while the atmospheric emission increases. For heavy rain, the atmosphere can be totally opaque, which masks the surface radiation. For this case, the atmospheric emissivity approaches unity and the brightness temperature saturates at the average rain physical temperature  $\sim 280$  Kelvin.

The rain model incorporated into the RTM is a statistical power law regression between absorption coefficient and rain rate in a form from the work of Jorgensen and Willis [13] and Olsen et al. [14] and is given by

$$k_R = aR^b \quad (3.8)$$

where  $k_R$  is the rain absorption coefficient in Np/km and exponent “b” is 0.69. The coefficient “a” is given by (3.9),

$$\begin{aligned} a &= gf^n \\ n &= 3.2 \end{aligned} \quad (3.9)$$

where the constant  $g = 9.4 \times 10^{-6}$ , Np/km.

These values are derived by Swift et al. [3] and are used by SFMR [1]. Since coefficient “a” is frequency dependent, the rain model is dispersive and this enables the multi-frequency retrieval of rain rate. Figure 3.3, is a plot of the rain rate absorption coefficient for the HIRAD frequencies according to (3.8).

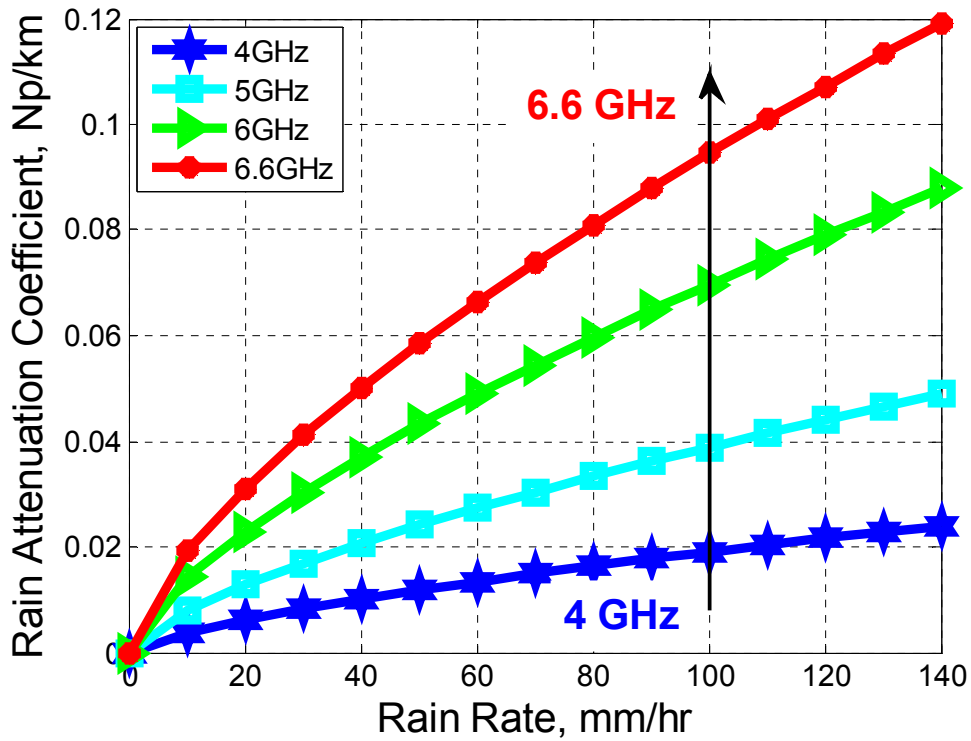


Figure 3.3 Rain absorption coefficients for HIRAD frequencies.

The relationship between transmissivity,  $\tau_r$ , and rain absorption coefficient,  $k_R$ , is,

$$\tau_r = \exp(-k_R h) * \sec(\theta) \quad (3.10)$$

where the product of the height of the rain column,  $h$ , (assumed to be the freezing level) times the secant of the incidence angle is the slant path through the rain along the line-of-sight.

Figure 3.4 (a) shows the Nadir-viewing rain transmissivity versus rain rate for a rain height of 5 km, which is a typical value over tropical oceans derived from the Tropical Rainfall Measuring Mission (TRMM) Microwave Imager (TMI) 3B11 monthly rain product. Even at C-band

frequencies, the decrease in transmissivity with rain rate is significant when looking through the entire rain column or at larger incidence angles that result in longer path lengths as illustrated by Fig. 3.4 (b). The transmissivity values shown are used in the forward and reverse atmospheric RTM to represent the attenuation in the brightness temperature ( $T_{\text{refl}}$ ,  $T_{\text{UP}}$ ,  $T_{\text{sur}}$ ) due to rain contamination, as it is noticed the higher the rain the more attenuation (less transmissivity) in the atmosphere.

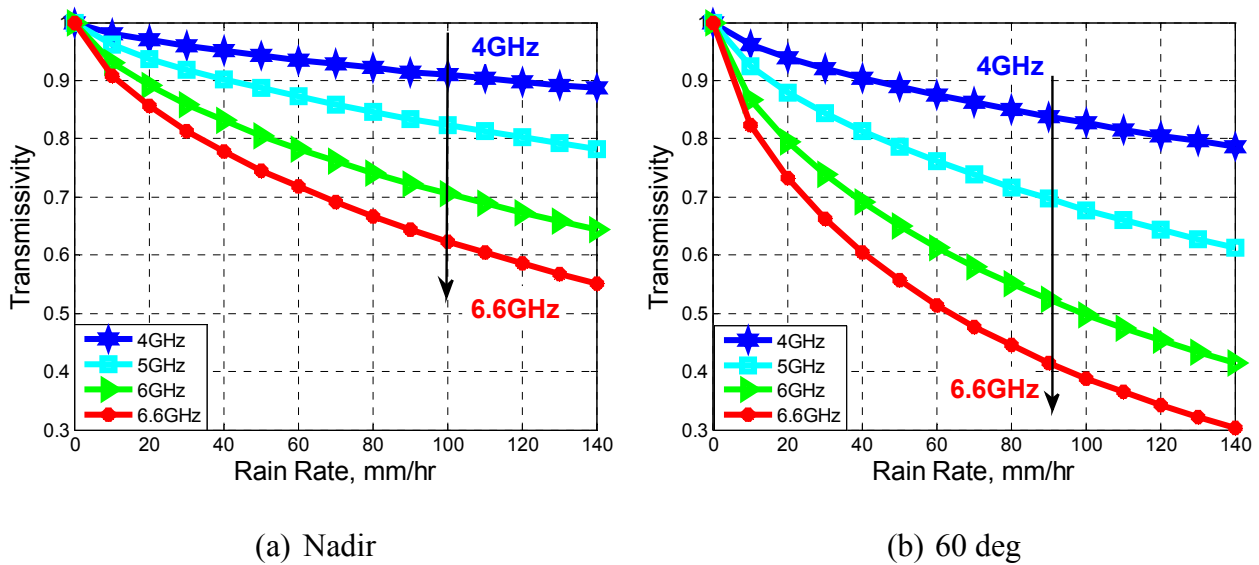


Figure 3.4 Rain transmissivity for a typical 5 km rain height for (a) Nadir-viewing, and (b) 60 deg-viewing.

### 3.4 Hurricane Radiative Transfer Model

Referring to Fig. 3.1, there are two atmospheric  $T_b$  components and the atmospheric transmissivity, which affect the radiative transfer model. Further, the upwelling and downwelling atmospheric  $T_b$ 's are the integral of emissions from each atmospheric layer along the propagation

path. The emissivity of each layer is determined by the sum of the four atmospheric absorption coefficients due to water vapor, molecular oxygen, cloud liquid water and rain.

The CFRSL radiative transfer model (known as RadTb [15]), has 39 atmospheric layers of 20 km total thickness, which are used to compute the water vapor, cloud liquid water and oxygen absorption coefficients. For the HIRAD frequencies, both the water vapor and cloud liquid absorption in hurricanes are significant, but oxygen is not. Further, rain is the dominant atmospheric absorber; and at high microwave frequencies, where the raindrop diameters become a significant fraction of a free-space wavelength, scattering may be significant. Fortunately at HIRAD frequencies scattering is not significant, even for high rain rates. Figure 3.5 shows the RadTb atmospheric model cartoon. As shown, the 39 layers have different thicknesses that are smaller near the surface and increase with altitude up to 20 km. This is due to the large condensation of gases near the surface which implies that more resolution (less thickness) is needed.

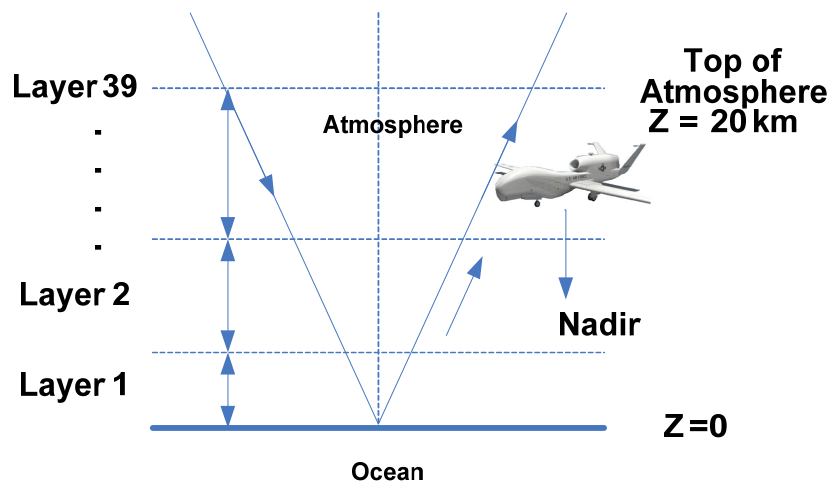


Figure 3.5 Forward (RadTb) atmospheric model.

### 3.4.1 MM5 Numerical Hurricane Model Data Description

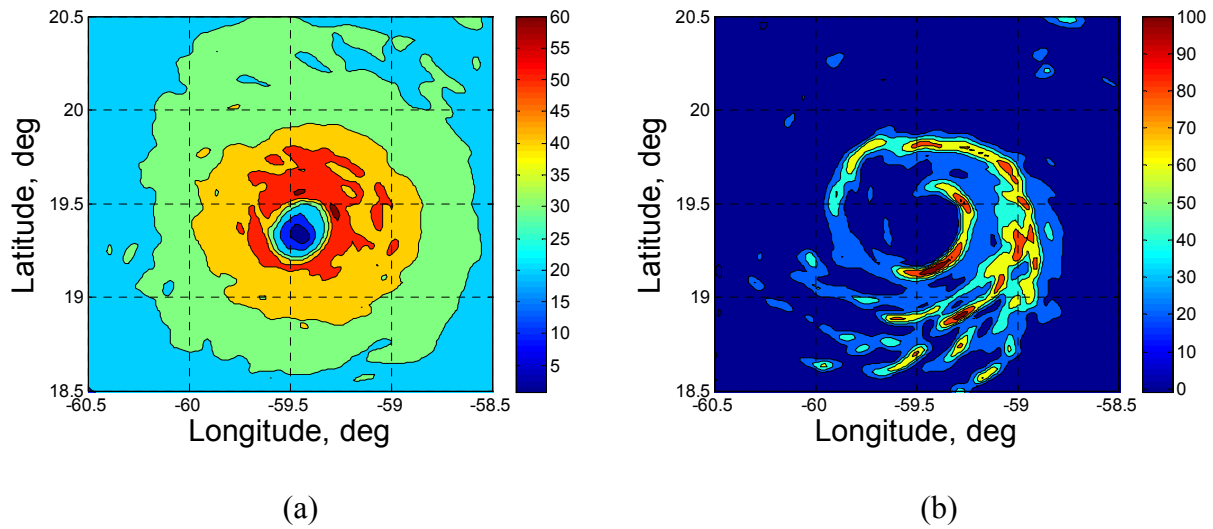
The MM5 hurricane “nature run” simulations were from a state-of-art numerical model described by Chen et al. (2007) [16]. A model run for Hurricane Frances (2004) provides realistic 3D environmental parameters (rain, water vapor, clouds, temperature and surface winds) from which simulated HIRAD  $T_b$ 's are derived for typical aircraft flight tracks. The MM5 model uses a system of nested grids with the innermost one having a horizontal grid spacing of 0.015 degrees ( $\sim 1.6$  km) in longitude and latitude. The model is non-hydrostatic in the atmosphere with detailed explicit microphysics and an interactive ocean wave model. The results include an eyewall, rainbands and other realistic convective and mesoscale structure.

Table 3.1 summarizes the atmospheric parameters that are considered in the HIRAD simulation. Parameters that are provided in 3D correspond to latitude, longitude and altitude.

**Table 3.1 Atmospheric parameters**

<b>Parameter</b>	<b>Included</b>	<b>Comment</b>
Rain Rate	3D	<ul style="list-style-type: none"> <li>• Most dominant factor in atmosphere</li> <li>• Data available in MM5</li> </ul>
Cloud Liquid Water	3D	<ul style="list-style-type: none"> <li>• <math>T_b</math> effects not very significant</li> <li>• Data available in MM5</li> </ul>
Super-cooled Water Water Vapor	3D 3D	<ul style="list-style-type: none"> <li>• Included in cloud liquid water</li> <li>• <math>T_b</math> effects are significant</li> <li>• Data available in MM5</li> </ul>
Oxygen	2D	<ul style="list-style-type: none"> <li>• <math>T_b</math> effects negligible</li> <li>• Surface pressure data available in MM5</li> </ul>
SST	2D	<ul style="list-style-type: none"> <li>• Data available from NSSTC</li> </ul>
Nitrogen	×	<ul style="list-style-type: none"> <li>• <math>T_b</math> effect negligible</li> <li>• Data not available in MM5</li> </ul>
Graupel	×	<ul style="list-style-type: none"> <li>• Ice is transparent at HIRAD frequencies</li> <li>• Data not available in MM5</li> </ul>

Figure 3.6 shows the surface wind (m/s) and rain (mm/hr) fields from the Hurricane Frances modeled data.



**Figure 3.6 Hurricane Frances surface fields at hour 20 on 31 August, 2004 for: (a) wind field (m/s) and (b) rain rate field (mm/hr).**

The MM5 numerical model output is provided in vertical layers from the surface to 20 km. Rain, cloud liquid and water vapor data are provided as mass mixing ratios of units kg/kg. The rain water mass function ( $\omega$ ) was converted to mm/hr using the air density profile according to Willis [17],

$$RR = \left( \frac{\omega \times \rho}{6.2 \times 10^{-5}} \right)^{1/0.913} \quad (3.11)$$

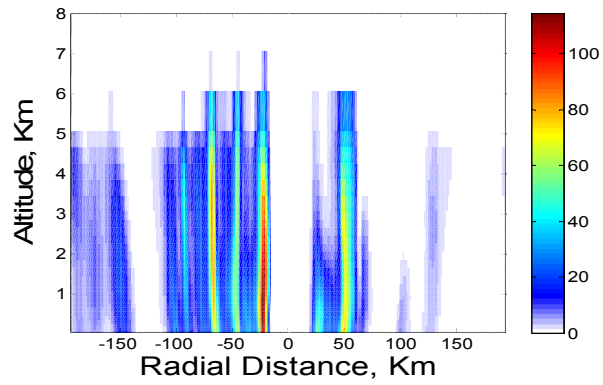
where  $\rho$  is the air density profile ( $\text{kg/m}^3$ ) that varies with altitude.

Analyses have been conducted to determine the importance of including the water vapor and cloud liquid water in the forward model and the retrieval RTM simulations. Error-free wind

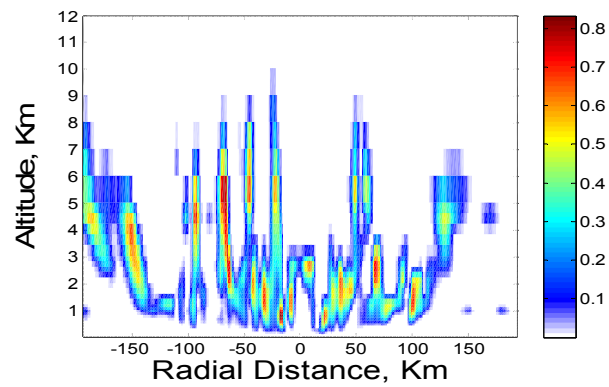


speed and rain rate retrieval simulations with and without the hurricane 3D water vapor and cloud liquid water fields were performed for homogeneous surface wind speed and rain rate values. Through these numerical experiments, it was determined that water vapor and cloud liquid water introduce small wind speed and rain rate retrieval errors and as such must be included in the simulation. Therefore, the water vapor and clouds mixing ratios were also converted from mass ratios (kg/kg) to  $\text{gm/m}^3$  by multiplying by the ambient air density at the given atmospheric layer. These quantities were then used to calculate the integrated water vapor and cloud liquid water densities per layer in  $\text{gm/cm}^2$  that were used as inputs to RadTb to compute the water vapor and cloud liquid water absorption coefficients.

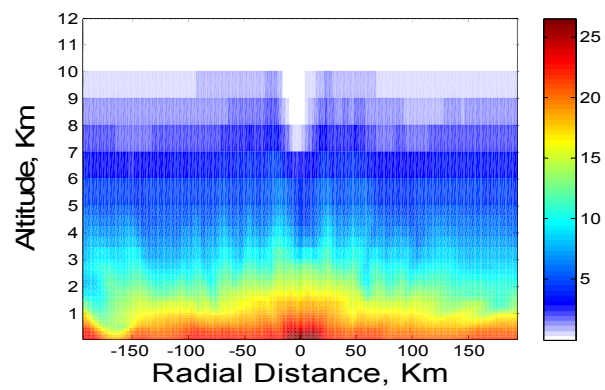
Figure 3.7 shows a 2D slice of the hurricane vertical profiles of: rain (panel-a), cloud liquid water (panel-b) and water vapor (panel-c) as a function of radial distance. As noted, these parameters are heterogeneous and thus are modeled in a 3D sense along the antenna line-of-sight. Because the rain does not extend beyond about 7 km altitude and both the clouds and the water vapor do not extend beyond 10 km, there is essentially no atmospheric effect above 10 km altitude.



(a)



(b)



(c)

Figure 3.7 Hurricane Frances 2D slices of: (a) rain in mm/hr, (b) cloud liquid water in gm/m<sup>3</sup> and (c) water vapor in gm/m<sup>3</sup>.

A realistic, high-resolution sea surface temperature field from the National Space Science and Technology Center (NSSTC) was used as the background SST in the forward radiative transfer model as shown in Fig. 3.8. As noted in the image, there is significant SST spatial variability that covers a dynamic range of approximately 2 Celsius.

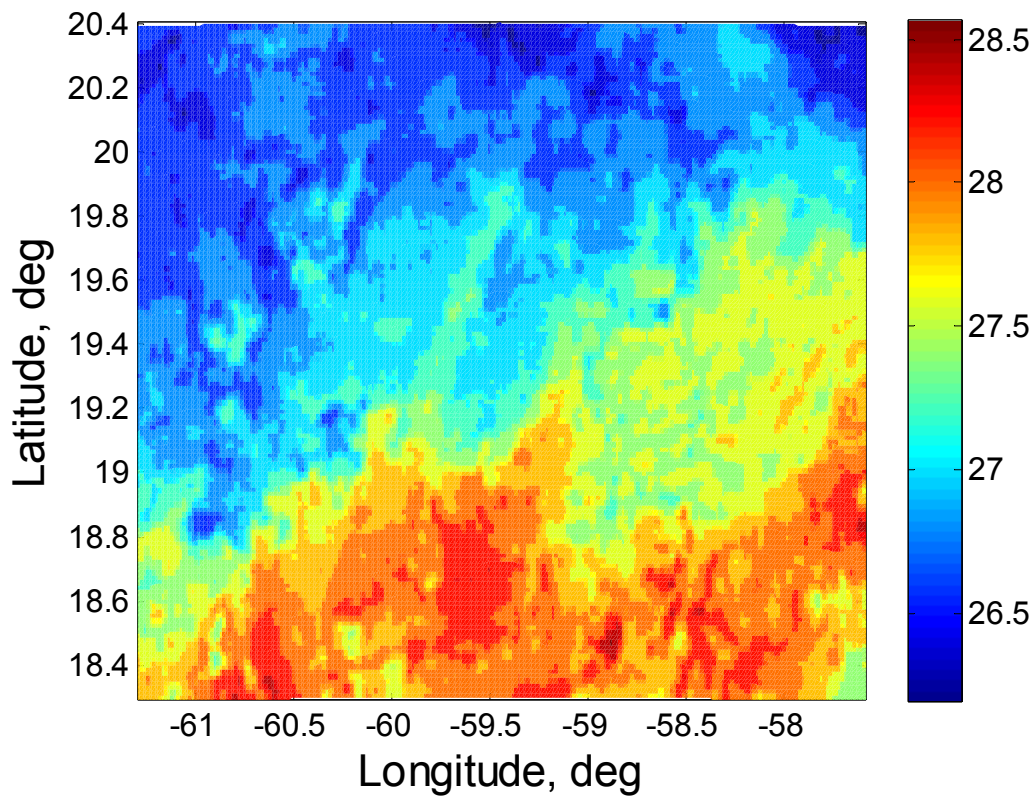


**Figure 3.8 Sea surface temperature field in Celsius.**

### 3.4.2 Simulation Geometry

The HIRAD antenna boresight geometry calculations are performed between  $\pm 60$  deg with beam positions located every 3 deg, which represent the HIRAD antenna sampling for the cross-track scans. To perform the geometry calculations, certain parameters are needed to simulate the aircraft ground track versus time and HIRAD pushbroom beams. The most significant parameters are: the aircraft heading at the flight track starting point (Initial Point, IP), altitude, ground speed and other antenna characteristics like beamwidths (to define the instantaneous field of view (IFOV) size).

Instantaneously HIRAD views the full swath at four frequencies and images the hurricane in cross-track scans, which translates to 1 MM5 pixel every 8 seconds from a 20 km altitude. Figure 3.9 shows the 3dB footprint (on the ocean surface) at 4 GHz for one HIRAD cross-track scan. A total of 41 beams on the ground correspond to the HIRAD swath of  $\pm 60$  deg. These beams are contiguous at nadir and they overlap at the edges of the swath.

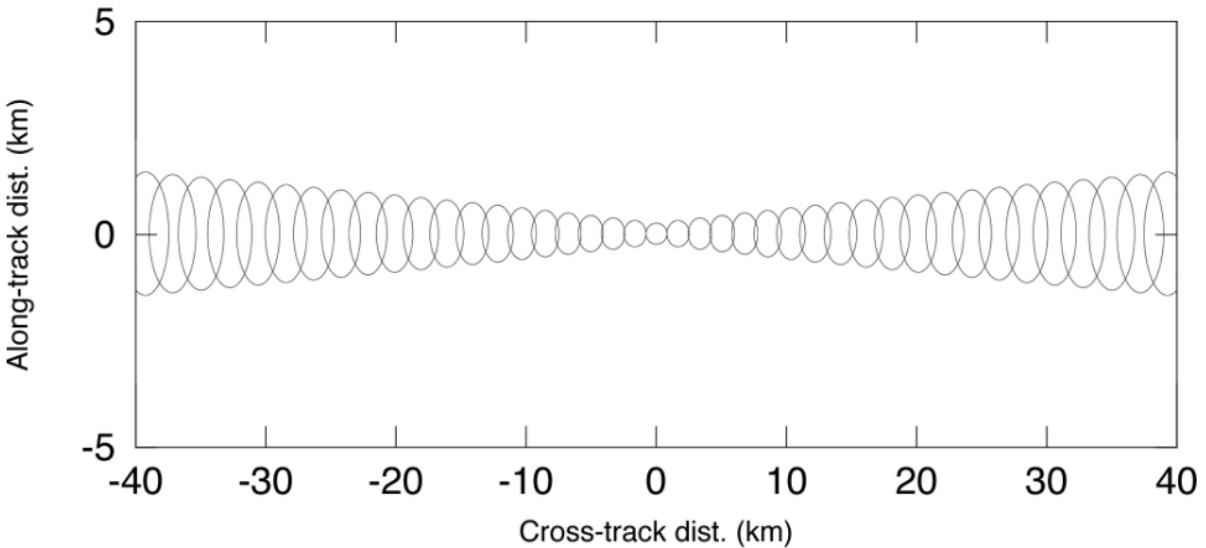


**Figure 3.9 HIRAD 3dB footprint on the ocean surface. Note that this figure distorts the slightly elliptical IFOV because of the different axis scales.**

### 3.4.3 Hurricane Atmospheric Model

The forward radiative transfer model simulation uses three-dimensional varying atmospheric parameters (rain, cloud liquid, water vapor, and temperature) along the antenna line-of-sight to the surface. Each of these components varies vertically with altitude and radially from the storm center, so each HIRAD measurement pixel will have an atmospheric profile different than the adjacent pixels. To implement this complexity, the forward radiative transfer model adopted a mesh grid criterion by dividing the atmosphere into 39 layers and the surface into 1.67 km pixels (corresponding to the MM5 resolution) as shown in Fig. 3.10. This approach approximates the actual HIRAD  $T_b$  measurement and causes the upwelling and downwelling brightness temperature components to be calculated along a different slant path.



**Figure 3.10 Example: forward radiative transfer model simulation for rain rate.**

Next, three typical scans simulated for a Global Hawk aircraft track at 20 km altitude are presented in Fig. 3.11. The first scan is in the eyewall region (right) where the highest winds occur, the second scan (middle) is through the center of the eye and the last scan is taken in the outer edge of the eyewall region (left) where the brightness temperature across the swath is uniform. The three scans are referred to as scan 1, 2, and 3, respectively, and the star symbol represents the scan nadir point. The swath width is approximately 70 km at the 20 km altitude. These three scans are used continuously in this dissertation as an example.

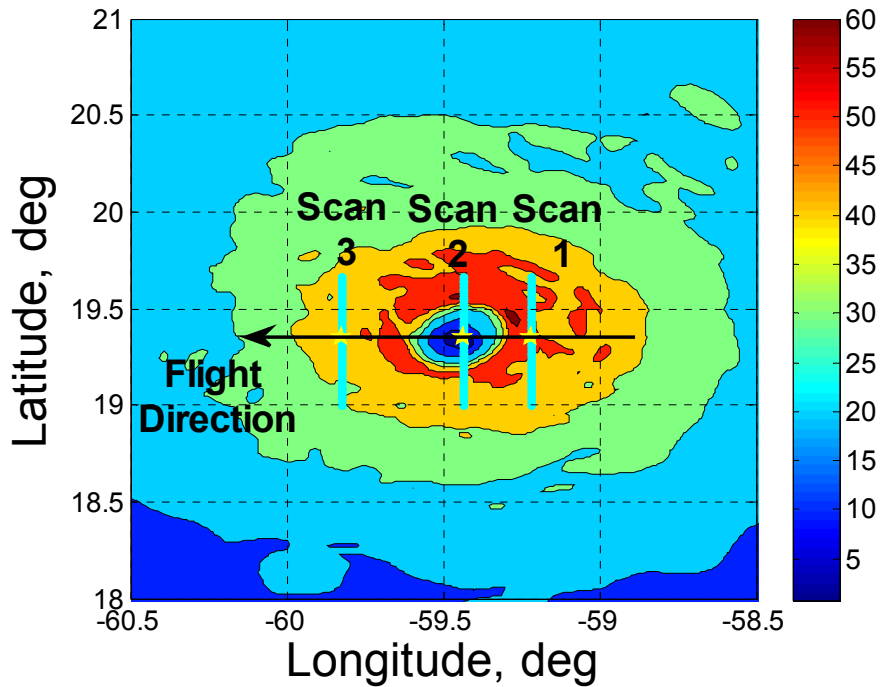
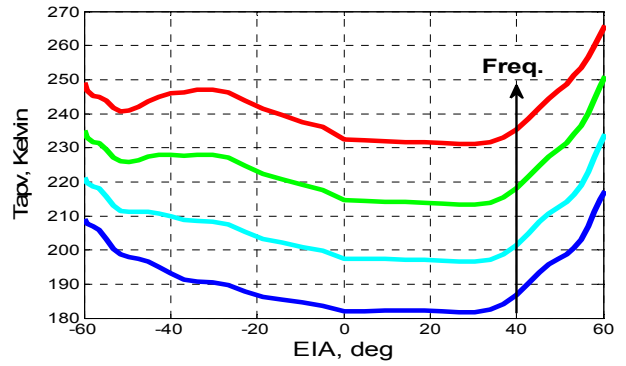
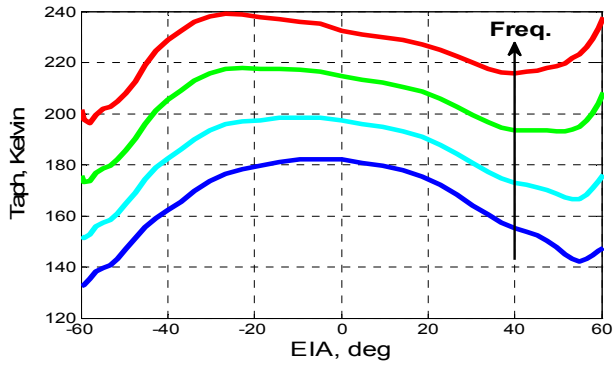
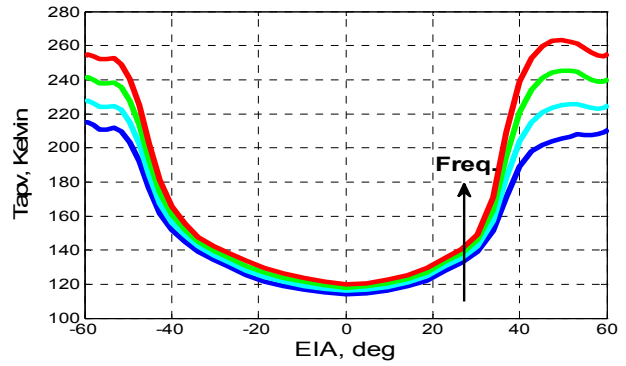
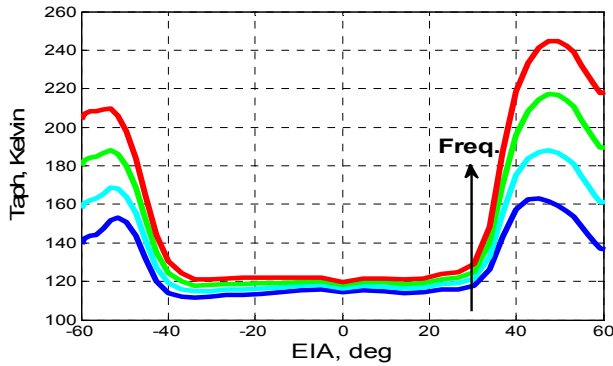


Figure 3.11 Frances wind field (m/s) with three HIRAD cross-track scans 1, 2 and 3 indicated.

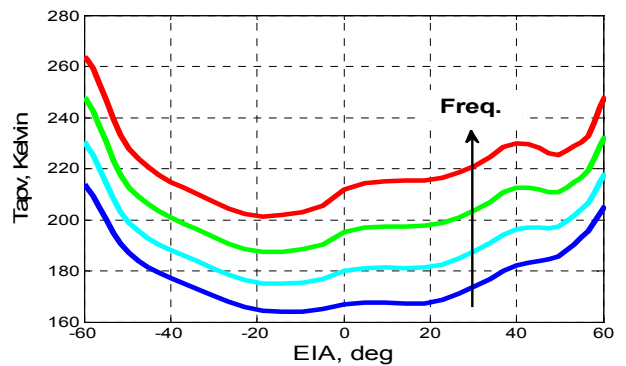
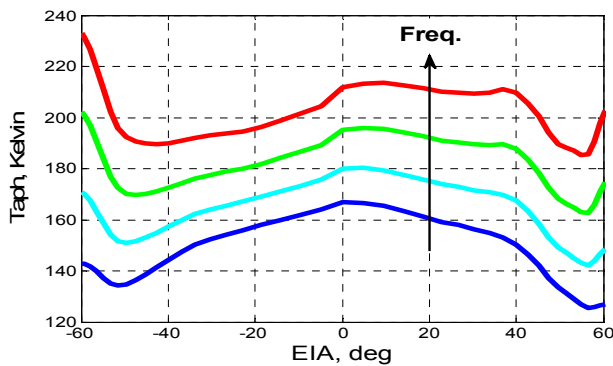
The cross-track  $T_b$  profiles for the three different scans are shown in Fig. 3.12 for all the frequencies. The H-Pol and V-Pol  $T_b$ 's are presented in the left and right panels respectively. From the three different scans, the variability in the temperature profiles is clearly shown. For example, scan 1 shows a high divergence in the  $T_b$  curves due to the intense rain bands in the eyewall region. Scan 2 on the other hand, passes through the eye of the hurricane (EIA's between  $\pm 30$  deg); and in this region of low wind speed and no rain, the curves are nearly the same. Also notice that the scan pattern  $T_b$ 's do not exhibit perfect symmetry, which is due to differences of the hurricane wind and rain fields in the northern and southern eyewalls. Finally, scan 3 shows more uniformity of the  $T_b$  scenes since the scan was taken towards the outer edge of the eyewall region.



(a) scan-1



(b) scan-2



(c) scan-3

**Figure 3.12 Simulated cross-track brightness temperature scenes for (a) scan 1 in the eyewall region, (b) scan2 is through the center of the eye and (c) scan 3 is taken at the outer edge of the eyewall region. Left-hand panels are H-Pol and right-hand are V-Pol.**



### 3.5 Antenna Brightness Temperature

The HIRAD image reconstruction algorithm is under development at the University of Michigan and is not available for use in this dissertation; therefore, we elected to use the traditional radiometer approach [9] to simulate the hurricane brightness temperature measurement. We use a real aperture phased array antenna to produce multiple antenna beams in a pushbroom configuration for the wide-swath surface sampling, which is approximately equivalent to the HIRAD brightness temperature image synthesis.

The brightness distribution is defined in terms of an apparent temperature  $T_{app}(\theta, \Phi)$  as shown in Fig. 3.13.

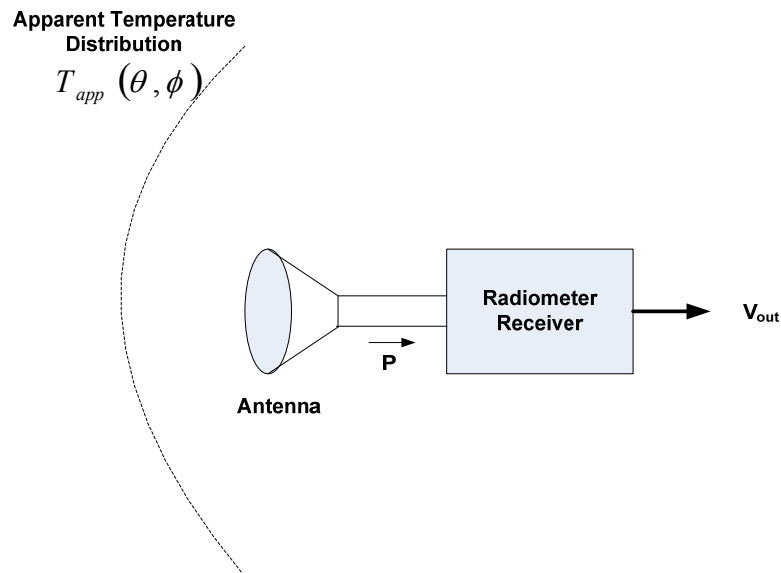


Figure 3.13 Apparent temperature distribution [9].

The antenna output brightness,  $T_A$ , is defined by Ulaby et al. as the convolution of the scene brightness temperature over a spherical surface surrounding the antenna with the antenna gain pattern [9], which is expressed as,

$$T_A = \frac{\iint_{4\pi} T_{app}(\theta, \Phi) \times F_n(\theta, \Phi) \times d\Omega}{\iint_{4\pi} F_n(\theta, \Phi) \times d\Omega} \quad (3.12)$$

where  $T_{app}(\theta, \Phi)$  is the scene apparent temperature distribution,  $F_n(\theta, \Phi)$  is the antenna power gain weighting function, and the solid angle,  $d\Omega$ , is given by,

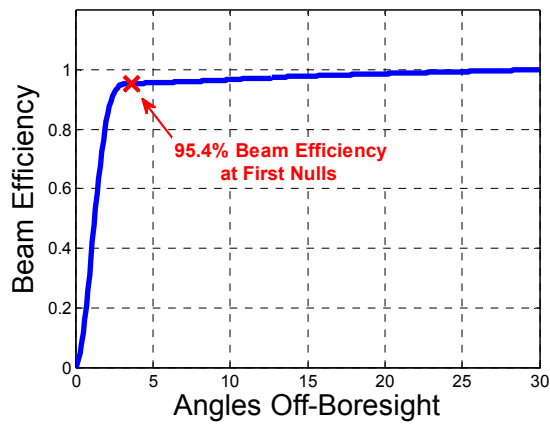
$$d\Omega = \sin\theta d\theta d\Phi \quad (3.13)$$

Both the H-Pol and V-Pol scene apparent brightness temperatures, which are computed from the forward model, are convolved with the co-polarized (Co-Pol) and the cross-polarized (X-Pol) antenna patterns respectively. The resulting convolved H-Pol and V-Pol temperatures are given by,

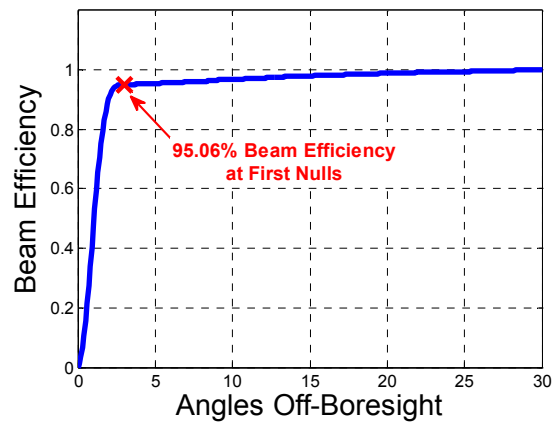
$$T_{bHconv} = \frac{\int_0^{2\pi} \int_{-\theta_1}^{\theta_1} T_{aph}(\theta, \Phi) \times F_{Co-Pol}(\theta, \Phi) \times \sin\theta d\theta d\Phi}{\int_0^{2\pi} \int_{-\theta_1}^{\theta_1} F_{Co-Pol}(\theta, \Phi) \times \sin\theta d\theta d\Phi} \quad (3.14)$$

$$T_{bVconv} = \frac{\int_0^{2\pi} \int_{-\theta}^{\theta} T_{apv}(\theta, \Phi) \times F_{X-Pol}(\theta, \Phi) \times \sin\theta d\theta d\Phi}{\int_0^{2\pi} \int_{-\theta}^{\theta} F_{X-Pol}(\theta, \Phi) \times \sin\theta d\theta d\Phi} \quad (3.15)$$

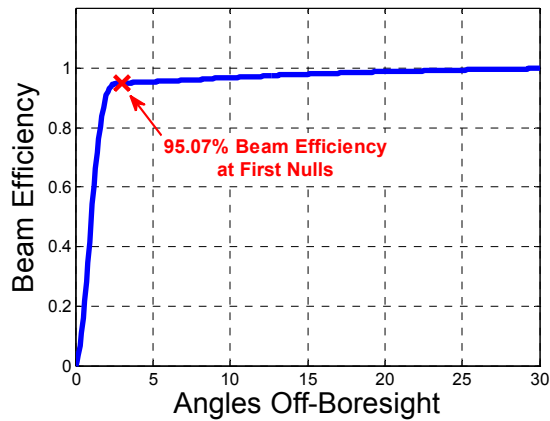
In (3.14), the horizontally convolved  $T_b$  is integrated over  $\pm \theta_1 = \pm 30$  deg that results in  $\sim 100\%$  beam efficiency for the Co-Pol antenna pattern, as shown in Fig 3.14, whereas in the vertically convolved  $T_b$  given by (3.15), the  $\theta$  limits change by beam position to insure  $> 90\%$  beam efficiency.



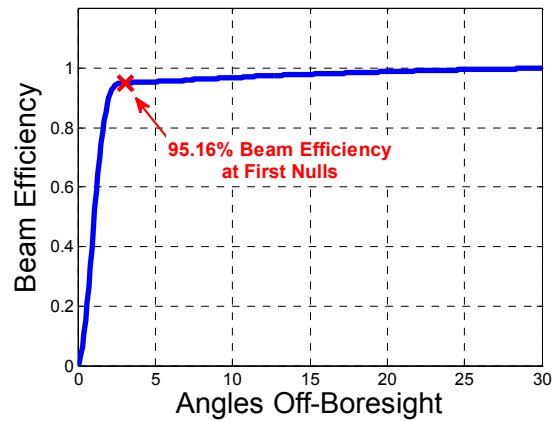
(a) 4 GHz



(b) 5 GHz



(c) 6 GHz



(d) 6.6 GHz

**Figure 3.14 Co-Pol zero boresight pattern beam efficiency for (a) 4 GHz (b) 5 GHz (c) 6 GHz and (d) 6.6 GHz with the red cross identifying the first null beam efficiency.**

The total convolved antenna brightness temperature,  $T_A$ , is a superposition of  $T_{bHconv}$  and  $T_{bVconv}$  according to,

$$T_A = (1 - \gamma)T_{bHconv} + \gamma T_{bVconv} \quad (3.16)$$

where  $\gamma$  is the ratio of the X-Pol brightness temperature to the total and is approximated by (3.17),

$$\gamma = \frac{\int_{FirstNulls} XPol}{\int_{FirstNulls} XPol + \int_{FirstNulls} CoPol} \quad (3.17)$$

$\gamma$  changes as a function of incidence angle (beam position) for each frequency as shown in Fig. 3.15. This is caused by changes in the Co-Pol and X-Pol patterns that are described in Chapter 2 and in Appendix B.

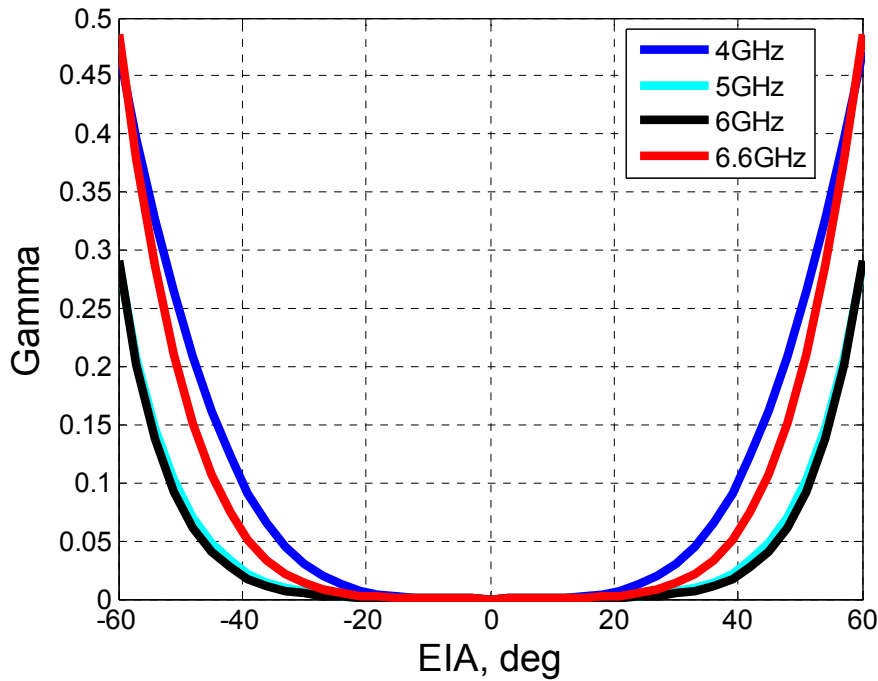
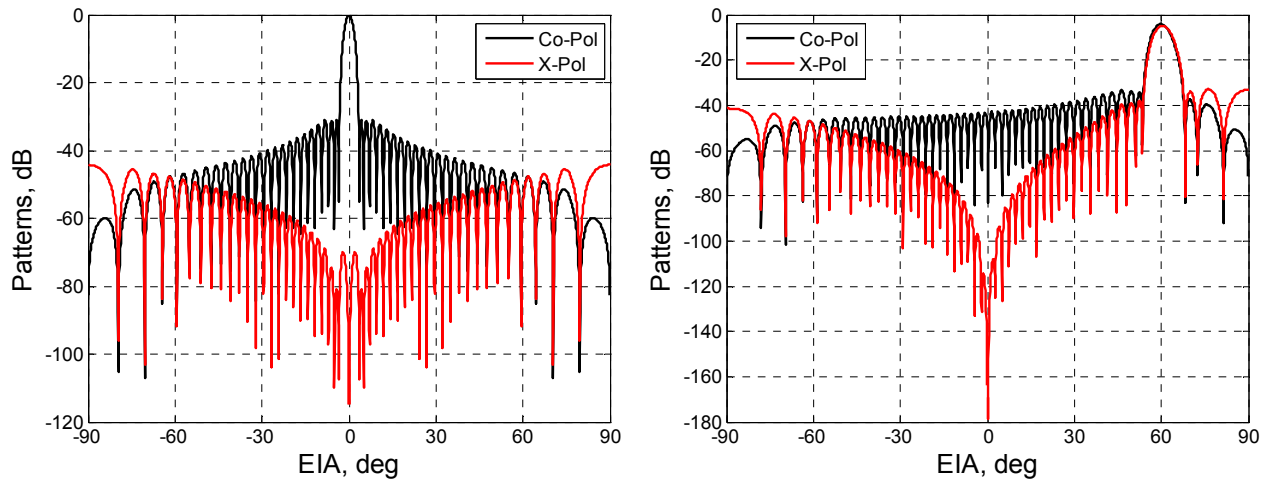
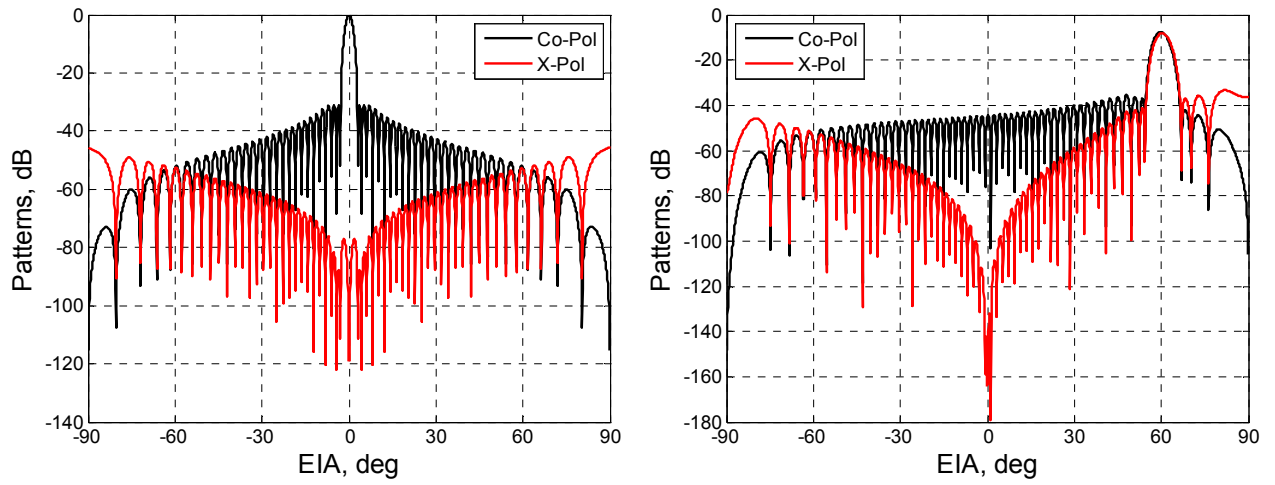


Figure 3.15 Integrated X-Pol brightness fraction ( $\gamma$ ).

The antenna patterns (X-Pol, Co-Pol) for both 4 and 6.6 GHz are shown in Fig. 3.16. For the nadir beam (left panel), nearly all the brightness is from Co-Pol making  $\gamma$  approximately equal to zero. The right panel of Fig. 3.16 shows the corresponding patterns for the beam position at 60 deg, where both patterns have the same power gain, which results in approximately half of the measured brightness coming from X-Pol and half from the Co-Pol, making  $\gamma \sim 0.5$ .



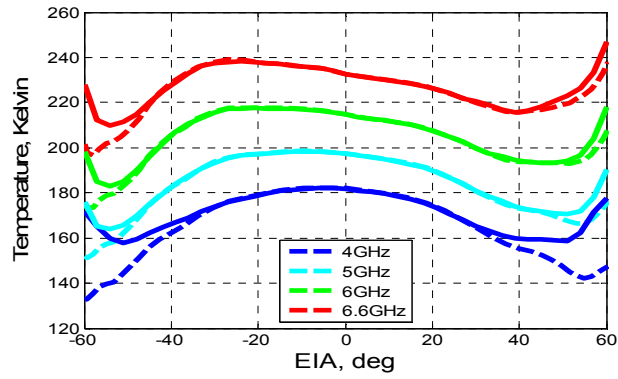
(a) 4 GHz



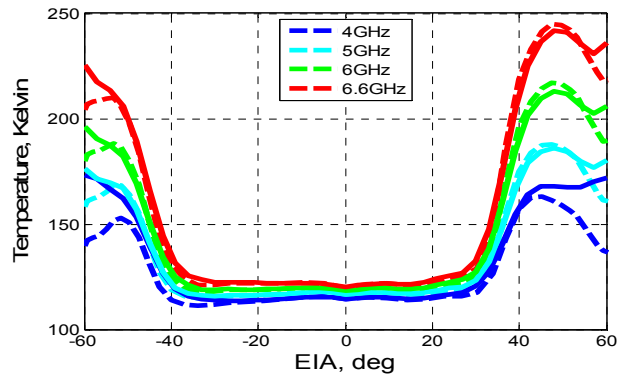
(b) 6.6 GHz

Figure 3.16 Co-Pol and X-Pol patterns at Nadir (left panel) and 60 deg (right panel) beam positions for (a) 4 GHz and (b) 6.6 GHz.

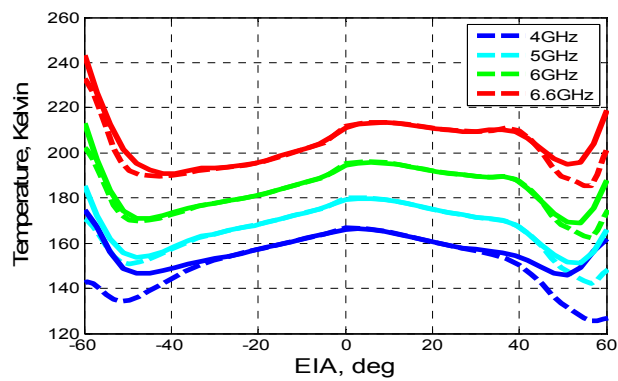
Next, the convolved  $T_A$ 's (solid lines), for the same three scans described earlier in this chapter are shown in Fig. 3.17 for all the frequencies. Also shown for comparison purposes is the true horizontal apparent brightness temperature,  $T_{\text{aph}}$ , (dashed lines) that is computed in the forward model. For angles  $> 40$  deg, there is a significant departure between the antenna temperature and the boresight brightness temperature, which is due to polarization mixing with the X-Pol. Thus, because of the equivalent high main beam efficiency of the HIRAD brightness image synthesis, there is a very minor effect of the pattern convolution except for X-Pol at wide scan angles. For example, at 60 deg, almost half of the antenna temperature comes from the X-Pol (V-Pol which is warmer).



(a)



(b)



(c)

Figure 3.17 Comparison between  $T_A$  (solid line) and  $T_{ap}$  (dashed line) at all frequencies for (a) scan 1, (b) scan 2 and (c) scan 3.



## CHAPTER 4 : GEOPHYSICAL RETRIEVAL ALGORITHM

In this dissertation, a hurricane retrieval algorithm was developed to infer wind speeds and rain rate in hurricanes. It comprises a least-squares inversion algorithm, which includes a radiative transfer model similar to the forward RTM described in Chapter 3. The retrieval algorithm block diagram is presented in Fig. 4.1, and the details will be discussed in this chapter.

The first step in the HIRAD retrieval algorithm is the antenna brightness temperature correction. This procedure is to estimate the true  $T_b$  at the antenna boresight, which involves subtracting the cross-polarized V-Pol brightness temperature and the collection of energy from outside of the antenna pattern main beam.

The next step is to calculate theoretical hurricane  $T_b$ 's for all possible combinations of surface wind speed and integrated rain rate. For this, an independent "retrieval RTM" is used with environmental parameters available from an *a priori* hurricane climatology and data bases parametrically to compute a theoretical modeled brightness temperature matrix over a wide range of possible wind speed, rain rate and incidence angles for the four HIRAD frequencies. Using these possible theoretical brightness temperatures ( $T_{\text{mod}}$ ), the retrieved ocean surface wind speed and rain rate are estimated using the statistical least-squares difference method according to,

$$\sum_{i=1}^4 \left[ (T_{\text{corr}} + \text{Noise})_i - \left( \hat{T}_{\text{model}} \right)_i \right]^2 \quad (4.1)$$

Realistic sources of random errors, which are expected in hurricane observations, are added to the simulated HIRAD measurements and the retrievals are performed using a Monte Carlo simulation. In this procedure, the wind speed and rain rate that minimize the difference between the simulated HIRAD  $T_b$  measurements and modeled apparent brightness temperatures across all HIRAD frequencies will infer the retrieved wind speed and rain rate values.

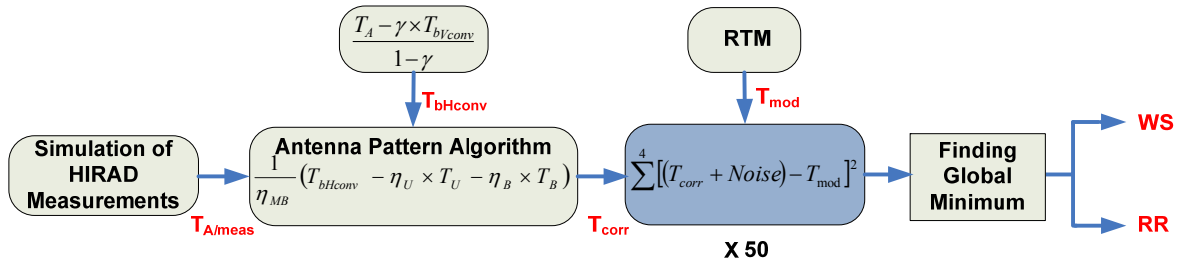


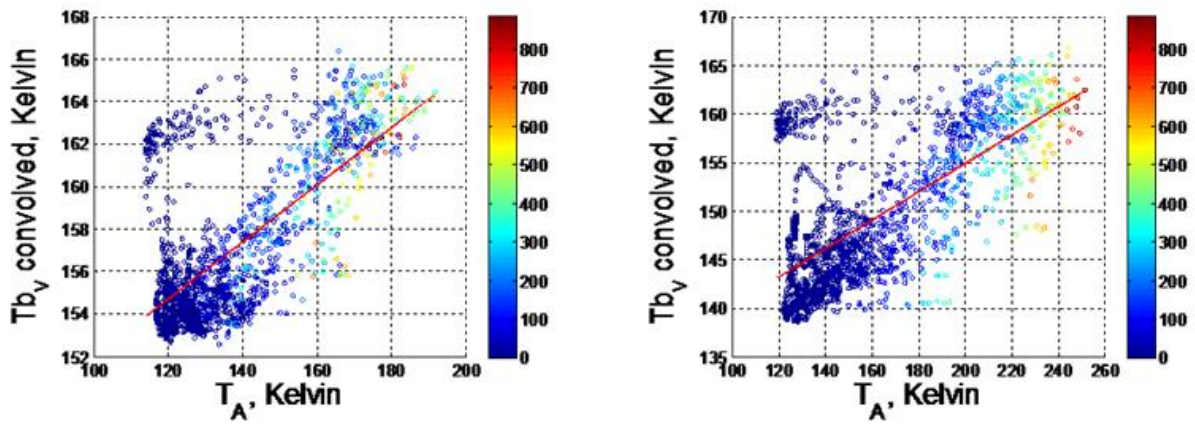
Figure 4.1 HIRAD retrieval algorithm block diagram.

#### 4.1 Antenna Pattern Correction

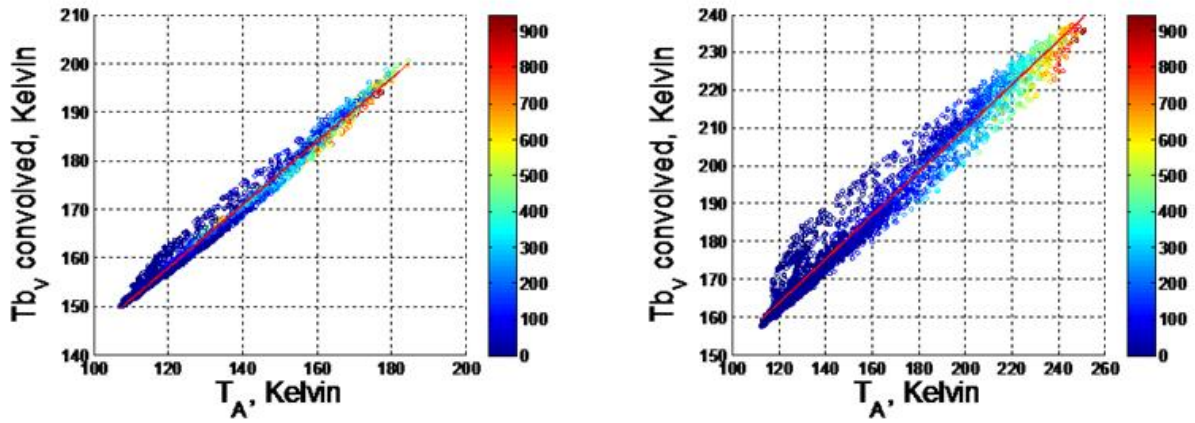
The purpose of the antenna pattern correction algorithm is to estimate the true horizontally polarized brightness temperature at the antenna boresight. This involves correcting for the effects of the antenna cross polarization coupling and the antenna pattern (sidelobes). The first step in this process was to remove the Cross-Pol component of the brightness temperature ( $T_{bVconv}$ ) from the total antenna brightness temperature ( $T_A$ ) according to,

$$T_{bHconv} = \frac{T_A - \gamma \times T_{bVconv}}{(1 - \gamma)} \quad (4.2)$$

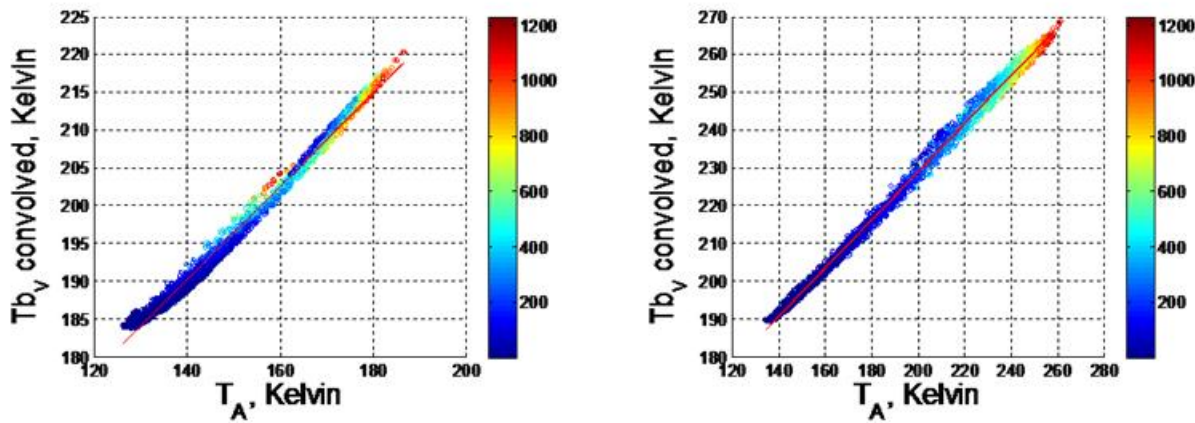
In an actual HIRAD measurement, the hurricane  $T_b$  scene will not be known; so we performed a simulation study to investigate the correlation between the measured antenna temperature and the corresponding convolved V-Pol brightness temperature. For three aircraft Fig-4 legs, the vertically polarized  $T_b$  were calculated and used to compute the convolved  $T_{bV}$ , which was then correlated with the corresponding antenna temperature. We used regression analysis to provide a statistical relationship, and results shown in Fig. 4.2 illustrate the linear curve fits (red lines) between  $T_A$  and  $T_{bVconv}$  at three different boresight angles; Nadir,  $\pm 30$  deg and  $\pm 60$  deg for 4 and 6.6 GHz frequencies. More scattering exists (weaker correlation) at near Nadir angles, but this will not significantly affect the  $T_b$  correction since the cross-polarized coupling  $\gamma$  is small ( $\sim$  zero) near these angles.



(a)



(b)



(c)

Figure 4.2 Correlation of  $T_A$  and  $T_{bVconv}$  brightness temperatures for 4 GHz (left panel) and 6.6 GHz (right panel) for (a) Nadir, (b)  $\pm 30$  deg and (c)  $\pm 60$  deg. The color-bar refers to the integrated RR values in km-mm/hr.

After solving for  $T_{bHconv}$ , the brightness temperature contributions from outside of the main beam are accounted for and the corrected brightness temperature ( $T_{corr}$ ) is,

$$T_{Corr} = \frac{1}{\eta_{ML}} [T_{bHconv} - \eta_U \times T_U - \eta_B \times T_B] \quad (4.3)$$

where  $\eta_{ML}$ ,  $\eta_U$ , and  $\eta_B$  are the beam efficiencies for the main lobe, above the boresight and below the boresight portions.  $T_U$  and  $T_B$  represent the collection of thermal emission through the remainder of the antenna pattern as illustrated in Fig. 4.3.

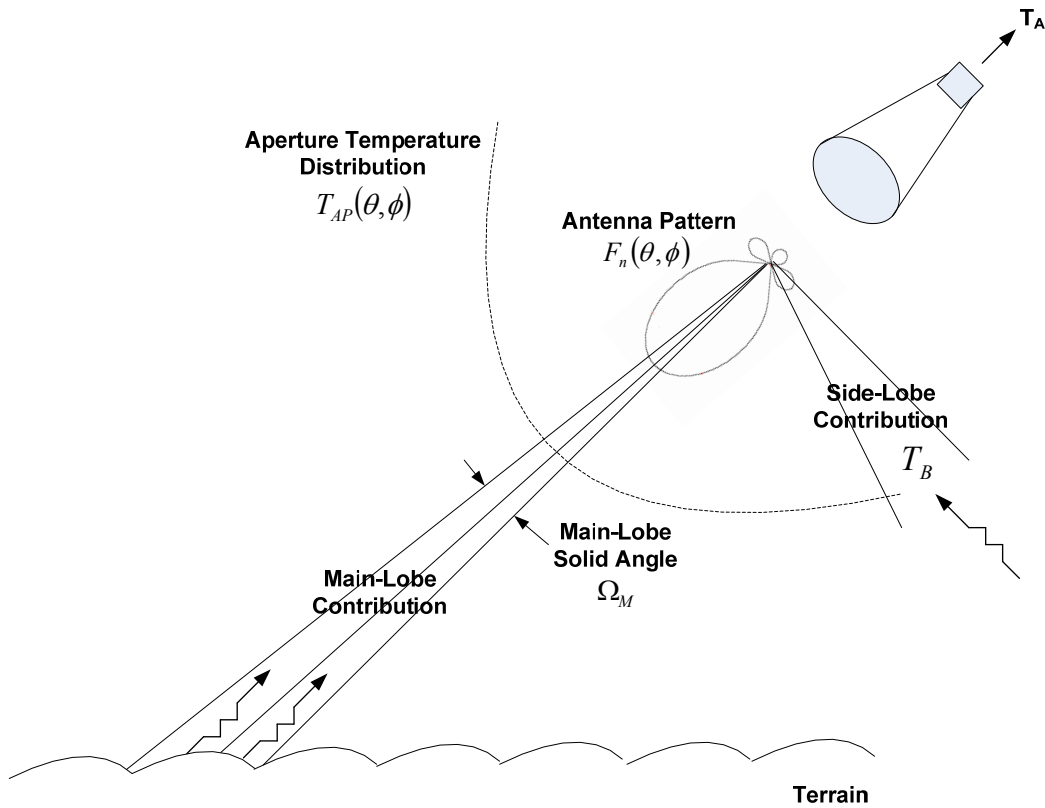
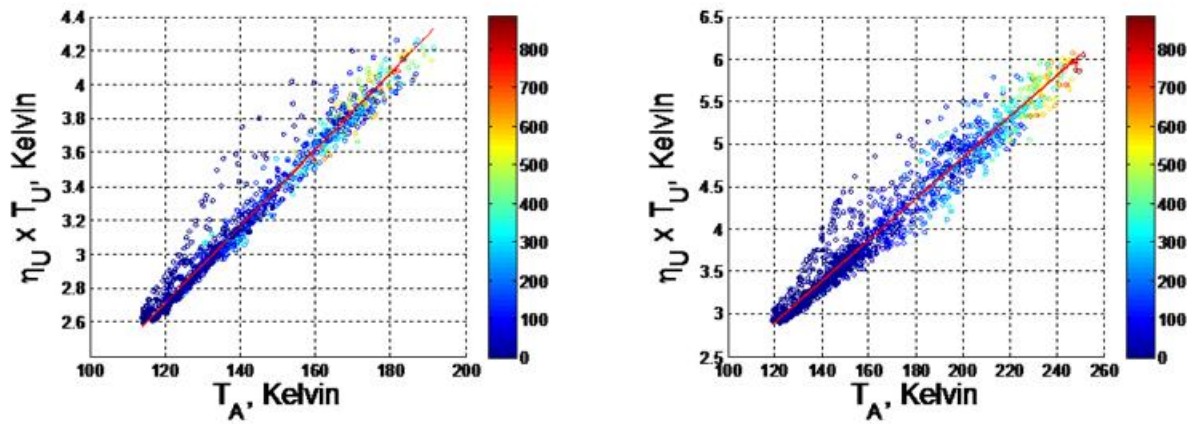
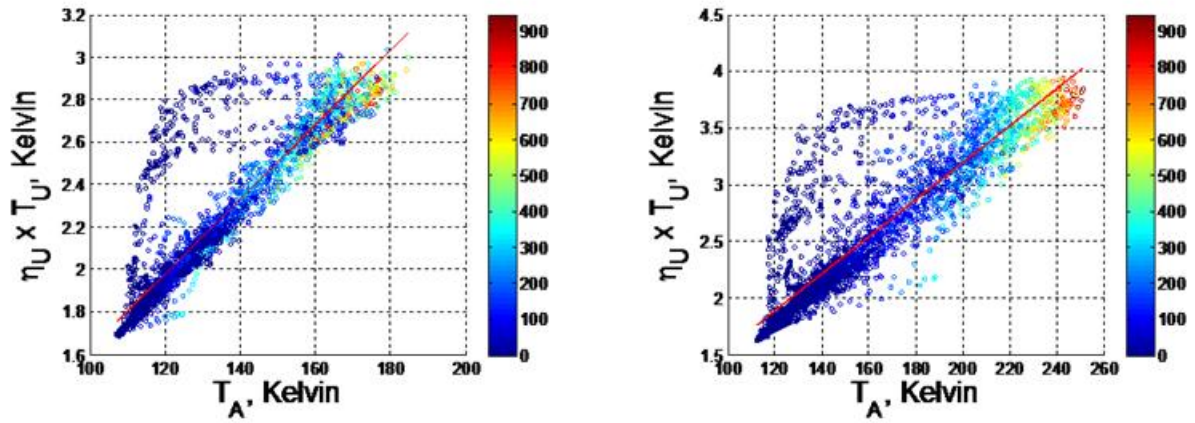


Figure 4.3 Main-lobe and side-lobe contributions to the antenna temperature  $T_A$  [9].

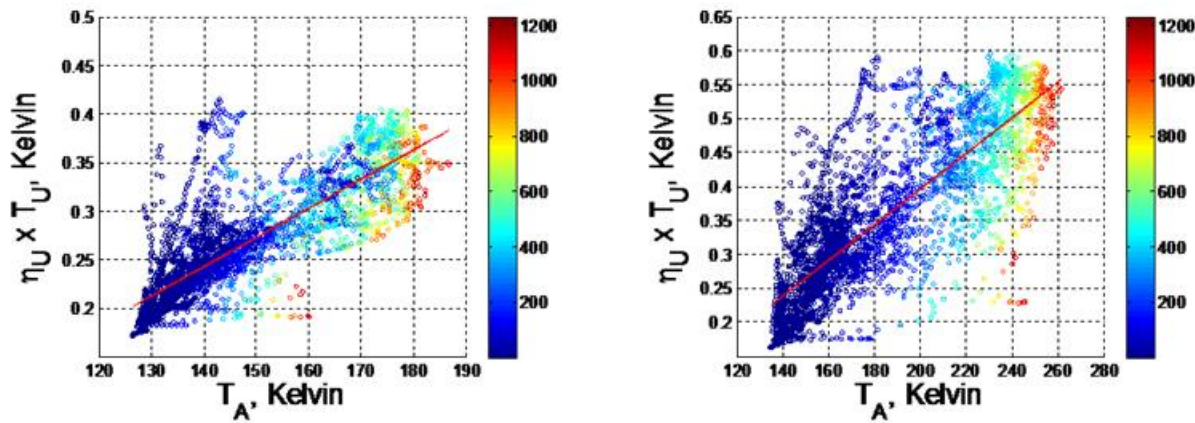
Again, in an actual HIRAD measurement, the terms  $\eta_U \times T_U$  and  $\eta_B \times T_B$  are unknown; but we used a similar procedure as described above to estimate them based on the statistical regression analysis with  $T_A$ . Results shown in Fig. 4.4 and Fig. 4.5 are the relationships are used in (4.2) to calculate the brightness temperature that goes into the retrieval algorithm.



(a)

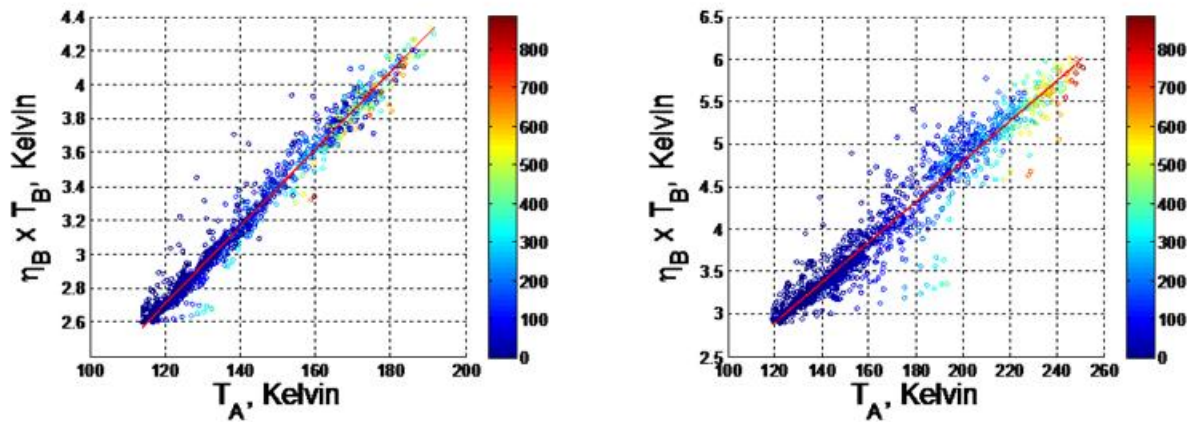


(b)

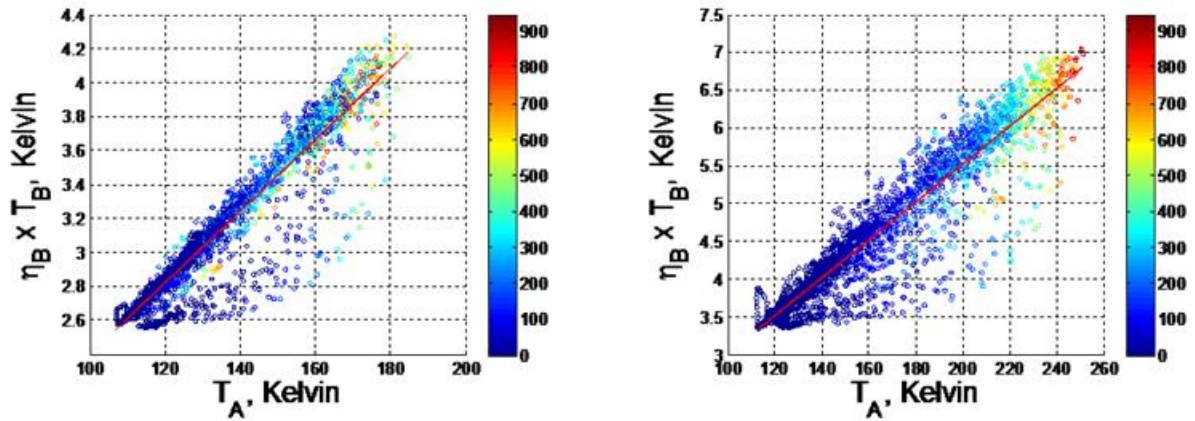


(c)

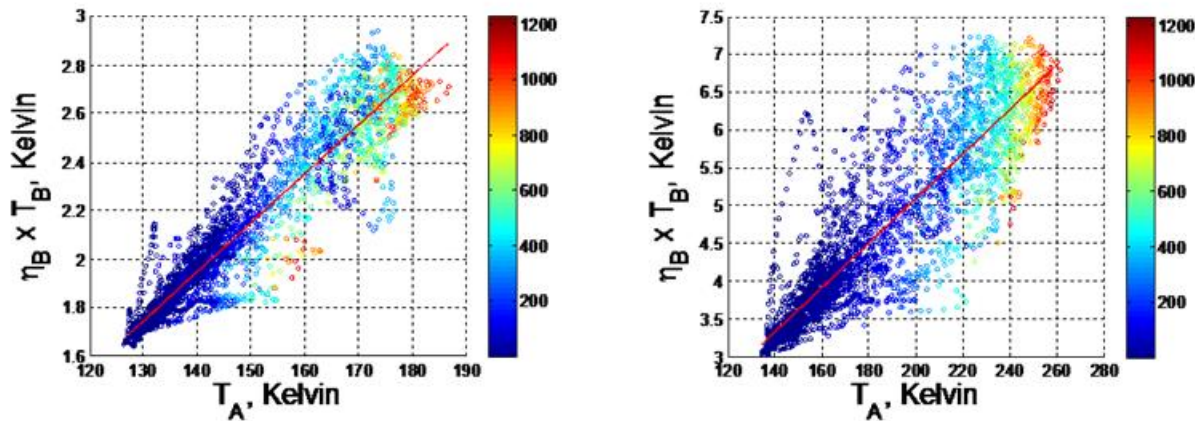
Figure 4.4 Antenna sidelobe brightness contributions above the antenna boresight for 4 GHz (left panel) and 6.6 GHz (right panel) for (a) Nadir, (b)  $\pm 30$  deg and (c)  $\pm 60$  deg. The color-bar refers to the integrated rain rate km-mm/hr.



(a)



(b)

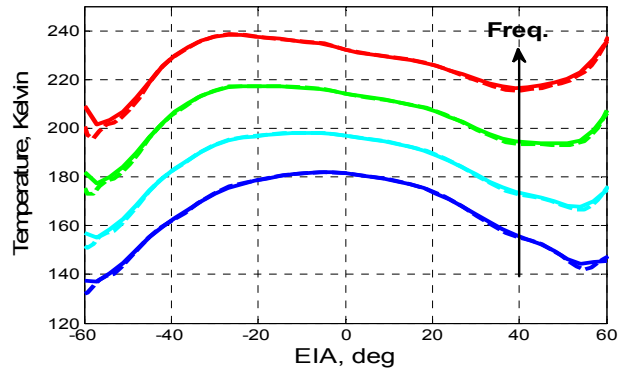


(c)

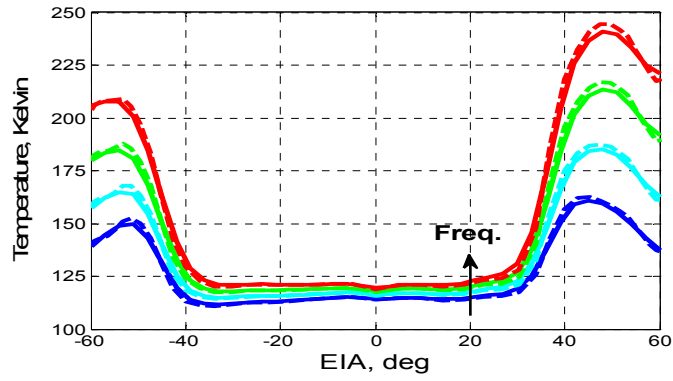
Figure 4.5 Antenna sidelobe brightness contributions below the antenna boresight for 4 GHz (left panel) and 6.6 GHz (right panel) for (a) Nadir, (b)  $\pm 30$  deg and (c)  $\pm 60$  deg. The color-bar refers to the integrated rain rate values km-mm/hr.



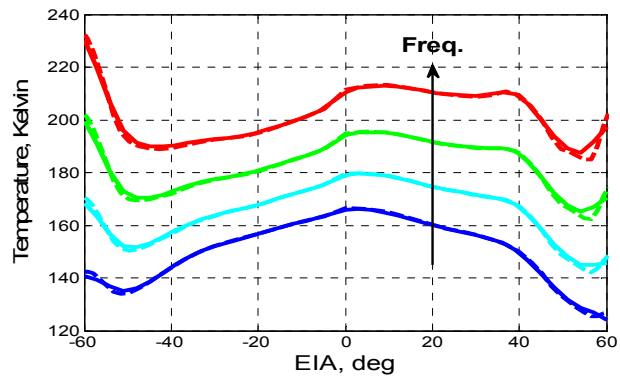
The corrected brightness temperature,  $T_{\text{corr}}$ , (solid lines), for the basic three scans described earlier in chapter 3, are shown in Fig. 4.6 for all 4 frequencies. Also shown, for comparison purposes, is the true horizontal apparent brightness temperature,  $T_{\text{aph}}$ , (dashed lines) that is computed in the forward model. Overall the antenna pattern correction algorithm is very effective, and the remainder error is negligible for incident angles  $< 40$  deg. However, above this EIA, there is a small error ( $< 2$  K) that is most likely associated with the large cross-pol coupling.



(a)



(b)



(c)

Figure 4.6 Comparison between  $T_{\text{corr}}$  (solid line) and  $T_{\text{aph}}$  (dashed line) at all frequencies for cross-track brightness temperature scenes(a) scan 1, (b) scan 2 and (c) scan 3.

## 4.2 Atmospheric Treatment

The retrieval algorithm RTM is slightly different than the forward RTM model used in the simulation. First, the hurricane climatology atmosphere vertical profiles used in the retrievals vary radially with distance from the eye. This is in contrast with the simulated forward model, where the atmosphere varies both horizontally and vertically in a 3D sense as described earlier in Chapter 3. Further, there is a major difference in the treatment of rain; where the height of the rain is fixed at a constant freezing level of 5 km in the retrievals as shown in Fig 4.7. On the other hand for the forward RTM, the rain height from the hurricane numerical weather model varies and the upwelling and downwelling  $T_b$  components are calculated along different slant paths. Also for the retrieval RTM, the sea surface temperature is assumed to be a constant value of 28 Celsius in comparison to the actual SST image used in the forward simulation.

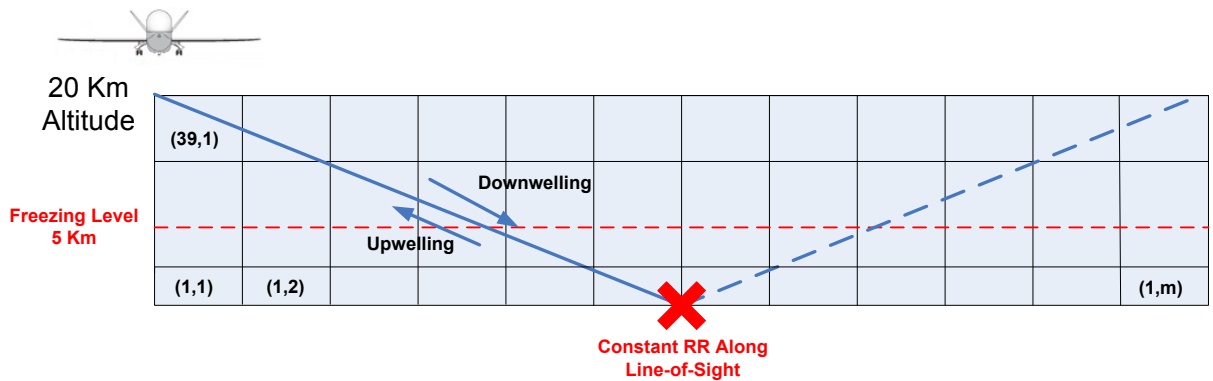


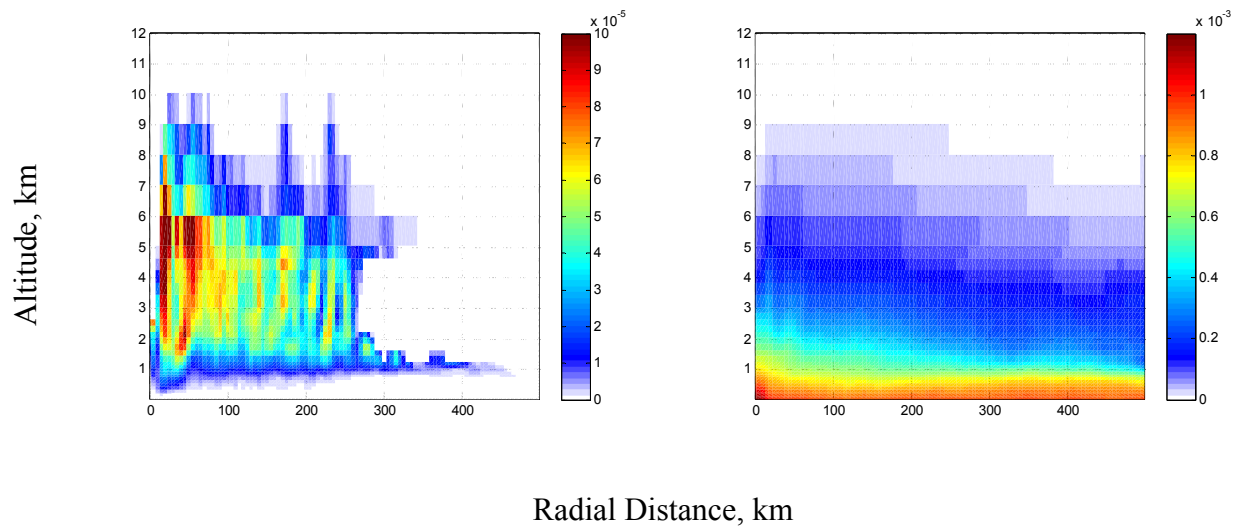
**Figure 4.7 Retrieval radiative transfer model for calculating rain emission.**

To calculate the atmospheric absorption coefficients, *a priori* hurricane climatology environmental parameters were developed using the 3D atmosphere (described in Chapter 3)

generated from the hurricane MM5 model. The atmospheric data (temperature, water vapor density and cloud liquid) were averaged in the 39 layers over radial annuli of 5 km increments. Each annulus was assigned the mean value of the vertical profile and the resultant water vapor and cloud liquid water absorption coefficient profiles in Np/km are shown in Fig. 4.8.

Knowledge of the cross-track pixel latitude and longitude is used to calculate the radial distance, which provides the corresponding atmospheric profile for water vapor and cloud liquid water. This allows the retrievals to be calculated at surface locations corresponding to the antenna beam IFOV centers.

For rain, the absorption coefficient is computed according to the power law relation given earlier by (3.8). In the retrievals, rain is assumed constant along the slant path from the 5 km freezing height to the surface.



(a) (b)  
**Figure 4.8 Hurricane atmosphere climatology (a) Clouds and (b) water vapor absorption coefficient profiles in Np/km averaged in 5 km annuli rings.**

Finally, the absorption coefficients are summed and used as input to the Atmospheric TUP/TDOWN model where the loss (transmission coefficient) and emission (upwelling and downwelling brightness temperature) of the atmosphere are calculated. The entire atmosphere is considered in the downwelling  $T_b$  component of the radiation while only that portion of the atmosphere between the aircraft and the surface is considered in the upwelling  $T_b$  component.

The ocean surface power reflection coefficient is used to determine the reflected  $T_{SKY}$  and the surface emission terms in (3.1). The sea water complex dielectric constant is computed using the Meissner and Wentz model [18], and this is used in the Fresnel power reflection coefficient calculation. Afterwards, the CFRSL surface emissivity wind speed model is used to compute a modified reflection coefficient as a function of wind speed, which affects the reflected  $T_{SKY}$  and the surface emission contributions [10]. Finally, these two quantities are attenuated by the atmospheric transmissivity between the surface and the aircraft altitude and then added to the

upwelling radiation term to produce the modeled apparent brightness temperature,  $T_{\text{mod}}$ , as a function of frequency, wind speed, rain rate and incidence angles. During the retrieval process: wind speed is varied in 0.1 m/s steps from 0~70 m/s, rain rate is varied in 0.8 mm/hr steps from 0~120 mm/hr, and incidence angle is varied according to the 41 antenna beams boresight between  $\pm 60$  deg to form an inversion brightness temperature matrix of  $701 \times 151 \times 41$ .

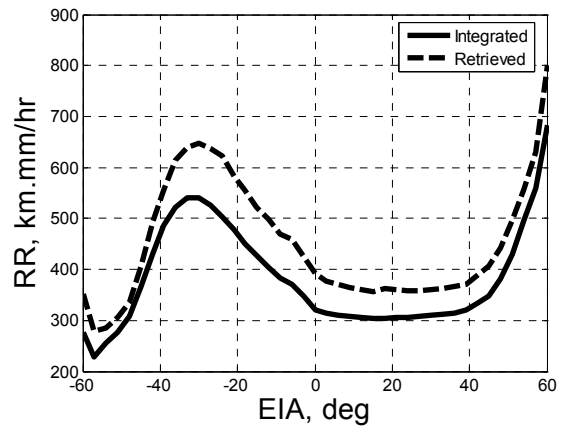
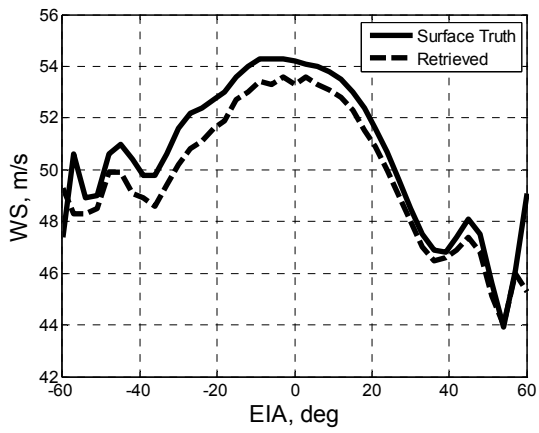
### 4.3 HIRAD Retrieval Algorithm

There are three main sources of errors that have been modeled in the retrieval module and those include the instrument  $T_b$  errors which involves the NEDT and the  $\Delta G/G$ , the aircraft attitude and the geophysical model function (emissivity model) errors. In the simplest terms, these errors are modeled as random errors that have probability distribution functions that are zero mean Gaussian. Geophysical Model Function (GMF) describes the relationship between surface emission and other geophysical parameters such as wind speed and incidence angle and the precision of the GMF directly influences the quality of the retrieved wind field. These models are usually based on the best fit to the mean of the ensembles across bins, which yield to some errors that are represented by the standard deviations across the mean in each bin. For HIRAD GMF, these errors vary with respect to wind speed and incidence angle and they include the X-Pol, imperfect antenna pattern correction and the differences in the treatment of the atmosphere and rain. For this dissertation these errors have been varied parametrically and results will be presented in Chapter 5. The Monte Carlo simulation is a well excepted procedure used in

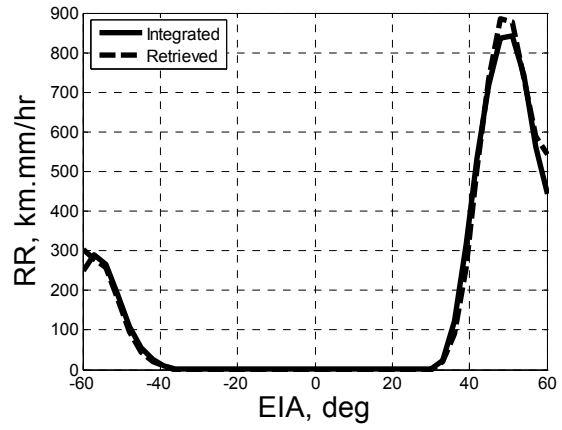
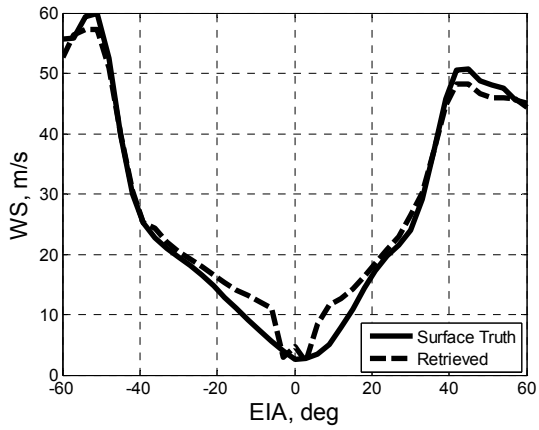
statistical analysis to characterize these effects. For this dissertation, we have chosen to represent the error as the root mean square error, which includes both the mean and standard deviation of the retrieved parameter compared to the “true” parameter (wind speed and rain rate).

The modeled brightness temperature matrix,  $T_{\text{mod}}$ , is compared to the corrected brightness temperature with random errors added ( $T_{\text{corr}} + \text{Noise}$ ) at each of the four frequencies as shown in the block diagram of Fig. 4.1. Each of the four  $T_{\text{mod}}$  vectors is compared to every value in each of the four brightness temperature matrices, forming four difference matrices. Each element in these is squared and the algorithm searches for the local minimum sum, over all frequencies, of squared difference. This process is repeated 50 times in a Monte-Carlo simulation for each beam position and used to calculate the root mean square error, RMSE.

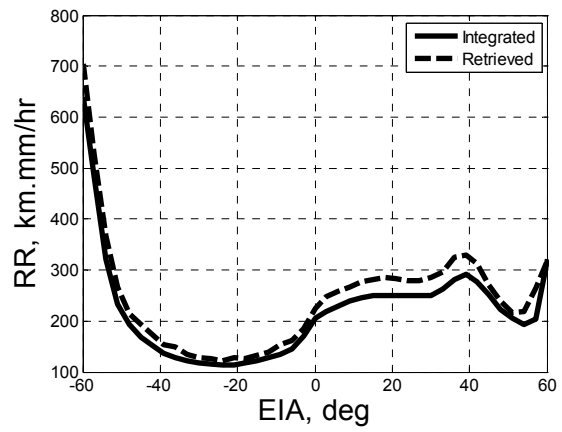
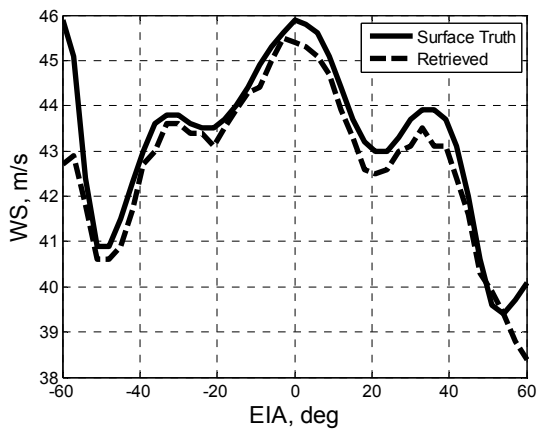
Figure 4.9 is a typical example of a retrieved set of wind speeds (left panel) and rain rates (right panel) for the same set of three scan passes through Hurricane Frances (2004). The solid lines represent the surface truth wind speed (interpolated value at the center of the antenna IFOV) and the path integrated rain rate in comparison with the dashed lines that represent the retrieved wind speeds and rain rates. The path integrated rain is the integrated rain rate along the line-of-sight path from the aircraft to the surface using the 3D rain nature run. Note that these results are for a zero random error instrument noise.



(a) Scan-1



(b) Scan-2



(c) Scan-3

Figure 4.9 Retrieved wind speed (left panel) and rain rates (right panel) for (a) scan 1, (b) scan 2, and (c) scan 3.



From the three different scans, the errors in the retrieved wind speeds and rain rates vary from one scan to the other and from one beam position to the other. For example, scan 1 shows a maximum wind speed error of 3 m/s at the edge of the swath (60 deg) while at Nadir the error is less than 1 m/s. The majority of the high wind speed errors occur at the edges of the swath as will be presented in more detail in Chapter 5. For the rain rate retrievals, errors are reasonable considering the different rain treatment between the forward and the retrieval RTM's. Our main objective in this dissertation is to retrieve accurate wind speeds in the presence of high rain, and retrieving the rain rate is a secondary objective. The sources of the wind speed errors and the complete set of retrieved wind speed and rain rate results for different aircraft Fig-4's and different random errors are presented in the next chapter. Statistics are provided in terms of RMS errors as a function of mean wind speed, integrated rain rate and incidence angle cross-track swath location).

## CHAPTER 5 : RESULTS

Methods for simulating realistic HIRAD hurricane flights; with detailed modeling of the hurricane environment, the aircraft flight path, and the HIRAD measurement, along with the HIRAD retrieval algorithm have been described in the previous chapters. This chapter includes results from applying these methods and algorithms in a Monte Carlo error analysis that simulates HIRAD measurements of observed brightness temperature, with errors, from an aircraft as it flies a pattern over the hurricane to provide images of estimated, or retrieved, wind speed and rain rate. The MM5 modeled data for Hurricane Frances was used to represent the geophysics and Fig-4 flight patterns were used to represent realistic coverage. Random errors were added to simulated HIRAD measurements of H-Pol brightness temperature, according to the forward model described earlier, with pattern corrections applied, and retrievals were done using the climatological model described in Chapter 4.

The objective of this analysis was to provide realistic imaging simulations, compile a relatively large data set of measurements, with errors, and demonstrate potential HIRAD performance over the full swath by mapping brightness temperature errors to estimates of wind speed and rain rate. Errors were treated parametrically and were not budgeted quantitatively, although the instrument errors would be expected to be 1 Kelvin or less for realistic integration times. Results are presented in this chapter for the 1 Kelvin noise case and in Appendix E for the balance of the results. In addition, the results of a noise analysis to identify the major sources of error and to quantify their significance are presented in this chapter.

## 5.1 Retrieved Wind Speed and Rain Rate Error Statistics

It appears that a single Fig-4 flight pattern, with 2 perpendicular flight legs through the eye of a hurricane 90 deg apart would adequately cover the inner portion of the hurricane and measure the maximum winds. However, to build a larger data set for this error analysis, three Fig-4 patterns were simulated, with 6 flight legs 30 deg apart, as in Fig. 5.1, and two legs outside the eye to capture high rain bands at relatively low wind speed values were added. Each flight leg is made up of 240 individual HIRAD scans, resulting in a total of 1920 scans over the HIRAD swath for the eight legs. The simulated HIRAD swath consists of 41 individual measurements of  $T_b$ , and the Monte Carlo simulation adds zero-mean Gaussian random errors, with a STD varied parametrically for 1, 2, 4 and 8 Kelvin cases, to these measurements. Fifty trials for each case and 1920 scans comprise the whole data set for the error analysis. The MM5 modeled data, serving as surface truth, is compared to the retrieved wind speed values and rain rate values and RMS errors are computed from the differences.

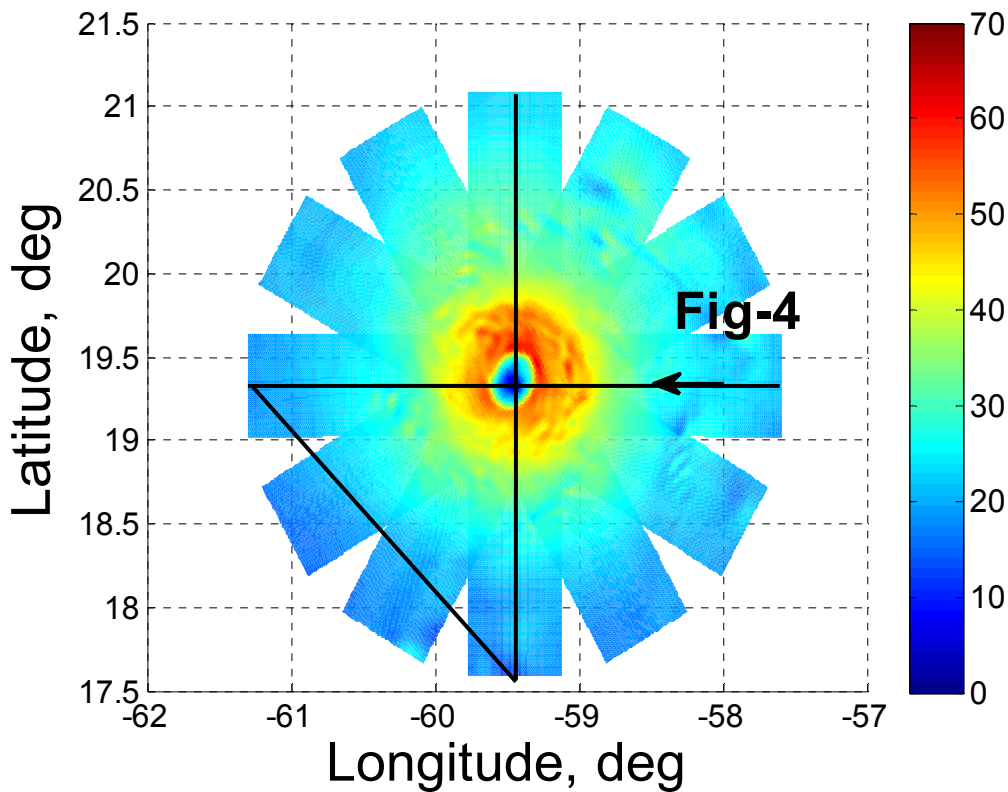


Figure 5.1 Frances simulated wind measurements for three Fig-4's.

The wind (m/s) and the integrated rain (km-mm/hr) fields for the two Fig-4 legs in Fig. 5.1 are illustrated in Fig. 5.2, where the left panel represents Leg 1 (constant latitude) and the right panel represents Leg 2 (constant longitude) with the arrow indicating the aircraft heading. Both legs are plotted on different latitude and longitude grids, as if the storm were moving during the flight, which explain the difference in the X-Y scales.

These two passes show that HIRAD would cover the eyewall region with a single Fig-4 pattern. Note that the maximum wind speed values go up to 60 m/s while the maximum integrated rain rate values reach up to about 1100 km-mm/hr at the edges of the swath, which translates to  $\sim 110$

mm/hr assuming a slant rain path of 10 km. The wind speed maximum values are located in the eyewall region of the hurricane, and even though rain exists in spiral bands that are spread more widely, the highest rain rates are located in the eye wall region also.

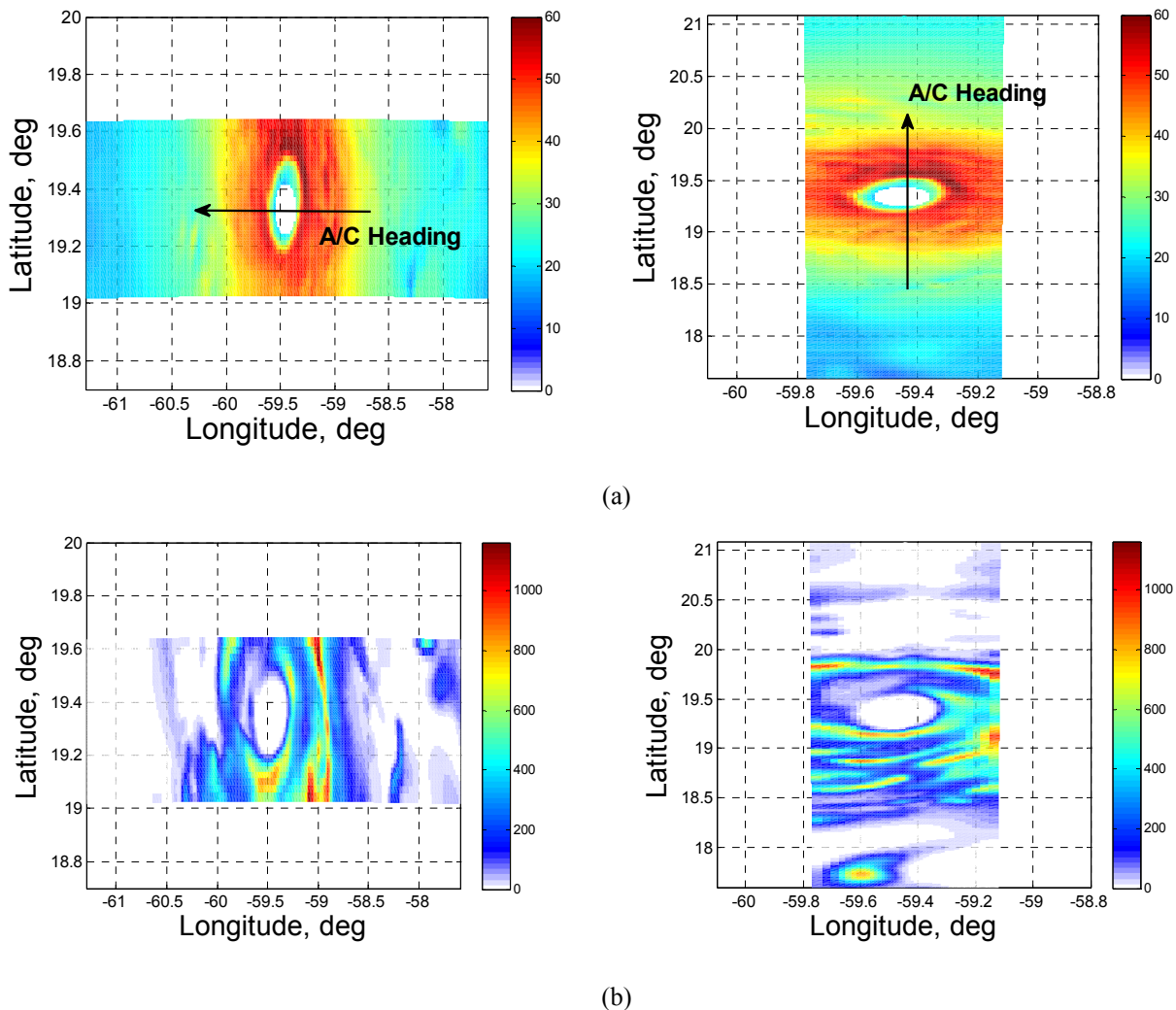
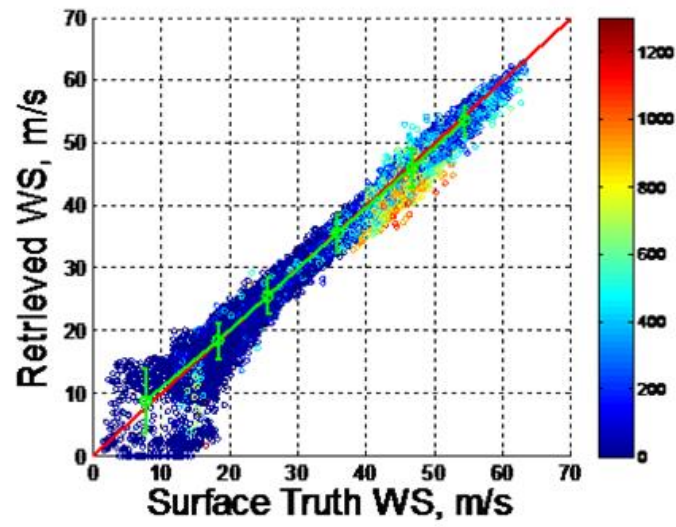


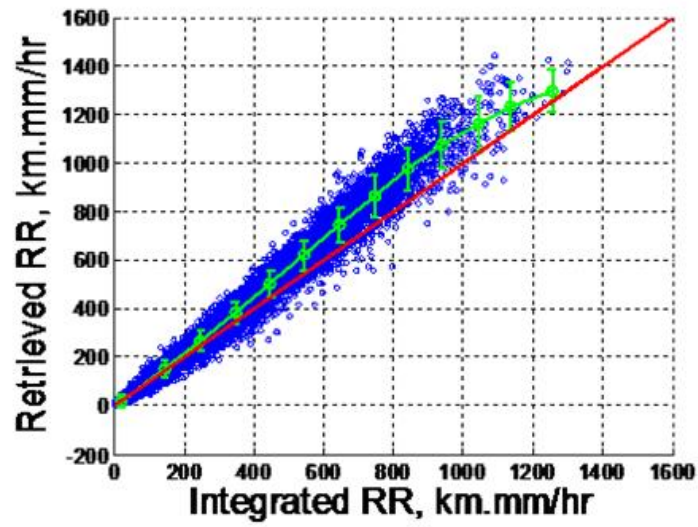
Figure 5.2 Nature run (a) wind speed (m/s) and (b) integrated rain rate (km-mm/hr) for Leg 1 (left panel) and Leg 2 (right panel).

Results for the 1 Kelvin error case are shown in Fig. 5.3 where retrieved wind speed and integrated rain rate are compared to the surface truth values for the 8 flight legs. The color-bar on

the wind speed comparison refers to integrated rain rate values in km-mm/hr. Relatively large errors in retrievals occur in the lower wind speed region due to the nature of the surface emissivity GMF in this region. Otherwise the wind speed agreement is good over the entire swath, even where heavy rain exists. The retrieved rain rate, on the other hand, is over estimated at higher integrated rain rate values, which is associated with longer slant paths (edges of swath). The corresponding histograms of differences are presented in Fig. 5.4. In general, there is good correlation between the nature run and the retrieved wind speed values. Over all wind speeds, the mean difference is much less than 1 m/s and the STD is approximately 1.5 m/s.

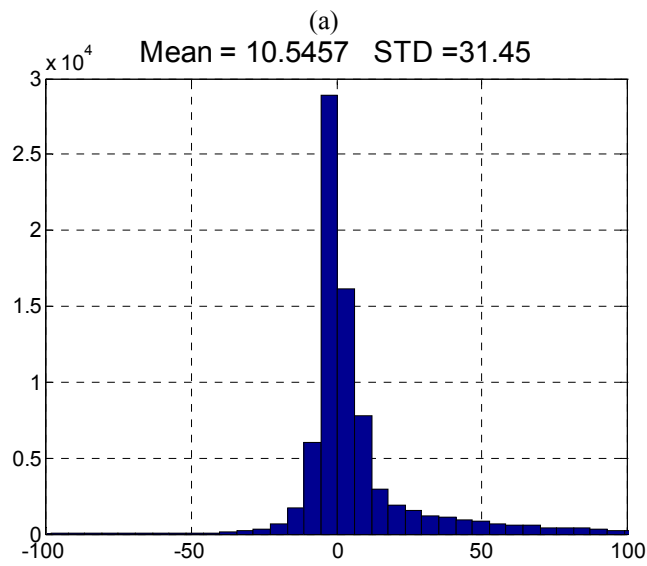
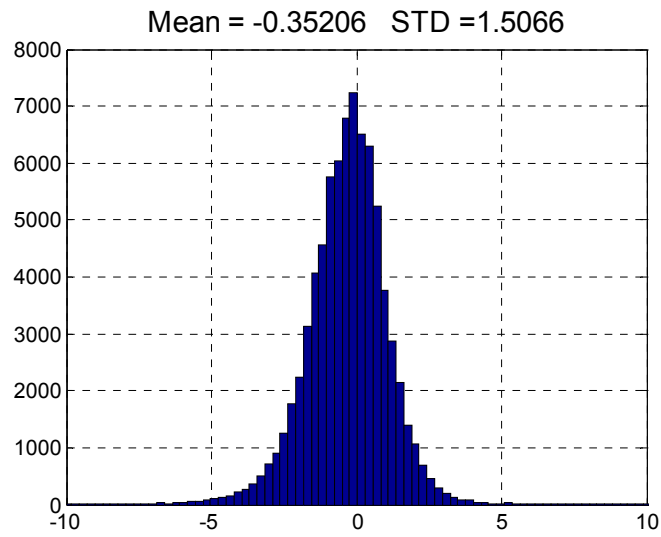


(a)



(b)

Figure 5.3 Scatter plot comparisons for (a) wind speed and (b) rain rate for eight legs.



(b)

Figure 5.4 Histograms of the differences in (a) wind speed and (b) rain rate for eight legs.



Wind speed and integrated rain rate error images are plotted for the orthogonal legs in Fig. 5.5 and Fig. 5.6 respectively where the color-bar represents the RMS retrieved error in m/s. Note that in Fig. 5.5 the highest wind speed errors are primary associated with rain bands. Also, we see the highest wind speed errors at the edges of the swath where path lengths are greatest and rain is the most intense in the eye wall region. Further, heavy rain, even in the inner swath, can cause significant wind speed errors as seen in Fig. 5.5 (a) at 59.5 deg longitude and in (b) at 17.5 deg latitude (bottom of image).

Results presented in Fig. 5.6 indicate that we are retrieving good rain rate values over most of the image where the highest errors occur at the swath edge and are approximately 50% and the higher errors in the inner swath are approximately 30%. The color-bar in Fig. 5.6 is in percent rain rate error.

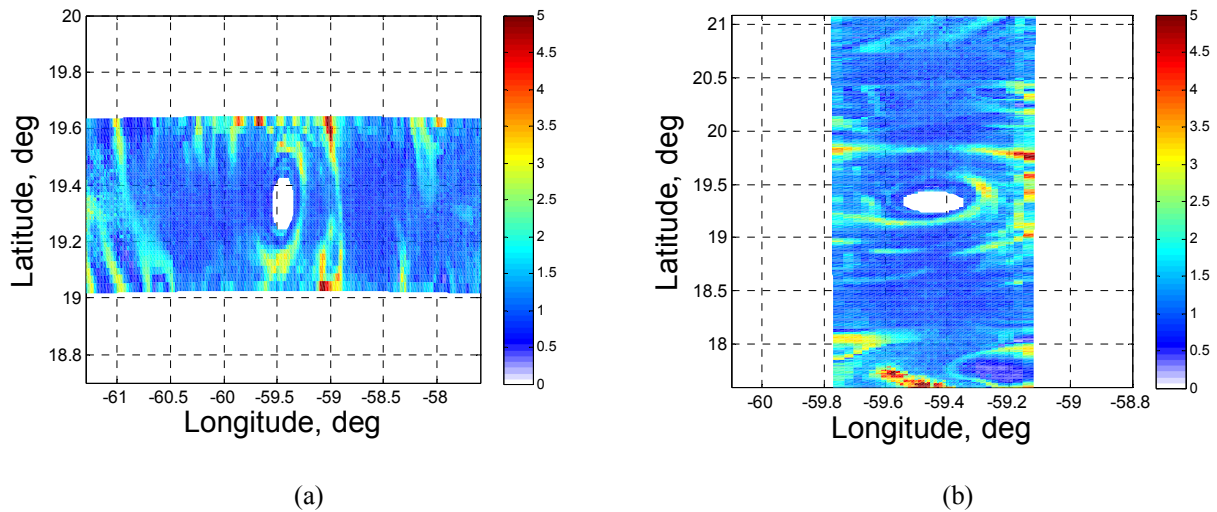


Figure 5.5 RMS retrieved wind speed errors (m/s) for (a) Leg 1 and (b) Leg 2.

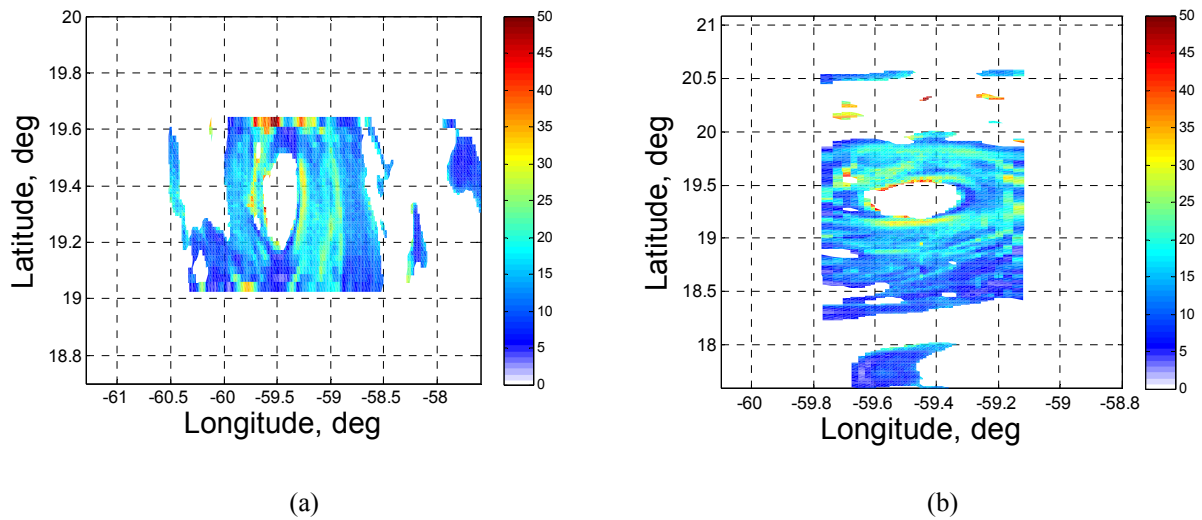


Figure 5.6 RMS retrieved integrated rain rate errors (%) for (a) Leg 1 and (b) Leg 2.

Retrieved wind speed and rain rate error statistics averaged over all wind speeds and incidence angles are summarized in Table 5.1 for the five cases of random errors. The data for 2, 4 and 8 Kelvin are taken from Appendix E. The mean error in retrieved wind speed is approximately 1 m/s or less for simulated measurement errors up to 4 Kelvin, and the STD of the error follows the 1 m/s per Kelvin rule. The mean integrated rain rate error corresponds to an average over the

path of a few mm/hr or less, depending on location in the swath. However, there are significant rain rate errors at higher rain rates, as shown in Fig. 5.3 (b) and in some images at the swath edges.

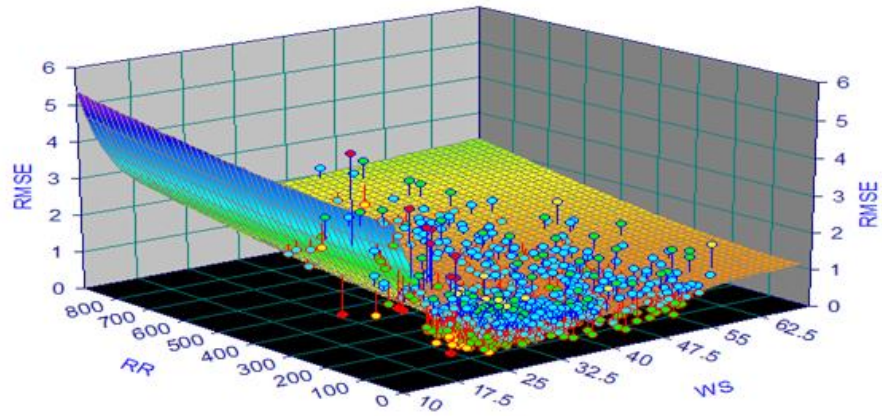
**Table 5.1 Error Statistics for All Cases**

<b>Noise Added (Kelvin)</b>	<b>0</b>	<b>1</b>	<b>2</b>	<b>4</b>	<b>8</b>
<b><i>ERROR IN RETRIEVALS</i></b>					
Wind Speed Mean (m/s)	-0.271	-0.352	-0.582	-1.165	-2.623
Wind Speed STD (m/s)	0.989	1.507	2.480	4.551	8.209
Rain Rate Mean (km-mm/hr)	10.361	10.546	11.322	13.501	22.390
Rain Rate STD (km-mm/hr)	29.243	31.450	37.664	55.155	95.563

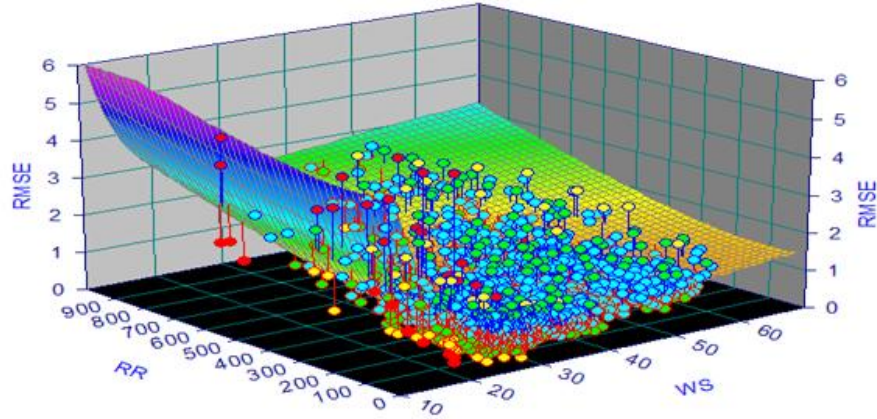
To characterize the wind speed retrieval error as a function of wind speed, rain rate and beam position (EIA), a regression analysis was performed to fit wind speed “error surfaces” in two dimensions (wind speed and integrated rain rate) for fixed incidence angles. The errors were the RMS of the Monte Carlo retrieval simulation on a per pixel basis for all cross-track scans in the eight aircraft legs. Results presented in Fig. 5.7 were computed for all eight legs, and 1 Kelvin random error, which shows the best wind speed RMSE surface fits (based on maximizing “Coefficient of Determination”) at three different beam positions; 0, 30 and 60 deg. Each symbol represents an individual estimate of the wind speed error. These symbols are color coded with blue bordered circles indicating points above the surface, red bordered circles indicating points below the surface and filled circle colors indicating the distance of these points from the surface. The magnitude of the wind speed error increases with increasing EIA, but the shape of the surface i.e., the dependence of the error on wind speed and rain rate is similar at all EIAs. As

seen in Fig. 5.3, the RMS wind speed errors, at all beam positions, are the greatest at lower wind speeds, and in general the error increases with rain rate.

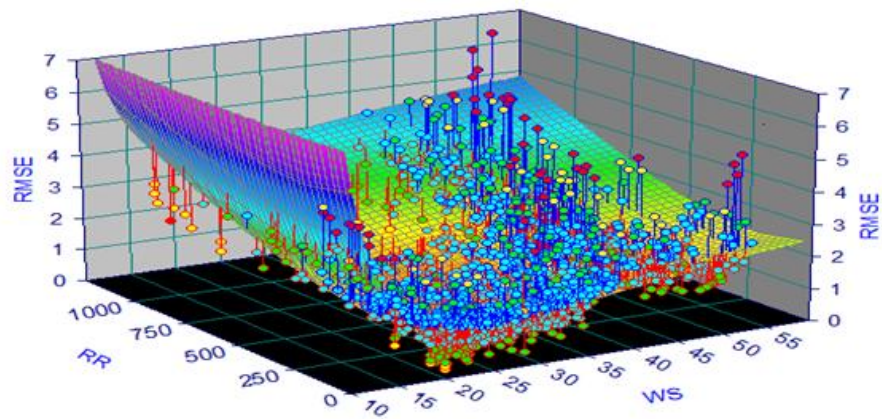
Taking constant wind speed slices of these surfaces is possibly a more useful way to look at this data. RMSE is plotted against integrated rain rate for constant wind speeds at 0 deg,  $\pm 30$  deg, and  $\pm 60$  deg in Figs. 5.8, 5.9, and 5.10, respectively.



(a) Nadir



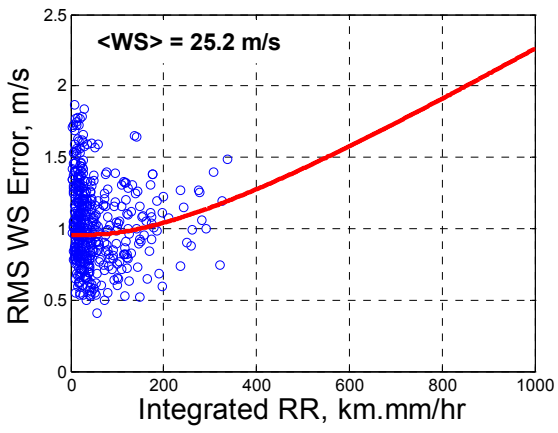
(b) 30 deg



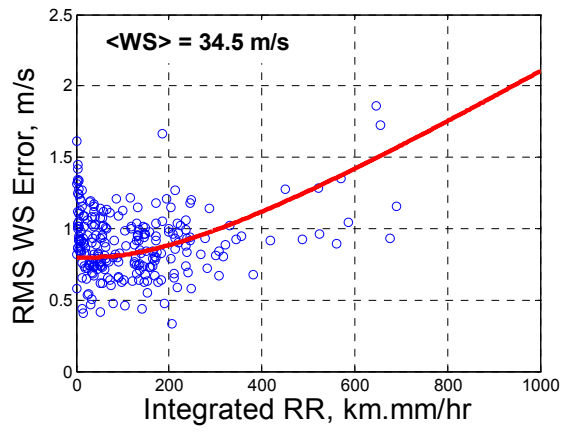
(c) 60 deg

Figure 5.7 RMS retrieved wind speed error surfaces (m/s) for (a) Nadir (b)  $\pm 30$  deg and (c)  $\pm 60$  deg.

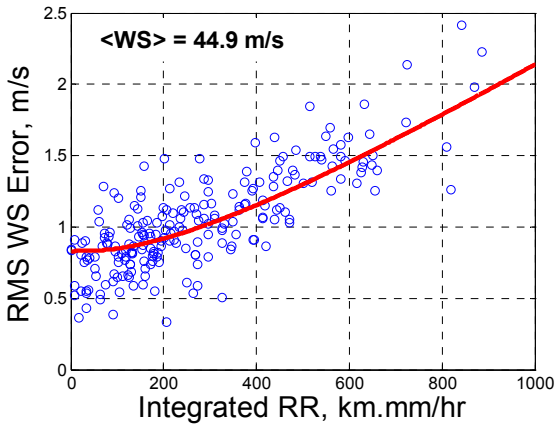
The RMS wind speed errors versus integrated rain rate scatter diagrams for wind speed bins  $\pm 5$  m/s are shown in Fig. 5.7. Along with the best surface fits, these data demonstrate that the surface fits are reasonable representations.



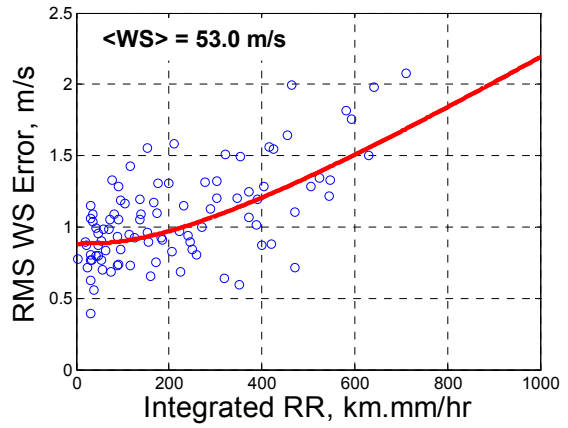
(a)



(b)

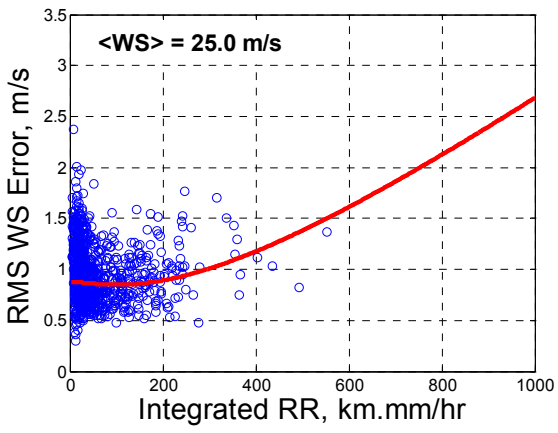


(c)

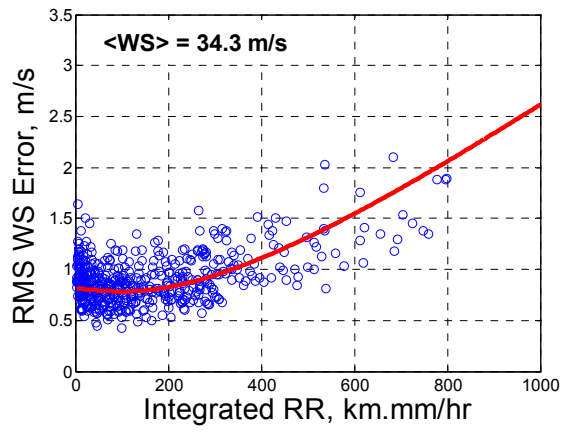


(d)

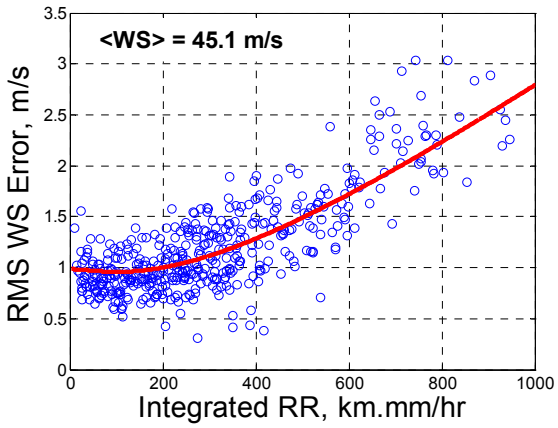
Figure 5.8 RMS wind speed errors (m/s) at Nadir for four wind speed bins  $\pm 5$  m/s.



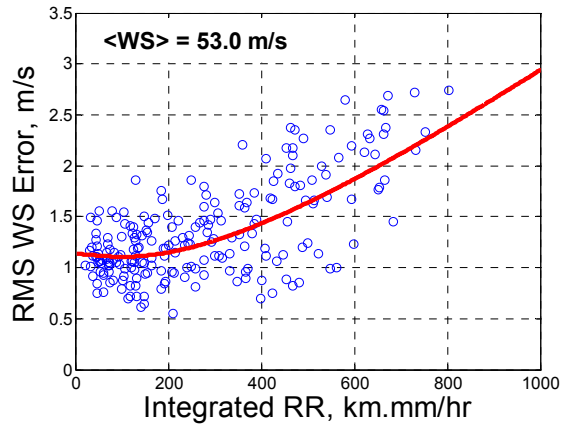
(a)



(b)



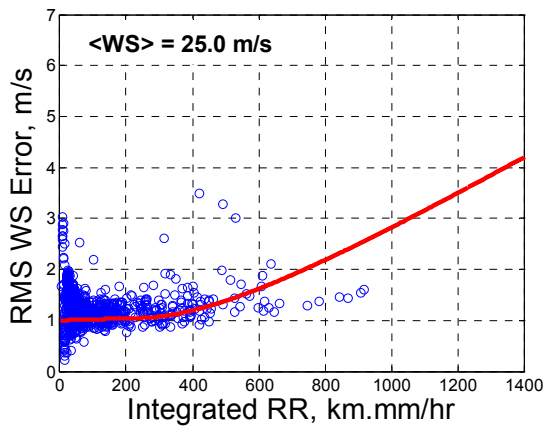
(c)



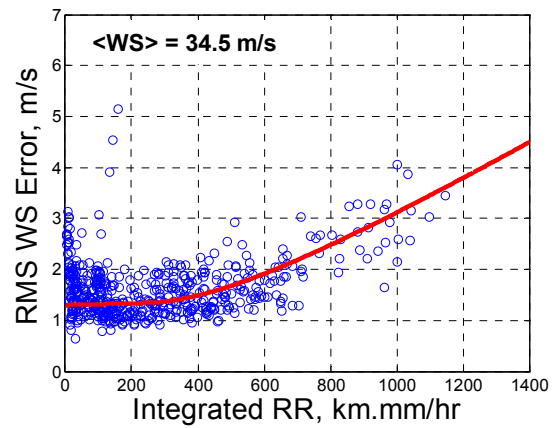
(d)

Figure 5.9 RMS wind speed errors (m/s) at  $\pm 30$  deg for four wind speed bins  $\pm 5$  m/s.

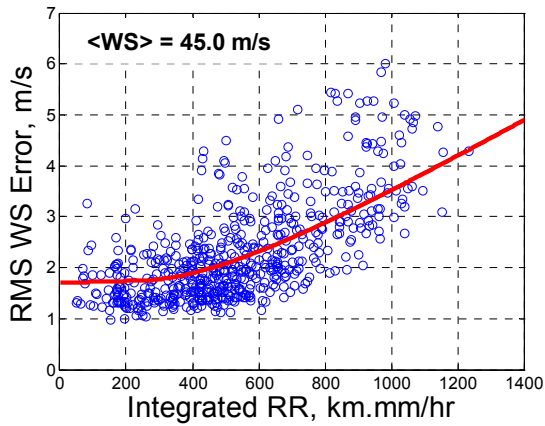




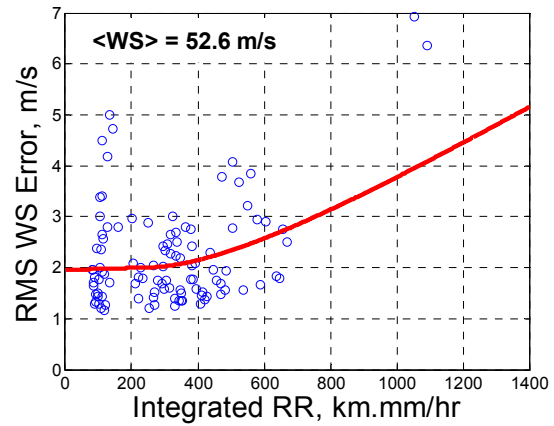
(a)



(b)



(c)



(d)

Figure 5.10 RMS wind speed errors (m/s) at  $\pm 60$  deg for four wind speed bins  $\pm 5$  m/s.

## 5.2 Individual Error Source Assessment

An understanding of each error source and its contribution to the total error in retrieved wind speed is necessary, and provides a basis for future improvements to the retrieval algorithm. The error source assessment consisted of evaluating each of the following 5 error sources individually: sea surface temperature, rain, atmosphere, antenna pattern and random errors.

In each case, we turn on one error source at a time to study its contribution to the RMS wind speed errors. Data from one leg only (constant longitude) in Fig. 5.2 is used in this analysis.

### 5.2.1 Perfect Retrieval

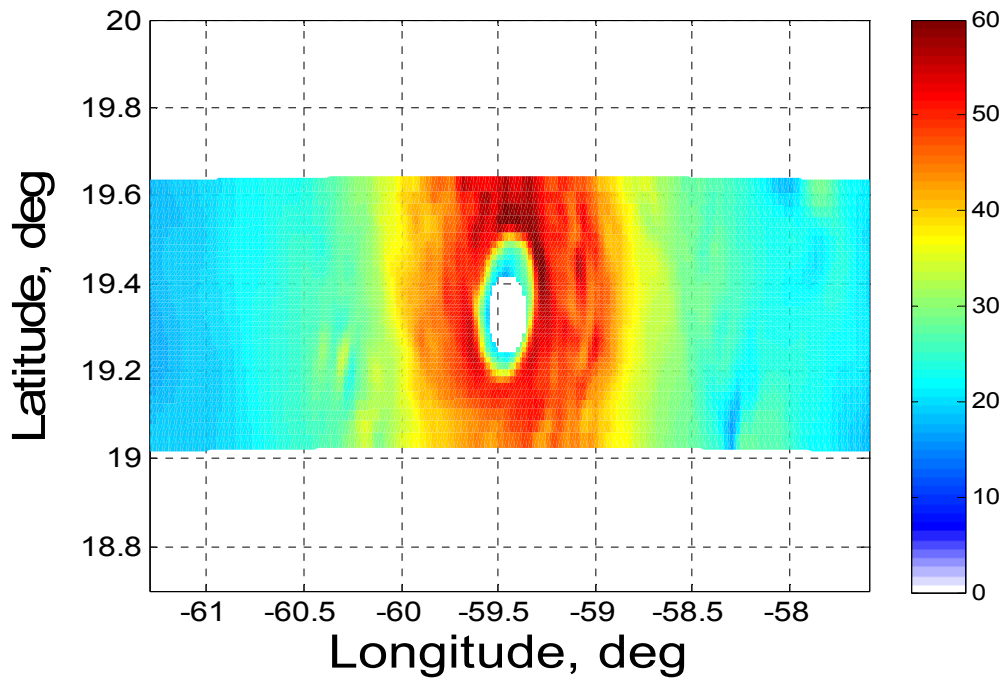
The purpose of this study is to demonstrate that an error-free retrieval will reproduce the surface truth exactly. This was done by considering a zero random error case, including no atmospheric or rain effects, adding no cross-pol or sidelobe contributions, and keeping SST constant. Therefore, as part of the forward RTM, we assume the following conditions:

- 1- Rain-free
- 2- No Atmosphere
- 3- Constant SST = 28 Celsius

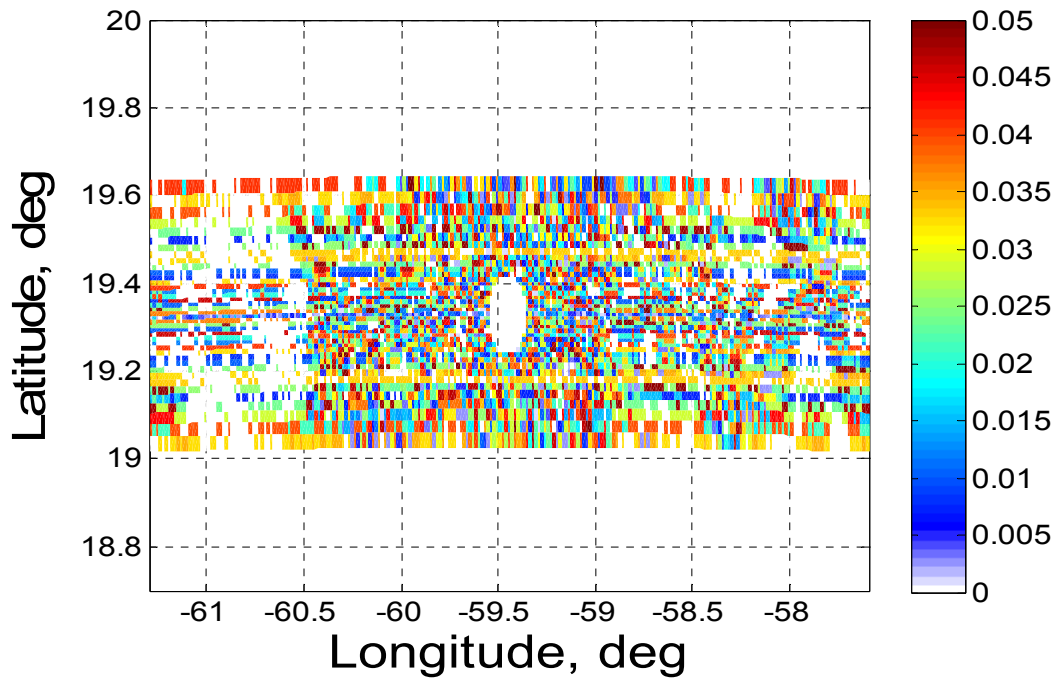
while in the retrievals, we assume the following:

- 1- No Atmosphere
- 2- No Random Errors
- 3- Perfect Antenna Correction

The simulation was run for Hurricane Frances (surface wind only) over the aircraft Leg 1, and the RMS wind speed error was plotted in Fig. 5.11 along with the corresponding surface truth wind speed. The magnitude of the wind speed errors does not go beyond 0.05 m/s which represent the quantization errors due to the wind speed step size of 0.1 m/s in the retrieval algorithm.



(a)



(b)

Figure 5.11 For Frances Leg 1 (a) Surface wind field (m/s) and (b) RMS wind speed errors (m/s).

### 5.2.2 Imperfect Sea Surface Temperature Knowledge

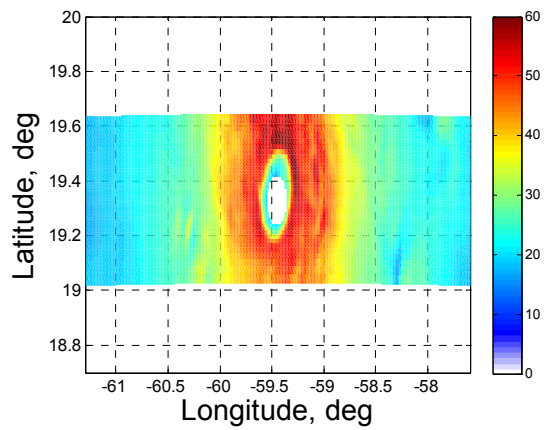
This study investigates the effect of assuming a constant SST in the retrievals compared to the real SST field used in the FWD model. As part of the forward RTM, we assume the following conditions:

- 1- Rain-free
- 2- No Atmosphere
- 3- SST 2D Field

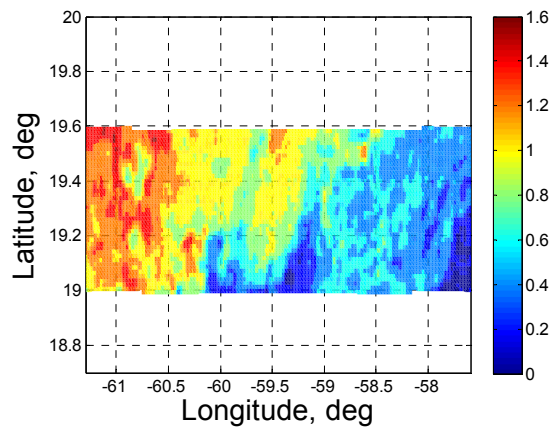
and in the retrievals, we assume the following:

- 1- No Atmosphere
- 2- No Random Errors
- 3- Perfect Antenna Correction (includes both cross-pol and sidelobe corrections)
- 4- Constant SST = 28 Celsius

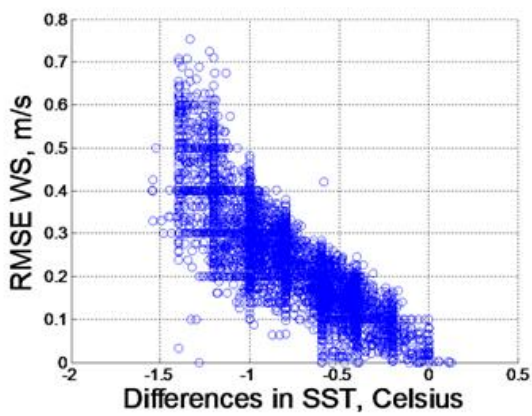
The simulation was run for Hurricane Frances (surface wind only) over the aircraft Leg 1, and the RMS wind speed error was plotted as an image in Fig. 5.12 along with the corresponding surface truth wind speed, relative SST difference image after subtracting SST = 28 Celsius and the correlation between the RMS wind speed errors and the difference in SST. The magnitude of the error is small, less than 0.5 m/s, and is maximum where there are relatively low wind speeds (less than 20 m/s) and larger SST variation. These errors included in are the statistics presented for the noise-free (zero random error) case in Table 5.1.



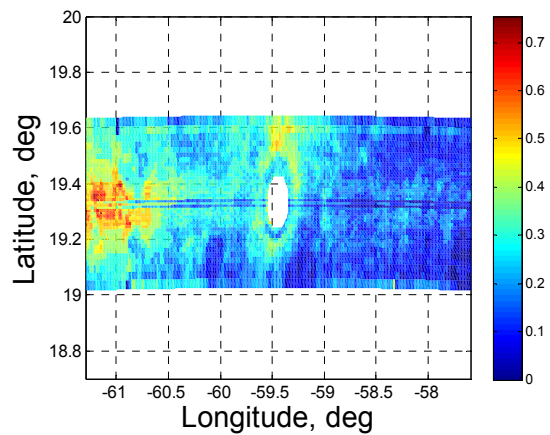
(a)



(b)



(c)



(d)

Figure 5.12 For Frances Leg 1 (a) Surface wind field (m/s), (b) relative SST difference (Celsius), (c) correlation between RMS wind speed errors and differences in SST and (d) RMS wind speed errors (m/s).

### 5.2.3 Rain Errors

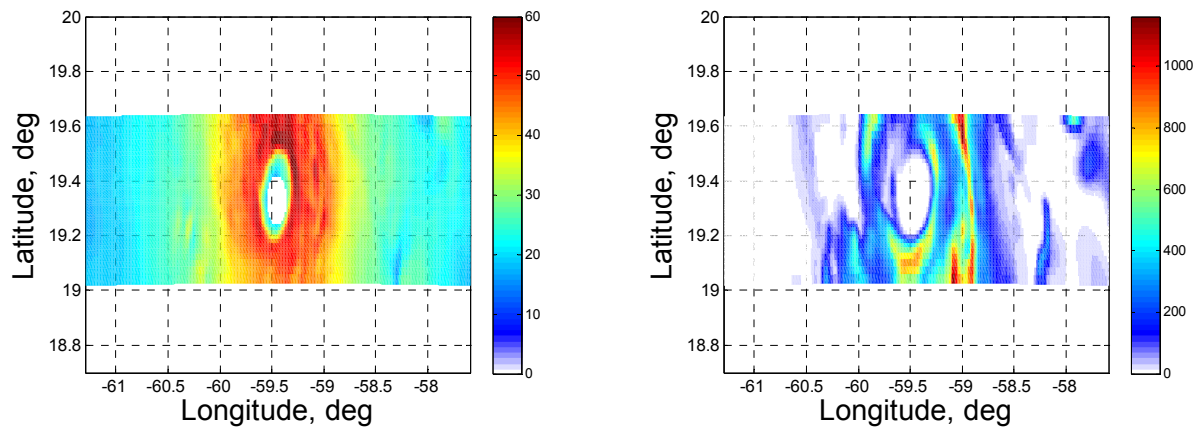
This study investigates the effect of using a constant rain rate along the antenna line of sight in the retrievals versus the true 3D variation in rain rate. As part of the forward RTM, we assume the following conditions:

- 1- Variable 3D RR
- 2- No Atmosphere
- 3- Constant SST = 28 Celsius

and in the retrievals, we assume the following:

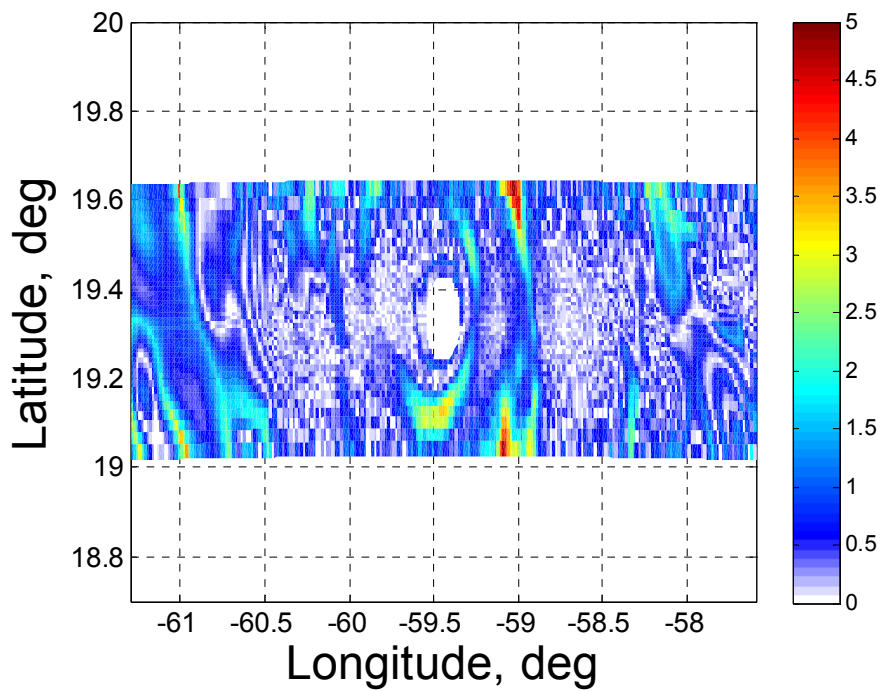
- 1- No Atmosphere
- 2- No Random Errors
- 3- Constant Line Of Sight Rain Rate
- 4- Perfect Antenna Correction

The simulation was run for Hurricane Frances (surface wind and rain rate only) over the aircraft Leg 1, and the RMS wind speed error was computed and plotted in Fig. 5.13 along with the corresponding surface truth wind speed and the integrated rain rate. The maximum errors, of 5 m/s, were in regions of heavy rain, and at the edges of the swath, which is expected due to the longest slant path. Errors of 3 m/s were seen in mid-regions of the swath with heavy rain. Near Nadir, RMS wind speed errors are due to the vertical variation in rain rate. The spatial distribution of the errors follows the rain pattern, but is also modulated by the wind speed. For example, these errors are reduced where the GMF has a strong slope,  $dT_b/dWS$ .



(a)

(b)



(c)

Figure 5.13 For Frances Leg 1 (a) Surface wind field (m/s), (b) integrated rain rate (km-mm/hr) and (c) RMS wind speed errors (m/s).

#### 5.2.4 Imperfect Atmosphere Parameter Knowledge

This study investigates the effect of using the climatological hurricane model for the atmosphere in the retrievals, rather than the true 3D atmosphere. Therefore, as part of the forward RTM, we assume the following conditions:

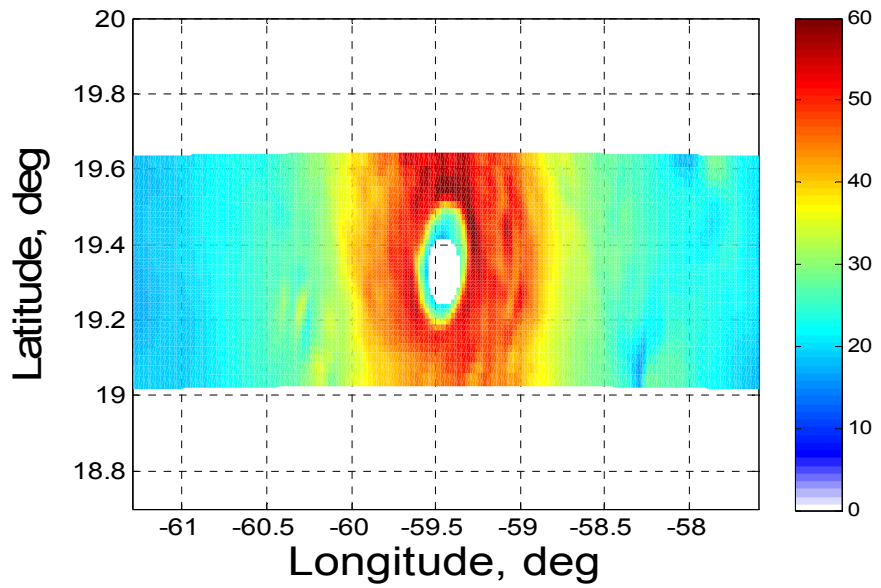
- 1- Rain-free
- 2- 3D Atmosphere
- 3- Constant SST = 28 Celsius

and in the retrievals, we assume the following:

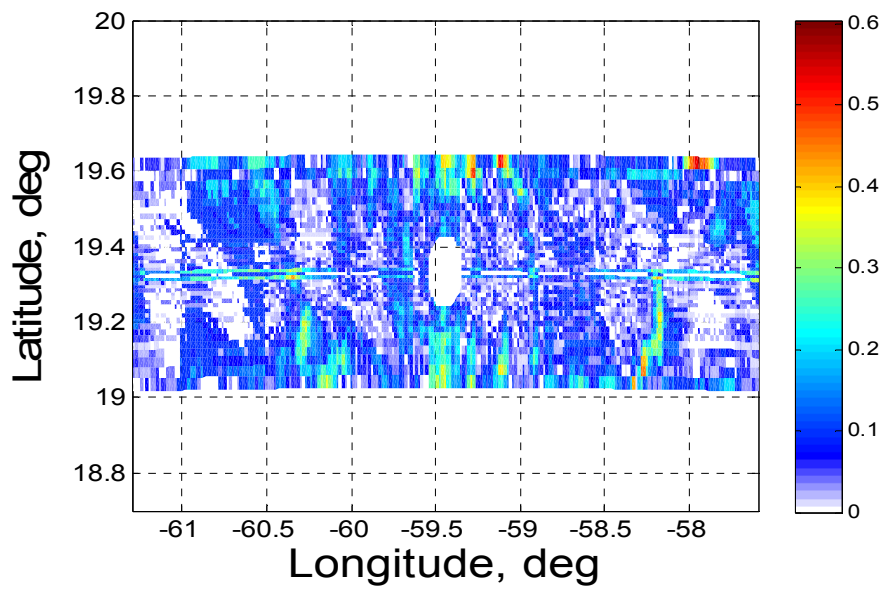
- 1- Hurricane atmosphere climatology
- 2- No Random Errors
- 3- Perfect Antenna Correction

The simulation was run for Hurricane Frances (surface wind only) over the aircraft Leg 1, and the RMS wind speed error was computed and plotted in Fig. 5.14 along with the corresponding surface truth wind speed. The magnitude of the error is small, less than 0.5 m/s, and is maximum at the edges of the swath where path lengths are the greatest. Errors of this magnitude are within the statistics presented for the noise-free (zero random error) case in Table 5.1





(a)



(b)

Figure 5.14 For Frances Leg 1 (a) Surface wind field (m/s) and (b) RMS wind speed errors (m/s).

### 5.2.5 Antenna Pattern Correction Errors

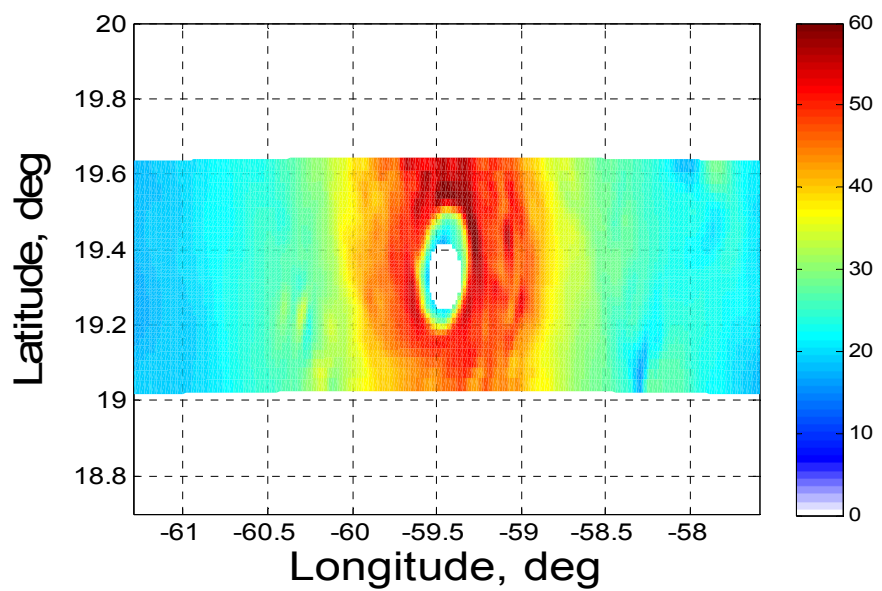
This study investigates the effect of using the algorithms developed in Chapter 4, for correcting for the cross-pol contribution and antenna pattern sidelobes, in the retrievals. Therefore, as part of the forward RTM, we assume the following conditions:

- 1- Rain-free
- 2- No Atmosphere
- 3- Constant SST = 28 Celsius

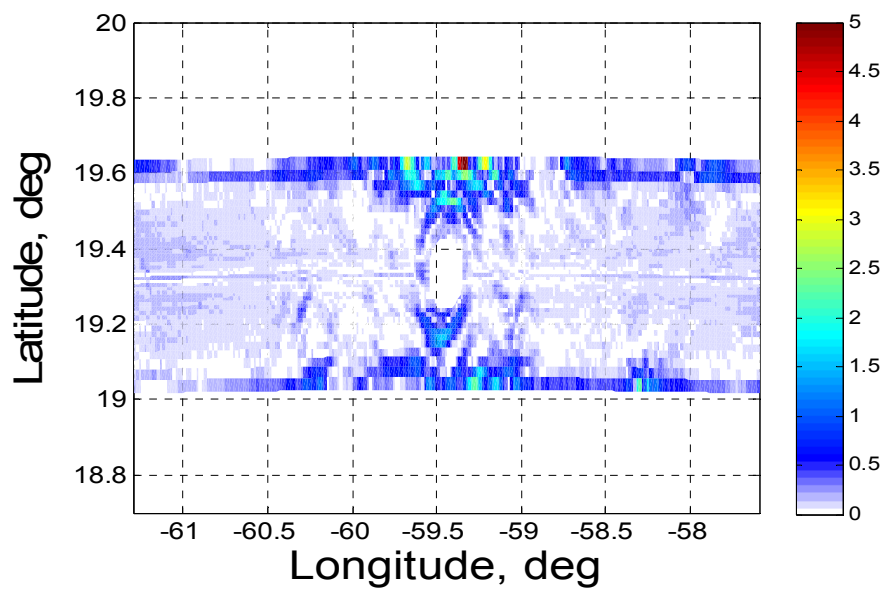
and in the retrievals, we assume the following:

- 1- No Atmosphere
- 2- No Random Errors
- 3- Antenna Pattern Correction Algorithms

The simulation was run for Hurricane Frances (surface wind only) over the aircraft Leg 1, and the RMS wind speed error is plotted in Fig. 5.15 along with the corresponding surface truth wind speed. The error is maximum at the edges of the swath due to the larger X-Pol contribution (~50%), but for the most part is between 0 ~ 0.25 m/s where the GMF has a strong slope,  $dT_b/dWS$ .



(a)



(b)

Figure 5.15 For Frances Leg 1 (a) Surface wind field (m/s) and (b) RMS wind speed errors (m/s).

### 5.2.6 Random Errors

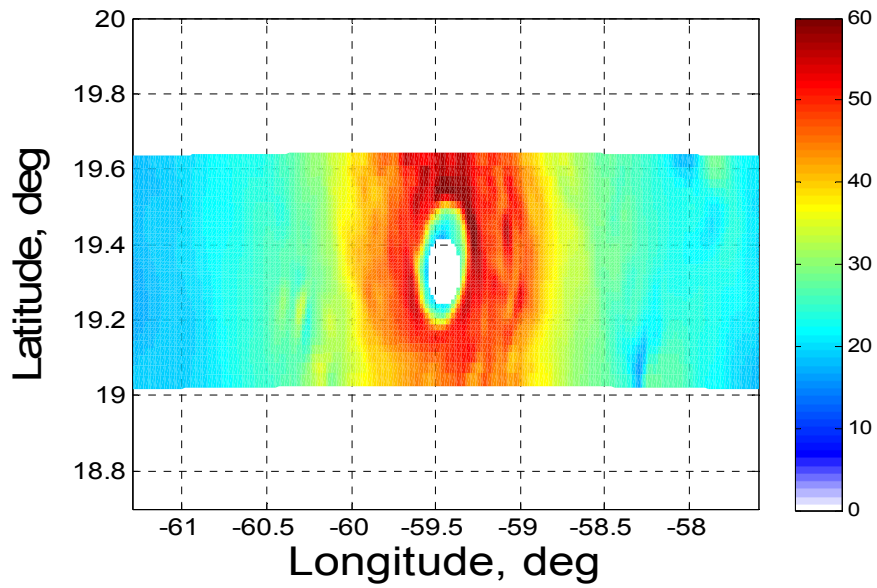
The purpose of this study is to demonstrate the effect of adding random error to the simulation. This was done by adding random errors of 1 Kelvin, including no atmospheric or rain effects, adding no cross-pol or sidelobe contributions, and keeping SST constant. Therefore, as part of the forward RTM, we assume the following conditions:

- 1- Rain-free
- 2- No Atmosphere
- 3- Constant SST = 28 Celsius

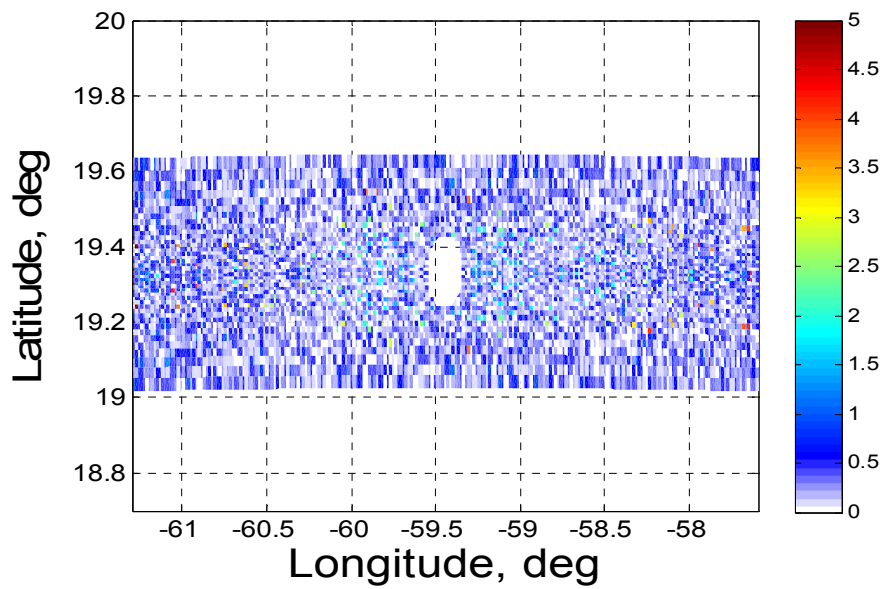
and in the retrievals, we assume the following:

- 1- No Atmosphere
- 2- Random Errors Included
- 3- Perfect Antenna Correction

RMS wind speed error was computed and plotted in Fig. 5.16 along with the corresponding surface truth wind speed. The error follows a uniform trend across the whole swath. There are no visible patterns other than the hurricane eye. The errors are less than 1 m/s and there are no edge of swath or path length dependent features. It is expected that at lower wind speeds ( $< 20$  m/s), the RMS wind speed errors will increase due to the nature of the GMF.



(a)



(b)

Figure 5.16 For Frances Leg 1 (a) Surface wind field (m/s) and (b) RMS wind speed errors (m/s).

As a result, we can clearly identify that the major sources of error are the difference in treatment between the forward and reverse algorithms, particularly the rain treatment and the correction for X-Pol effects. To overcome these error sources, an improved retrieval algorithm is needed for rain, which will minimize the error at larger path lengths (higher EIA's). Also, improvement in the HIRAD antenna X-Pol performance and modified Dual Pol retrievals would both reduce X-Pol errors.

In this chapter, results for running different passes through hurricane Frances were presented for a 1 Kelvin random error case and the other random error cases are covered in Appendix E of this dissertation. Wind speed retrieval errors were identified as a function of wind speed, rain rate and EIA where results showed that the maximum RMS wind speed errors are mostly associated with high rain rates at the edges of the swath. Conclusions and future work will be covered in the next chapter.

## CHAPTER 6 : CONCLUSION

### 6.1 Summary and Conclusion

This dissertation develops a comprehensive computer simulation for the Hurricane Imaging Radiometer, HIRAD, which is being developed to provide observations of the wind speed and rain rate in hurricanes. Therefore, the significance of this dissertation is developing an “engineering tool” not only for evaluating the HIRAD performance, but also a tool that sets a basis for data processing retrieval algorithms.

HIRAD is a Synthetic Thinned Array Radiometer that is expected to be the next generation hurricane surveillance instrument. The motivation for this work was the evaluation of the hurricane wind speed and rain rate measurement performance capability of HIRAD, with emphasis on the array antenna performance and the geophysical retrieval algorithm performance. This work is a significant advancement in the quality of simulations that have been performed previously for the HIRAD project. It utilizes 3D realistic hurricane atmosphere climatology along actual flight patterns in hurricane Frances, and it also includes a thorough study of potential random error sources and their effect on the quality of the retrieved wind speed and rain rate.

The Hurricane Imaging Radiometer, HIRAD, instrument concept has the potential to improve on the state of the art for hurricane surface wind speed measurements currently provided

by the Stepped Frequency Microwave Radiometer, SFMR. This improved capability to provide a wide swath measurement compared to the SFMR nadir viewing profile of brightness temperature has very significant positive impact on hurricane surveillance. HIRAD is a synthetic aperture interferometric radiometer that will provide measurements over a swath equal to three times the aircraft altitude and will yield images of hurricane surface wind speed and rain rate that covers the hurricane eye wall region in 2 passes from a 20 km altitude. Further, these simulations demonstrate the challenges associated with the HIRAD retrieval algorithm in making these wide swath measurements.

The HIRAD simulation is composed of a forward radiative transfer model, to calculate realistic brightness temperature measurements and a statistical least-squares difference inversion algorithm. In hurricanes, the importance of rain and atmospheric contributors, such as water vapor and cloud liquid water, on radiometric brightness temperatures in the modeling and retrieval of geophysical parameters in hurricanes have been observed. Therefore, for a wide swath measurement, a 3D treatment of these atmospheric components and rain has been included in the forward RTM for the simulation. The retrieval algorithm was based on the HIRAD geometry and the basic HIRAD antenna design. Nature, or surface truth, was represented using the MM5 numerical model for wind and rain fields for hurricane Frances, 2004.

Monte Carlo error studies were conducted for simulated HIRAD surveillance flights in hurricane Frances. Eight flight lines, for 1,920 total HIRAD scans, were simulated to provide complete images of Frances with brightness temperature errors of 1, 2, 4, and 8 Kelvin applied.



The modeled surface truth and the simulated retrievals were compared and the resulting differences, or root mean squared errors, RMSE for wind speed in the presence of rain were computed. It was observed that the retrieved wind speed compares well to the surface truth over most of the swath. Antenna pattern effects and limitations to the treatment of rain in the retrieval algorithm did result in some significant wind speed errors, usually near the edges of the swath ( $\pm 60$  deg). The wind speed retrieval error was further characterized as a function of wind speed, rain rate and beam position, by computing wind speed error surfaces. These relationships showed that the magnitude of the wind speed error increases with increasing EIA, and the shape of the dependence of the error on wind speed and rain rate is similar at all EIAs. The RMS wind speed errors are the greatest at lower wind speeds, due to the shape of the surface emissivity GMF, and this is true at all beam positions. The increase in the error as rain rate increases is also shown.

## 6.2 Future Work

The near-term benefit of the HIRAD aircraft instrument will be as a useful addition to the suite of aircraft and satellite sensors used by NOAA in hurricane surveillance, and by NASA and NOAA in tropical cyclone research. In the long term, HIRAD technology has potential to grow to a dual polarization wind vector measurement capability, with the same large dynamic range in wind speed, and with the complementing rain measurement. Also, the passive microwave frequencies employed by HIRAD will produce imagery of sea surface temperature under cloudy

and lightly precipitating skies, and may be useful in making vegetation canopy corrections to soil moisture measurements.

The HIRAD flight instrument was tested in recent engineering flights aboard the NASA B-57 aircraft and is approved to participate in a NASA science flight program during the 2010 hurricane season. Four engineering flights were successfully conducted in March 2010, in the Gulf of Mexico under relatively benign weather conditions. The data gathered on these flights will allow a functional evaluation of the instrument and a partial test of the retrieval algorithm. The simulations in this dissertation provided a rigorous evaluation of the geophysical retrieval algorithm, and future flights will be used to further develop it. Critical areas for future development during the HIRAD flights are both the  $T_b$  image reconstruction algorithms and the geophysical retrieval algorithm, and UCF will be responsible for the latter. The main components of the retrieval algorithm to be improved have been identified in these simulations. Extended retrieval algorithm development will be required as part of the future dual-pol instrument development. It is hoped that HIRAD has a long future.

## APPENDIX A. SYNTHETIC THINNED ARRAY RADIOMETER (STAR)

### A.1 Aperture Taper and Pattern Shaping

Design studies have been conducted using various image reconstruction algorithms as part of the HIRAD development [19]. The visibility terms that represent the radiometer measurements are computed from,

$$V = G \times T_b \tag{A.1}$$

$(N \times 1)$      $(N \times P)(P \times 1)$

where  $N$  is the total number of visibilities,  $P$  is the number of pixels in the scene, the matrix ‘ $G$ ’ characterizes the array, and brightness temperature,  $T_b$ , represents the actual brightness temperature scene [11, 19]. The reconstructed  $T_b$  scene is given by,

$$\hat{T}_b = G^{-1} \times V \tag{A.2}$$

where  $\hat{T}_b$  is the estimated brightness temperature and  $G^{-1}$  represents the matrix inversion that minimizes the difference between the estimated and actual brightness temperature scenes [19]. For simulation purposes, substituting the expression for the visibility term, the relationship between the actual scene and the measured scene is given by,

$$\hat{T}_b^{(P \times 1)} = \left( G' \times G \right)^{(P \times P)} T_b^{(P \times 1)} \quad (\text{A.3})$$

and  $G' \times G$  represents the synthesized antenna patterns. Each row in  $G' \times G$  is a complete pattern at a particular boresight angle.

Various aperture taper functions, or spatial filters, were used to weight the HIRAD  $G$ -matrix in simulating visibility measurements and in computing image reconstructions of  $T_b$ . Aperture tapers weight the individual visibilities and, effectively, shape the synthesized array patterns, decreasing the sidelobe levels while broadening the main beam. In simulations, selected tapers were applied directly to the  $G$ -matrix according to,

$$G_{P\_Taper}^{(N \times 1)} = G^{(N \times 1)} \times Taper^{(N \times 1)} \quad (\text{A.4})$$

Synthesized patterns at 0 and 60 deg boresight for the uniform, triangular and Blackman tapers are shown in Fig. A.1 for 6.6 GHz. The uniform taper is just unity weighting for each element ( $N$ ), the triangular varies linearly from unity at the lowest spatial frequency to zero at the highest, and the Blackman has a somewhat sharper roll-off.

Figure A.1 shows that at 0 deg boresight, the uniform taper has a -6.65 dB first side-lobe level, the triangular taper -13.3 dB, and the Blackman taper -28.92 dB. At 60 deg, the first side lobe levels were -6.3 dB, -11.8 dB, and -26.7 dB, for the uniform, triangular, and Blackman tapers, respectively. The Blackman taper beamwidth is approximately twice that of the uniform taper for both 0 and 60 deg boresight.

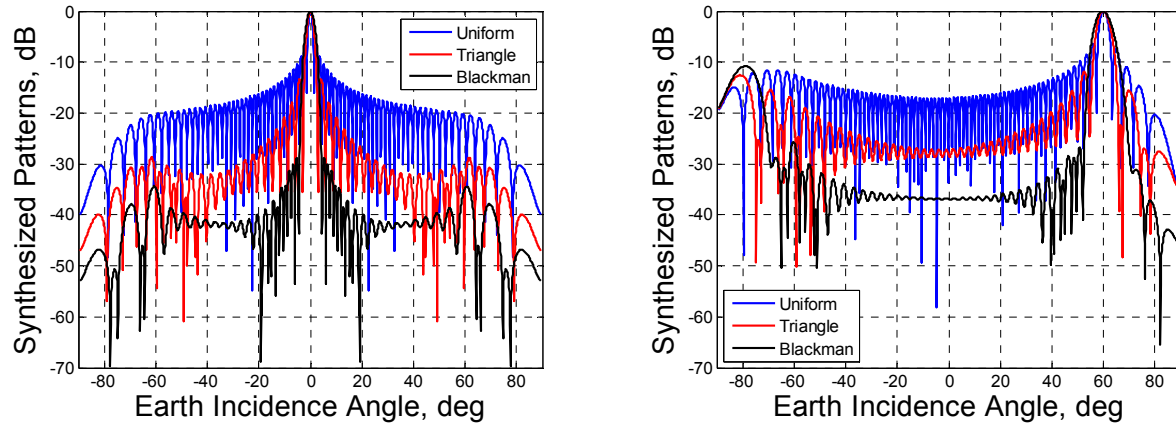


**Figure. A.1 Synthesized antenna patterns for uniform, triangular and Blackman tapers at 6.6 GHz.**

### A.2 Image Reconstruction Simulations

The modeled hurricane used in the simulations includes an eye-wall, rain-bands and other realistic structure with a horizontal grid spacing of 0.015 degrees ( $\sim 1.7$  km) in longitude and latitude for the innermost portion of the storm, including the entire eyewall region. The HIRAD simulation constructs cross-track scans every 3 degrees, and contiguous scans along the track [20].

Figure A.2 shows three typical HIRAD scans simulated from 20 km altitude. The first scan is taken outside the eyewall region (lower right) where the brightness temperature across the swath is uniform, the second scan (middle) is through the center of the eye and the last scan is in the eyewall region (upper left) where the highest winds occur. The three scans will be referred to

as scan 1, 2, and 3, respectively, and the star symbol represents the scan nadir point. The swath width is approximately 70 km at the 20 km altitude.

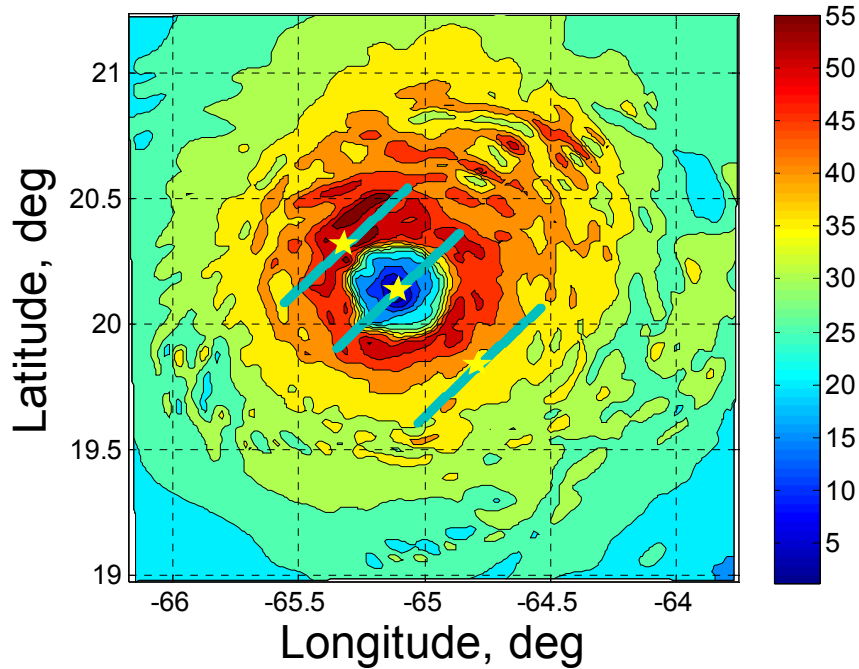


Figure. A.2 Frances wind field (m/s), HR 24, 31 August, 2004.

The uniform, triangular and Blackman tapers were applied to the  $G$ -matrix at each frequency for each of the 3 scans, and the HIRAD forward radiative transfer model [21] was used to compute brightness temperature. Figure A.3 shows the computed  $T_b$ 's as a function of earth incidence angle for the three different scans, for each taper.

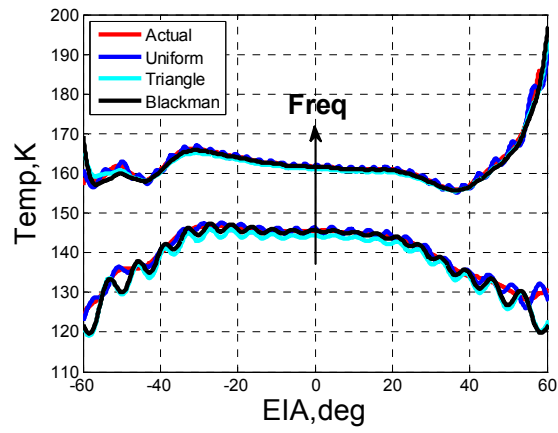
The uniform taper is shown to have the best match with the actual brightness temperature over the swath. Results also show the Gibbs phenomenon ringing, with generally increasing amplitude as frequency decreases and maximum amplitude at the swath edges, as expected. The

brightness temperature profiles for the triangular and Blackman tapers usually underestimate the actual brightness temperature by as much as ~10 Kelvin in the outer swath.

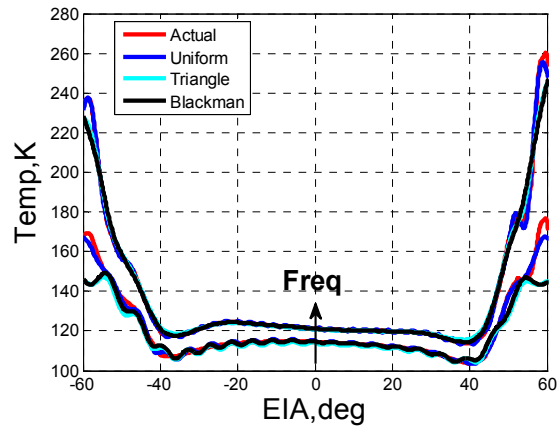
While computing the reconstructed image, or estimated brightness temperatures, the matrix in the inverse operation in (A.4) can be “ill-conditioned” causing the inversion to become unstable, and additional information must be introduced into the solution. This process is known as “regularization” and is necessary to obtain a usable inverse. For example, the least square method used in these simulations requires a very simple form of regularization. In (A.5) an additional small value, the regularization number,  $\alpha$ , was added along the diagonal of the  $G \times G^t$  matrix according to,

$$(GG^t + \alpha I) \tag{A.5}$$

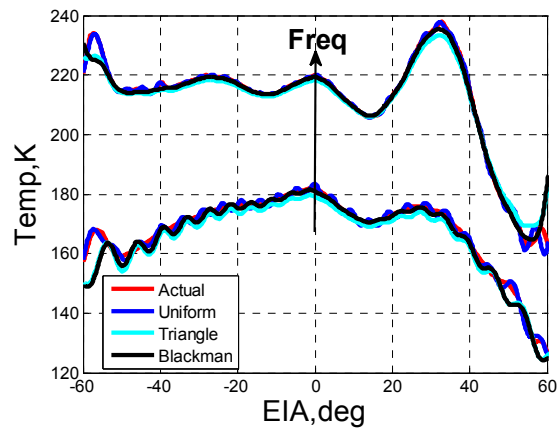
where  $I$  is the identity matrix. The regularization numbers were computed for each scan and frequency so as to minimize the difference between the original scene  $T_b$  and the estimated image,  $\hat{T}_b$ . Figure A.3 shows the  $T_b$  profiles for the different scans and at 4 and 6.6 GHz.



(a)



(b)



(c)

Figure. A.3  $T_b$  profiles at 4 and 6.6 GHz for (a) scan 1, (b) scan 2 and (c) scan 3.



These three dissimilar profiles were selected to get an indication of how sensitive imaging is to regularization, and to get an indication of the potential complexity of producing optimal images in field measurements where the actual  $T_b$  scene is unknown, and highly variable in hurricanes. The scenario used in these simulations was to consider these 3 scans to be part of a complete flight pass through the eye of hurricane Frances, which would typically include approximately 240 contiguous scans, and assume a single set of regularization numbers for use with all scans in the pass. This is equivalent to optimizing with respect to one particular  $T_b$  scene.

The general conclusions suggested from the results are that the uniform taper should provide the best estimate of brightness temperature for HIRAD and that some method of optimizing matrix regularization for image reconstruction is needed. Reconstructed brightness temperature scenes are sensitive to the value of the regularization number applied in the inversion process, and the examples presented here show significant effects on estimated  $T_b$ . But, these simulations did demonstrate that the uniform taper and optimal inversion in image reconstruction could produce images to  $\pm 2$  K.

The above studies represent the conducted research in the image reconstruction area. For the purpose of this dissertation, we are estimating the HIRAD performance exclusive of synthetic aperture radiometry image reconstruction errors since it is a dissertation topic by itself that is still under development.

## APPENDIX B. PLANAR ARRAY

Individual radiators can be positioned along a rectangular grid to form a planar array that is composed of  $M \times N$  elements according to Fig. B.1. Planar arrays provide additional variables when compared to linear arrays which can be used to control and shape the pattern of the array.

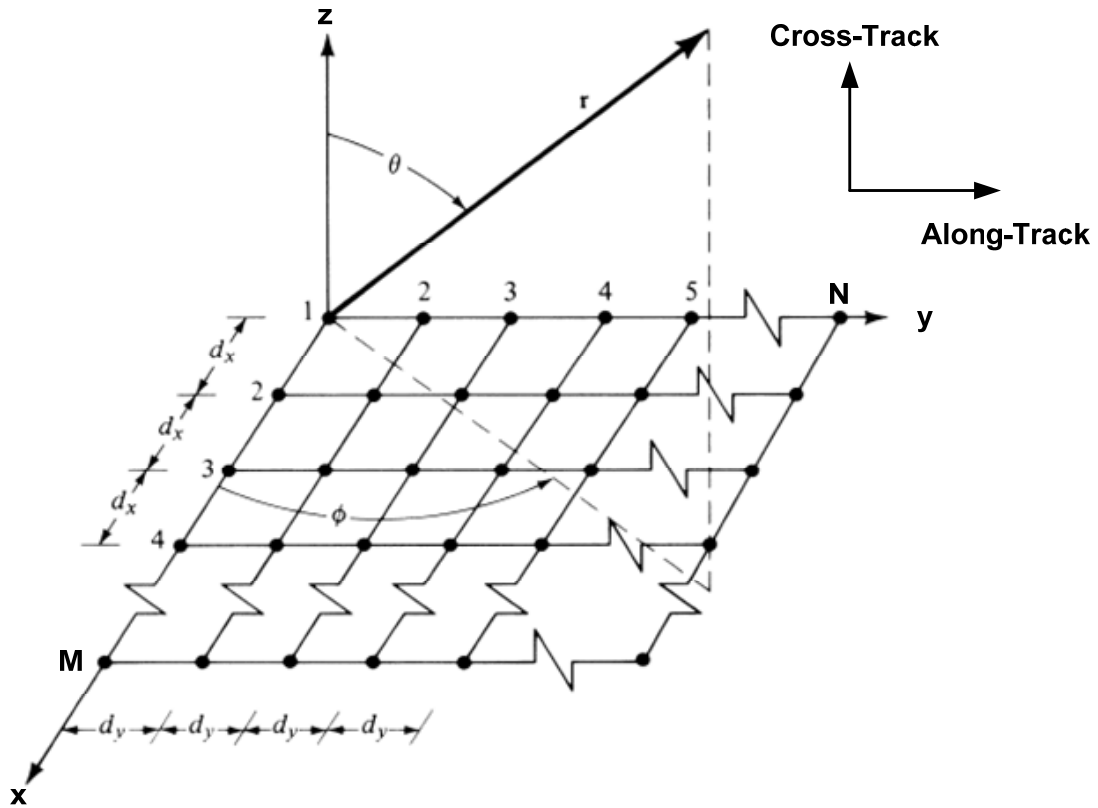


Figure. B.1 Planar array geometry

The array pattern in general is the multiplication of the array factor times the element pattern. Each array has its own array factor, AF. The array factor, in general, is a function of the number of elements, their geometrical arrangement, their relative magnitudes, their relative

phases and their spacing. By referring to Fig. B.1, the array factor for the entire planar is given by [22],

$$AF_n(\theta, \phi) = \sum_{m=0}^{M-1} e^{jm(kd_x \sin \theta \cos \phi + \beta_x)} \sum_{n=0}^{N-1} e^{jn(kd_y \sin \theta \sin \phi + \beta_y)} \quad (\text{B.1})$$

where

$M$ : is the number of cross-track elements,

$N$ : is the number of along-track elements,

$d_x, d_y$ : are the spacing between the  $M$  elements and  $N$  elements respectively,

$\beta_x, \beta_y$ : are the progressive phase shifts between the elements along the x-axis and y-axis respectively.

Since the along-track HIRAD beam is sufficiently narrow fan beam, then there is no variations in  $\phi$ , and therefore (B.1) can be simplified according to,

$$AF_n(\theta, \phi) = \sum_{m=0}^{M-1} e^{jm(kd_x \sin \theta \cos \phi + \beta_x)} \quad (\text{B.2})$$

The progressive phase shift,  $\psi_x$ , is represented by,

$$\psi_x = kd_x \sin \theta \cos \phi + \beta_x \quad (\text{B.3})$$

And  $K$  is given by,

$$K = 2\pi/\lambda \quad (\text{B.4})$$

Each of the four different C-band frequencies has an independent antenna design in terms of the number of cross-track elements,  $M$ , which are given by Table B.1, whereas the spacing between these elements is constant for all four frequencies and is equal to  $0.4 \times \lambda$ . When the spacing between elements is equal or greater than  $\lambda/2$ , multiple maxima of equal magnitudes can be formed. The principle maximum is referred to as the major lobe and the remaining as the grating lobes. A grating lobe is defined as a lobe other than the main lobe, produced by an array antenna when the inner element spacing is sufficiently large to permit the in-phase addition of radiated fields in more than one direction. To avoid grating lobes in the  $x$ - $z$  plane, the spacing between the elements in the  $x$ -direction was made less than  $\lambda/2$ .

**Table. B.1 Number of cross-track elements at each frequency**

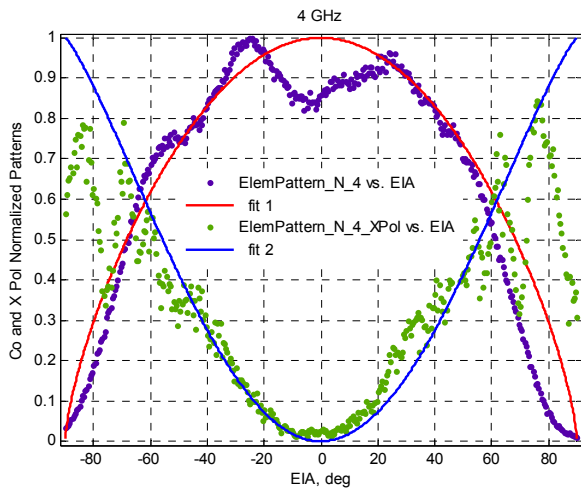
<b>Frequency, GHz</b>	<b>M</b>
4	61
5	72
6	73
6.6	71

The other part of the array pattern is the element pattern,  $EP$ , which serves as an envelope on the AF. The Co-pol element pattern is different than that for the X-pol and those are given by (B.5) and (B.6) respectively,

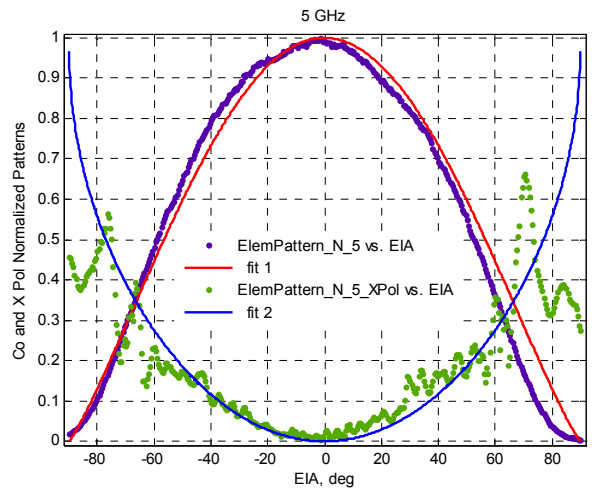
$$EP_m(\theta) = \cos(\theta)^m \quad (\text{B.5})$$

$$EP_n(\theta) = 1 - \cos(\theta)^n \quad (\text{B.6})$$

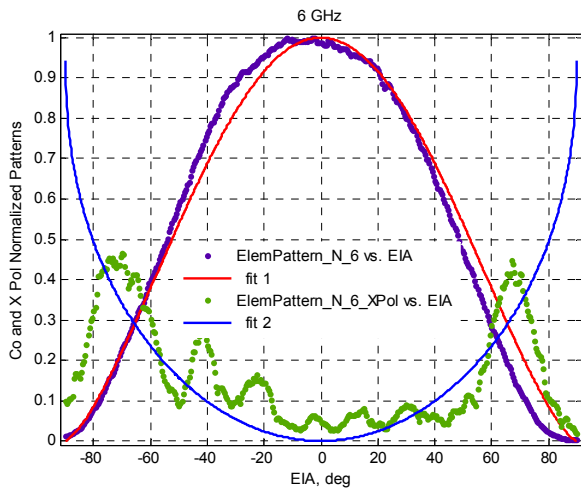
where  $m$  and  $n$  are based on the best curve fits, as shown in Fig. B.2, for the composite element patterns measured as part of the October chamber tests in Huntsville, Alabama (2008) for the HIRAD array. Table B.2 summarizes these numbers.



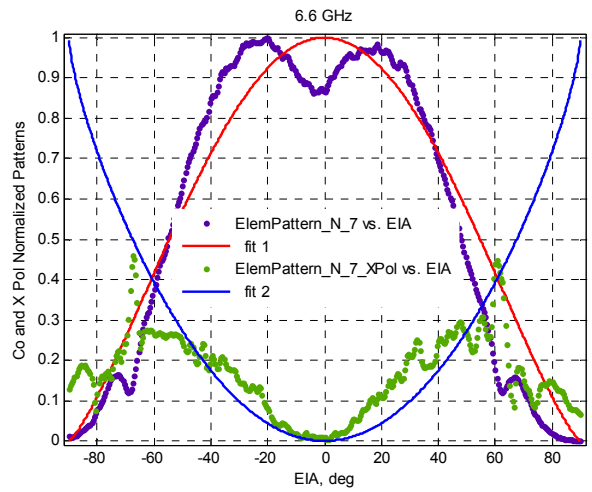
(a)



(b)



(c)



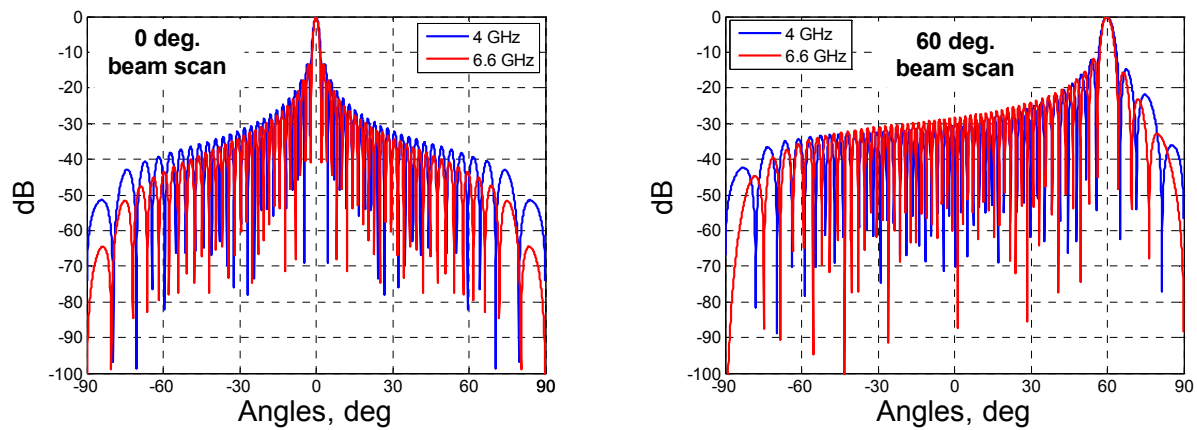
(d)

**Figure. B.2 Co-Pol and X-Pol composite element patterns at (a) 4 GHz, (b) 5 GHz, (c) 6 GHz and (d) 6.6 GHz.**

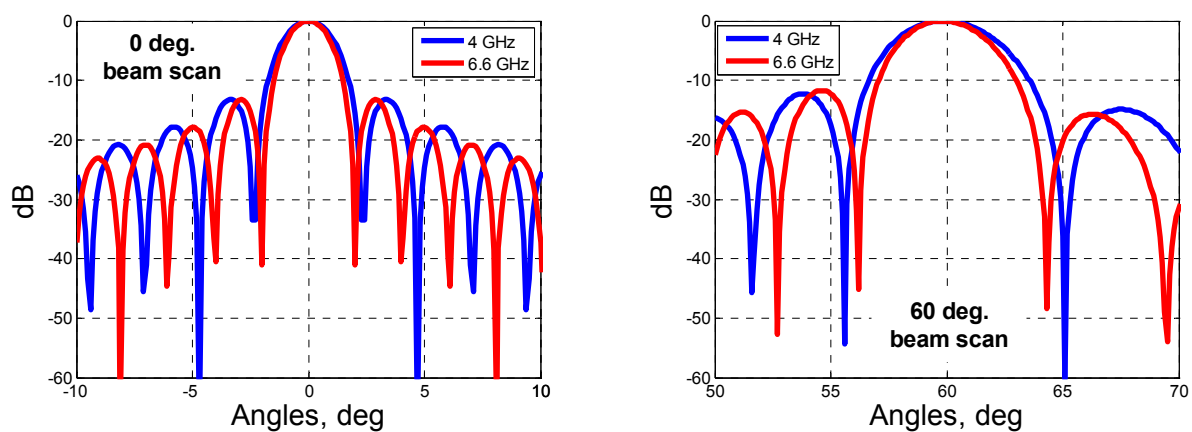
**Table. B.2 m and n values at each frequency**

<b>Frequency, GHz</b>	<b>m Co-Pol</b>	<b>n X-Pol</b>
4	0.695	1.205
5	1.165	0.465
6	1.401	0.388
6.6	1.265	0.720

The Co- and X-Pol patterns were computed based on the design described in the previous section. Figure B.3 and B.4 (a) shows the Co-Pol and X-Pol patterns respectively for the lowest and highest frequencies at 0 deg and 60 deg boresight angles and (b) a zoomed portion of the patterns to show the main beam and the first couple sidelobes.



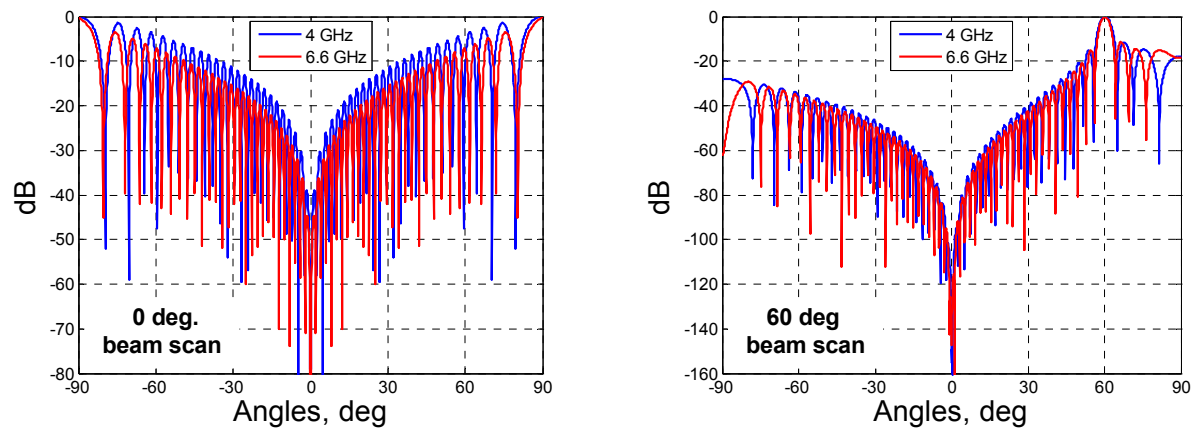
(a)



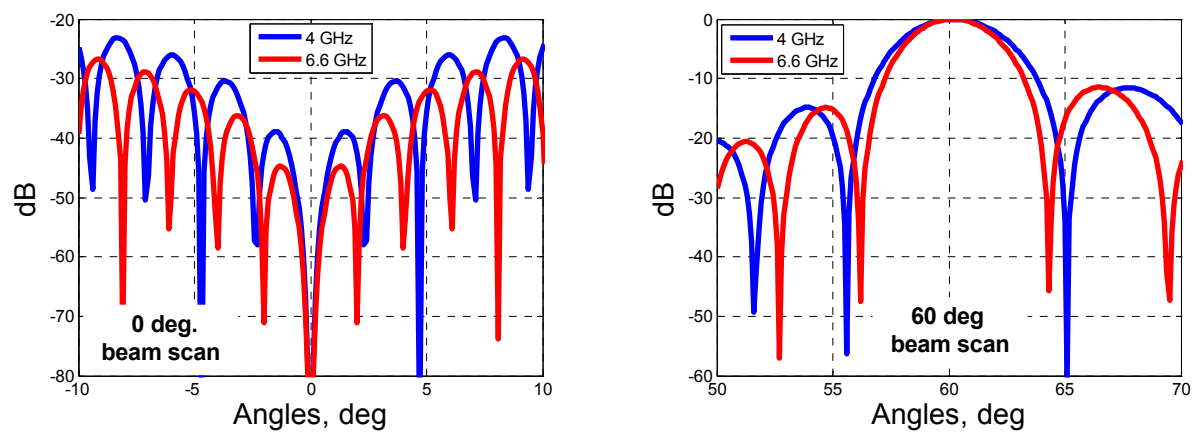
(b)

Figure. B.3 Co-Pol patterns at 4 and 6.6 GHz frequencies for (a) 0 deg and 60 deg scan beams and (b) zoomed portion of the main beam.





(a)



(b)

Figure. B.4 X-Pol patterns at 4 and 6.6 GHz frequencies for (a) 0 deg and 60 deg scan beams and (b) zoomed portion of the main beam.

As noticed from Fig. B.3 and B.4 (b), the pattern beamwidth decreases with frequency for all beam positions. The beam efficiency was computed for these patterns according to [22],

$$\eta = \frac{\int_0^{2\pi} \int_{-\theta_1}^{\theta_1} F(\theta, \phi) \times \sin \theta d\theta d\phi}{\int_0^{2\pi} \int_{-\pi/2}^{\pi/2} F(\theta, \phi) \times \sin \theta d\theta d\phi} \quad (\text{B.7})$$

where  $\theta_1$  is chosen as the angle where the first nulls occur. The beam efficiency indicates the amount of power in the major lobe compared to the total power. Table B.3 shows the first side lobe level, SLL, the 3dB and the null-to-null beamwidths along with the beam efficiency values for all four frequencies for a 0 deg and a 60 deg Co-Pol beam scan patterns.

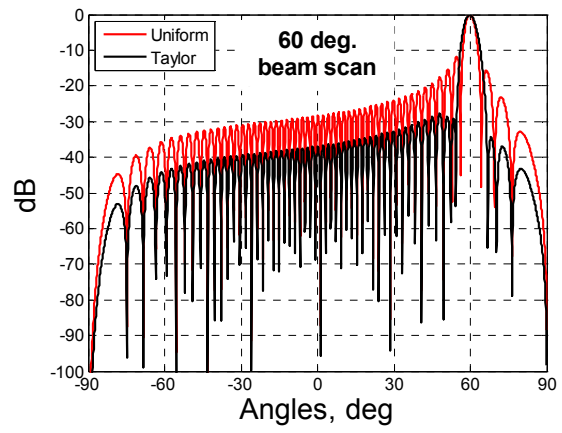
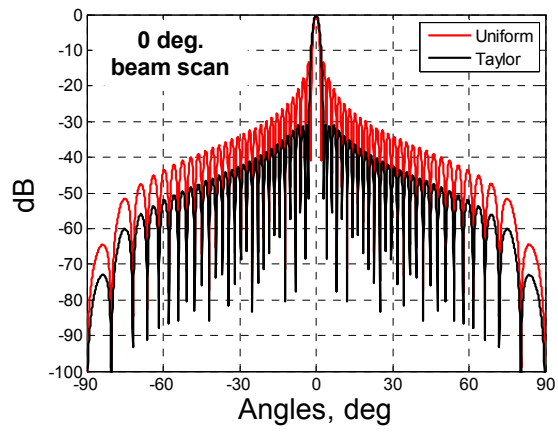
**Table. B.3 Co-Pol 0 deg and 60 deg beam scan patterns' characteristics**

	<b>Frequency, GHz</b>	<b>First SLL, dB</b>	<b>3dB BW, deg</b>	<b>Null BW, deg</b>	<b>Beam Efficiency, %</b>
<b>0 deg Boresight</b>	4	-13.29	4.5	10.4	50.64
	5	-13.3	3.7	8.2	50.34
	6	-13.28	2.9	6.8	48.75
	6.6	-13.28	2.7	6.2	46.87
<b>60 deg Boresight</b>	4	-11.48	8.9	22.1	63.16
	5	-10.76	6.9	17	48.11
	6	-10.65	5.8	13.8	36.97
	6.6	-11.03	5.4	12.6	34.37

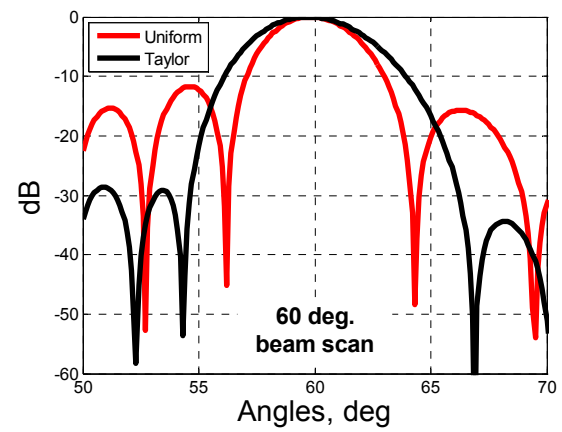
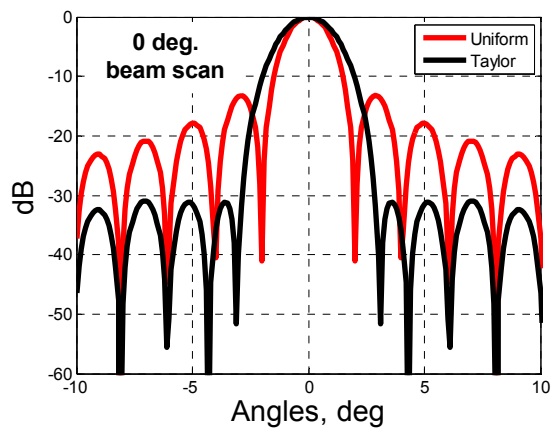
High beam efficiency (between the nulls) usually in the mid 90s is necessary for antennas used in radiometry. Therefore, the beam efficiencies provided in Table B.3 were increased as part of the antenna design by applying a Taylor taper with SLL of -31dB to the array factor according to,

$$AF_n(\theta, \phi) = \sum_{m=0}^{M-1} w \times e^{jm(kd_x \sin \theta \cos \phi + \beta_x)} \quad (\text{B.8})$$

Figures B.5 and B.6 shows the uniform and tapered Co-Pol and X-Pol patterns respectively for 6.6 GHz for a 0 deg and a 60 deg beam scans. As noticed from the figure, applying the Taylor taper decreased the first SLL to around -31dB and widened the beamwidths.

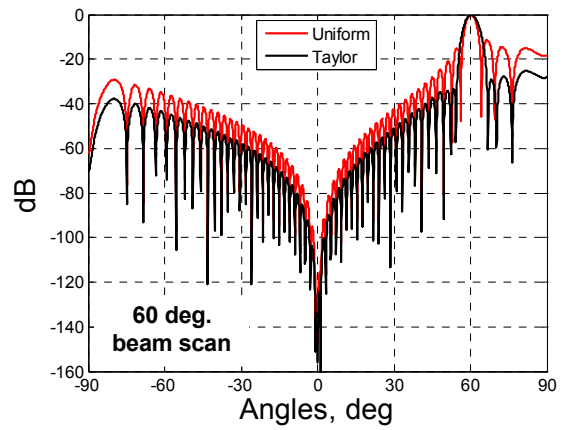
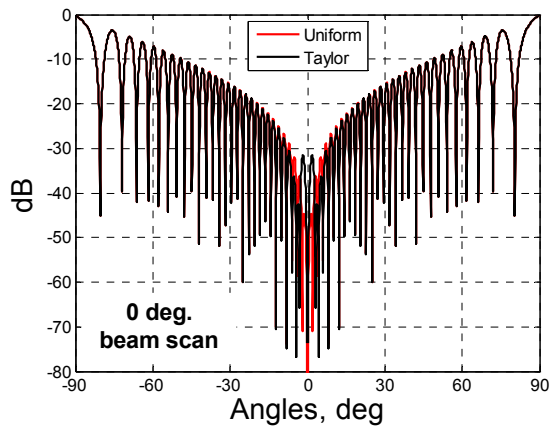


(a)

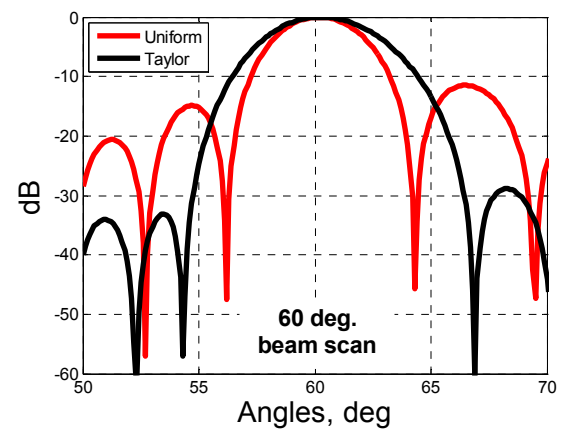
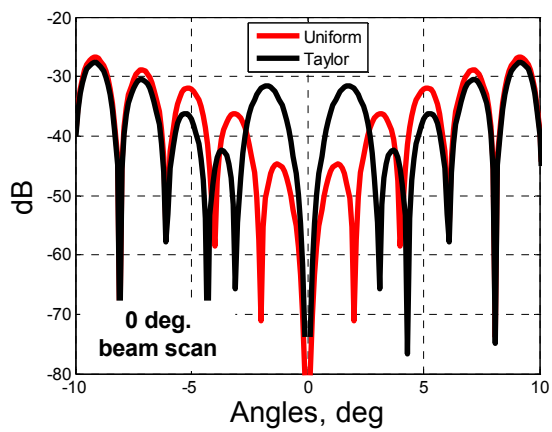


(b)

Figure. B.5 Co-Pol uniform and tapered patterns at 6.6 GHz frequency for (a) 0 deg and 60 deg scan beams and (b) zoomed portion of the main beam.



(a)

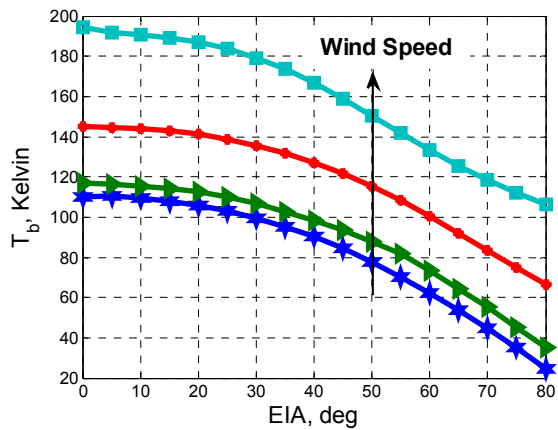


(b)

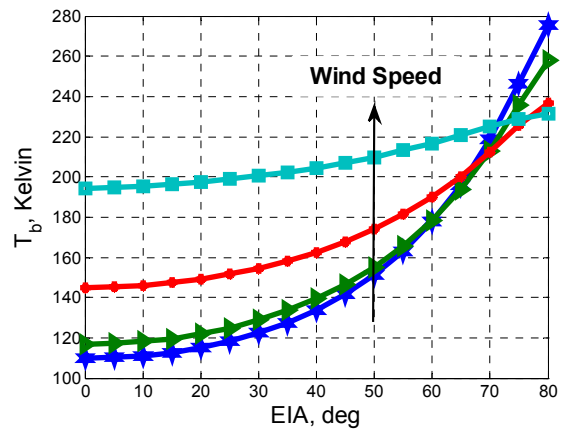
Figure. B.6 X-Pol uniform and tapered patterns at 6.6 GHz frequency for (a) 0 deg and 60 deg scan beams and (b) zoomed portion of the main beam.

## APPENDIX C. CFRSL EMISSIVITY MODEL FIGURES

Figure C.1 shows the CFRSL emissivity model [10] with respect to incidence angle at all C-band frequencies scaled for a SST = 300 Kelvin for horizontal and vertical polarization and wind speeds of 6, 20, 40 and 70 m/s.

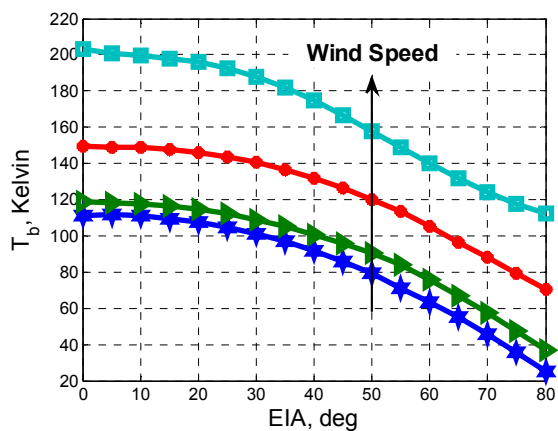


(a)

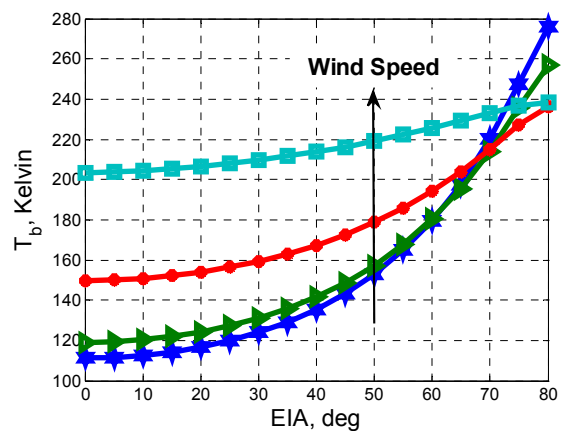


(b)

4.0 GHz

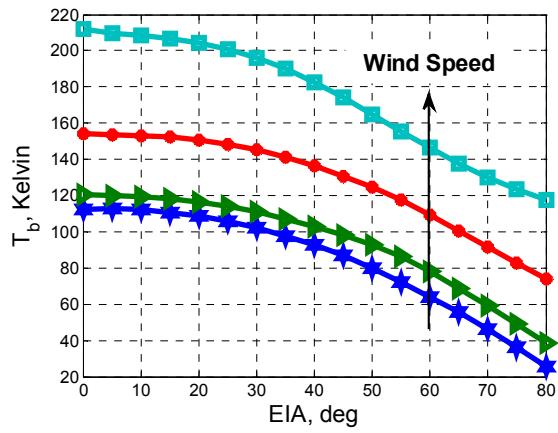


(a)

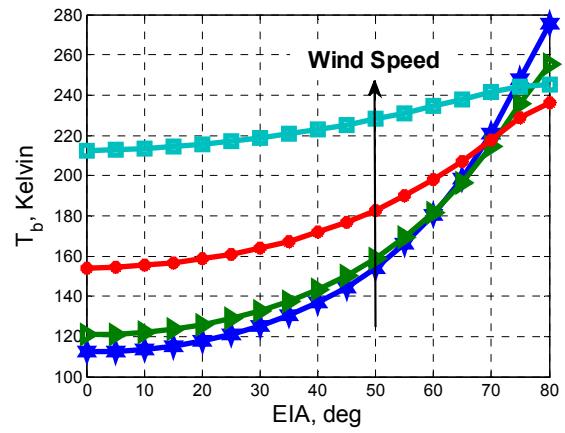


(b)

5.0 GHz

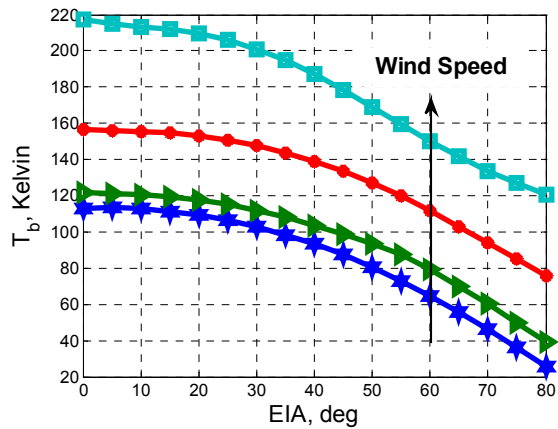


(a)

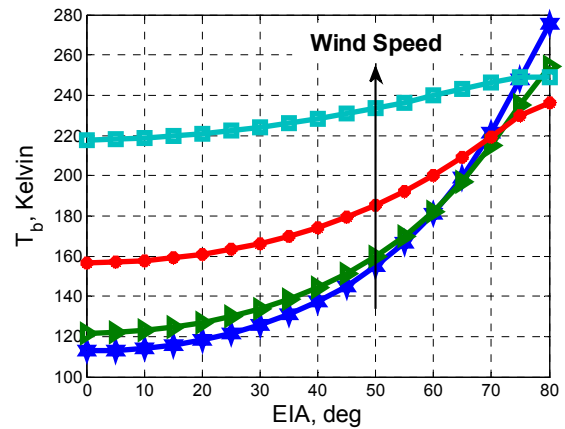


(b)

6.0 GHz



(a)



(b)

6.6 GHz

Figure. C.1 The CFRSL ocean surface emissivity model for SST = 300 Kelvin: (a) horizontal and (b) vertical polarization at all frequencies and wind speeds of 6, 20, 40 and 70 m/s from El-Nimri et al., 2010.

## **APPENDIX D.        RADTB MICROWAVE RADIATIVE TRANSFER MODEL**

The RTM is implemented in two parts as illustrated by the block diagram shown in Fig. D.1. The first part is coded in FORTRAN (RadTb) and the second part is implemented in MATLAB. This appendix describes RadTb, which is used at the Central Florida Remote Sensing Laboratory. This model was derived from the EnvaMod RTM [23] that was developed by the US Naval Research Laboratory during the 1970's. RadTb's FORTRAN program consists of a main program and subroutines that will be discussed in this appendix.

RadTb uses 39 layers of 20 km total thickness to describe the layered atmosphere with the thickness of the layers increasing as a function of altitude.



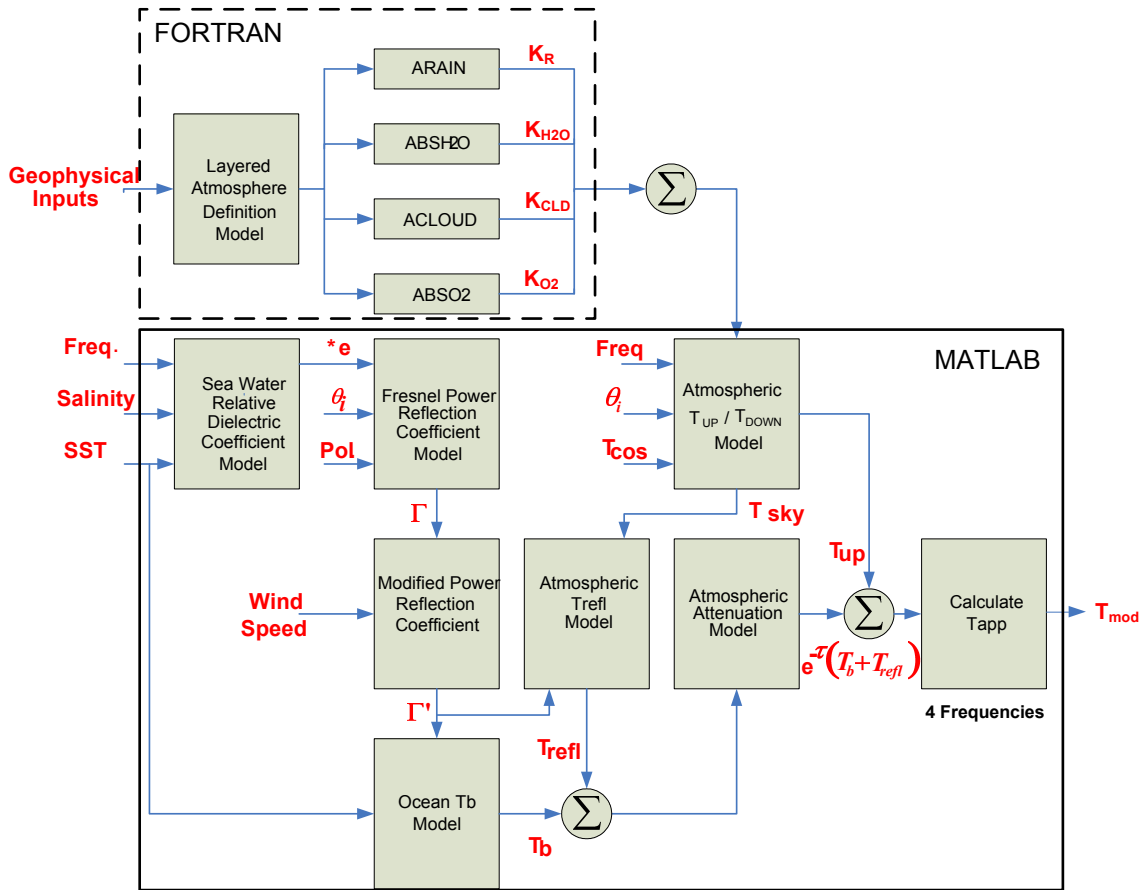


Figure. D.1 HIRAD radiative transfer model.

The ABSH2O subroutine shown in Fig. D.1 calculates the absorption coefficient of water vapor (Np/km), from the provided water vapor mass densities, in the air by means of Gross's formula [24] from frequencies below 400 GHz. It approximates the contribution from high frequency vapor lines at the lower frequency from the line shape function. The input parameters to ABSH2O are:

- L – level number
- P – total pressure at L (mb)

T – temperature at L (K)

AH – absolute humidity at L ( $\text{g/m}^3$ )

FREQ – frequency (GHz)

The output parameter is the absorption coefficient at L ( $\text{Np/km}$ ),  $K_{\text{H}_2\text{O}}$ .

The ACLOUD subroutine calculates the cloud absorption coefficient ( $\text{Np/km}$ ) at level L from the cloud mass densities provided by the hurricane model. The input parameters are:

L – level number

T – temperature at L (K)

MC – liquid water density at L ( $\text{g/m}^3$ )

FREQ – frequency (GHz)

The output parameter is the absorption coefficient at L ( $\text{Np/km}$ ),  $K_{\text{CLD}}$ .

ABSO2 subroutine calculates molecular oxygen absorption at level L. The results of ROSENKRANZ (1975) are used. The input parameters are:

L – level number

P – total pressure at L (mb)

T – temperature at L (K)

FREQ – frequency (GHz)

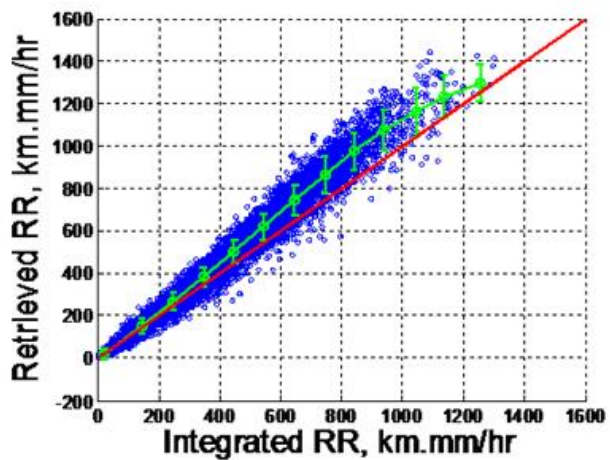
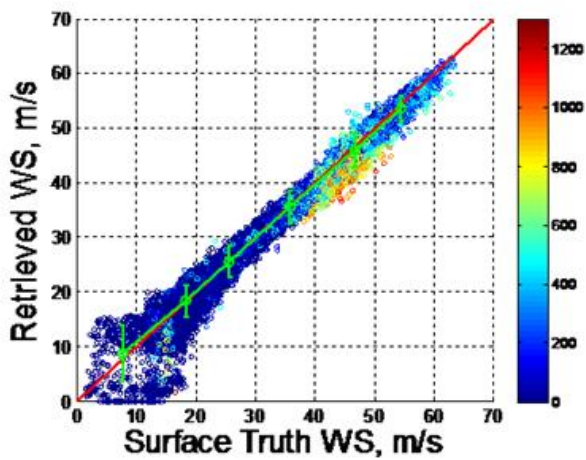
The output parameter is the oxygen absorption coefficient at L ( $\text{Np/km}$ ),  $K_{\text{O}_2}$ .

These absorption coefficients are summed with the rain absorption coefficient,  $K_{\text{R}}$ , described earlier in Chapter 3, in MATLAB and are then used in the computation of the apparent brightness temperatures.

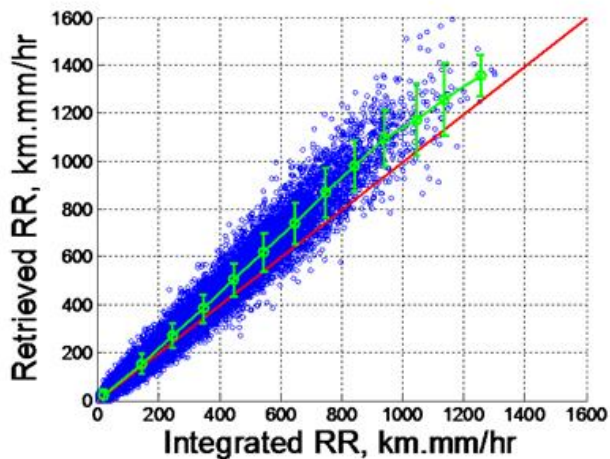
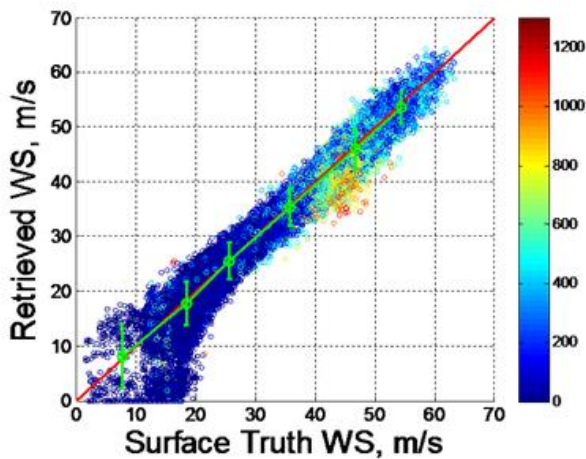
## **APPENDIX E. RESULTS**

This appendix presents the remaining results that were covered in Chapter 5 but for all random errors (1, 2, 4 and 8 Kelvin). Similar conclusions were drawn from these results as discussed earlier.

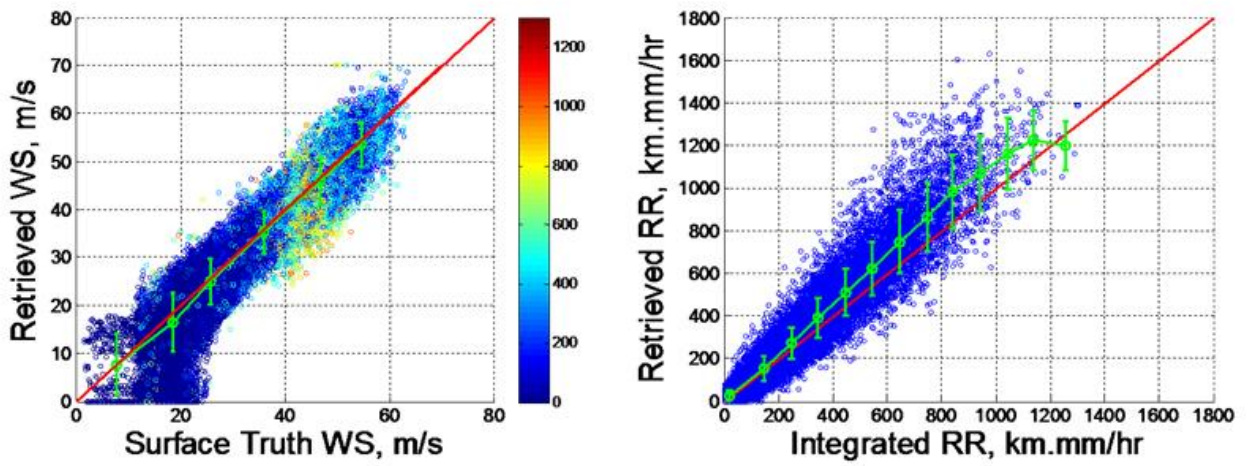
A comparison between the nature run and retrieved wind speed and rain rate is presented in Fig. E.1 for the 8 Frances legs (3 Fig-4 and two outside the eye legs) and for random errors of 1, 2, 4 and 8 Kelvin. The color-bar refers to the integrated rain rate values in km-mm/hr.



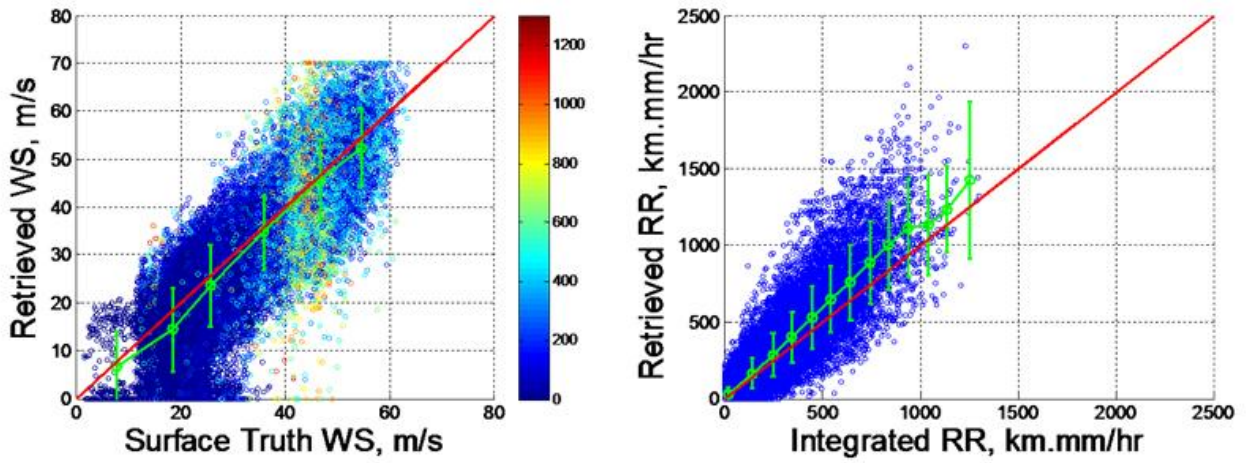
(a)



(b)



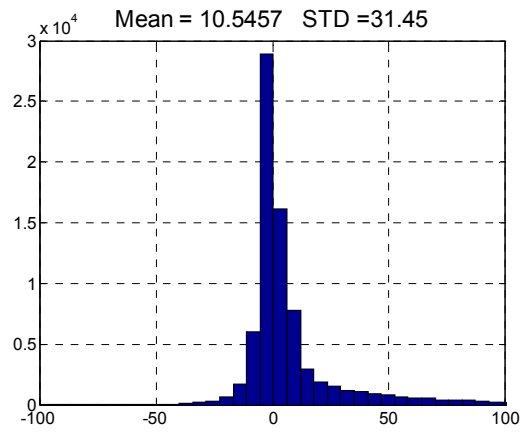
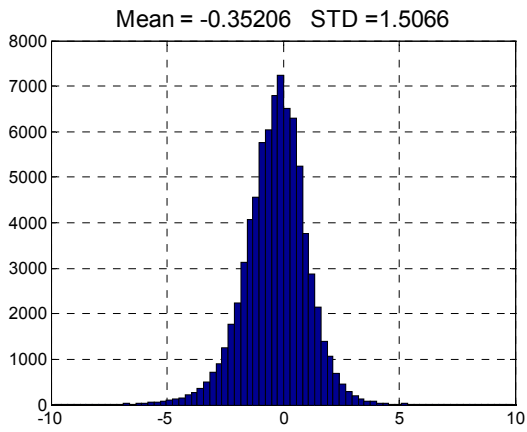
(c)



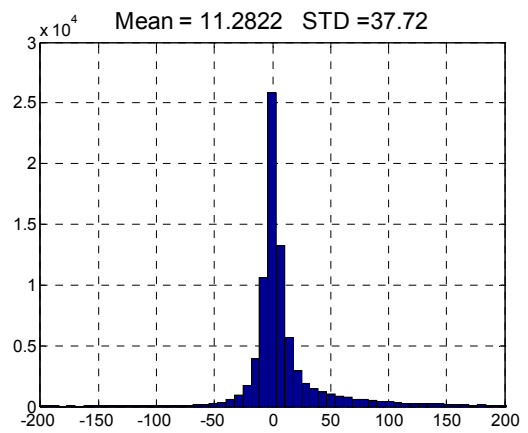
(d)

Figure. E.1 Scatter plot comparisons for wind speed (left panel) and rain rate (right panel) for random error (a) 1 Kelvin, (b) 2 Kelvin, (c) 4 Kelvin and (d) 8 Kelvin.

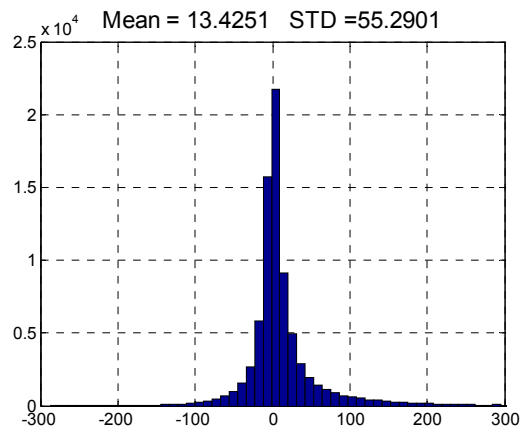
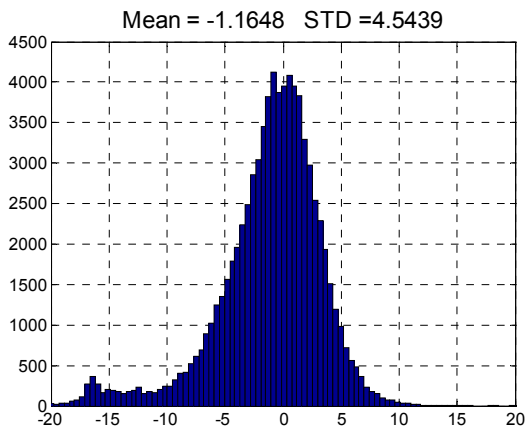
As noticed, scattering about the mean wind speed and rain rate values increases with random error. Also, there is a good correlation between the nature run and the retrieved wind speed values except at relatively lower wind speed due to the nature of the model function, which makes the random error effects more dominant at lower wind speeds. The retrieved rain rate, on the other hand, is over estimated at higher rain rate values, which is correlated with longer slant paths (edges of swath) due to the difference in the rain rate treatment between the forward and reversed models. The associated histograms of differences between retrievals and nature runs are presented in Fig. E.2 for all random error values. As expected both the mean and STD values of the differences in wind speed and rain rate increase with random error.



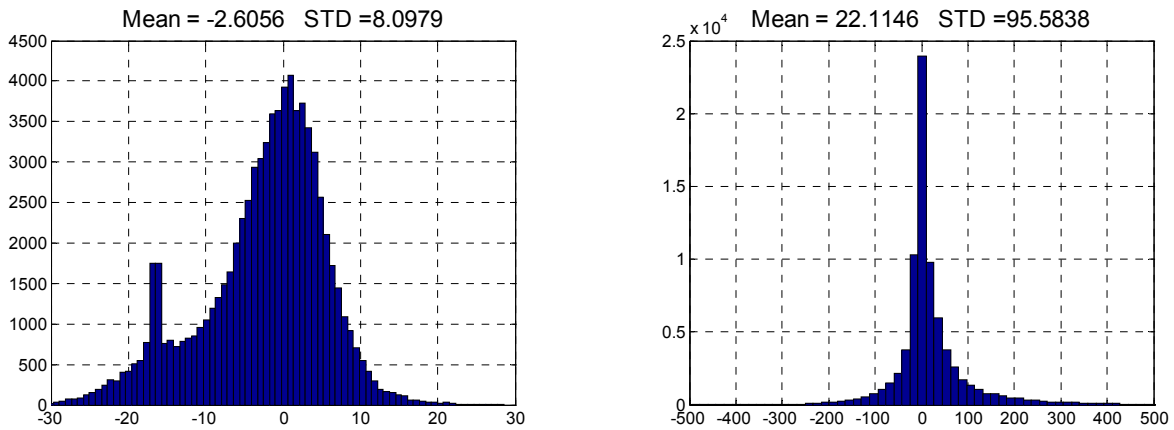
(a)



(b)



(c)

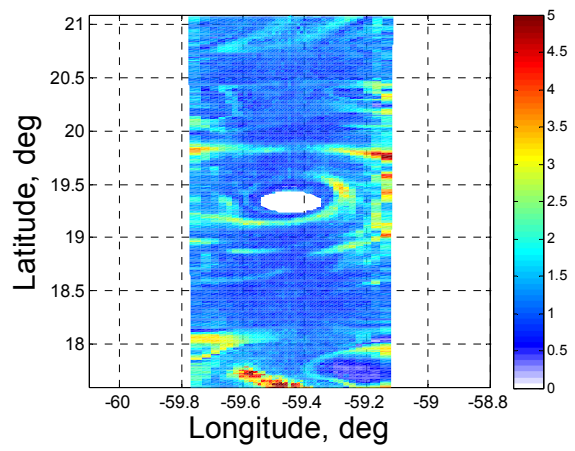
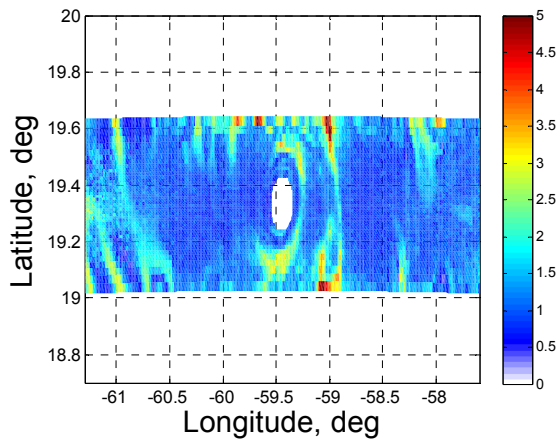


(d)

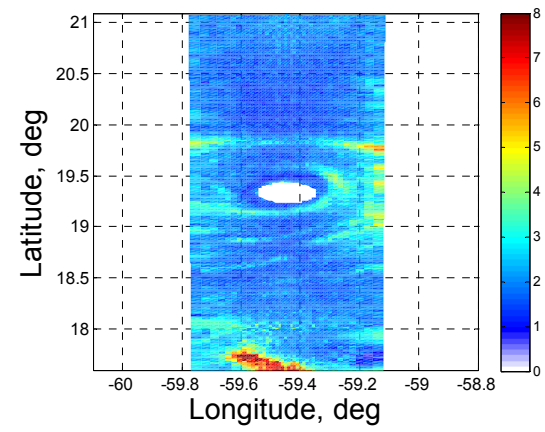
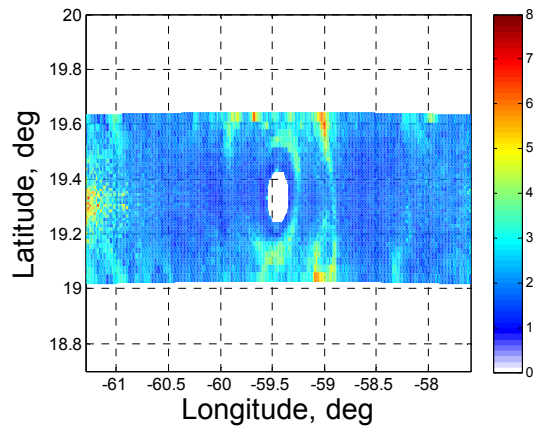
**Figure. E.2 Histograms of the differences in wind speed (left panel) and rain rate (right panel) for random error (a) 1 Kelvin, (b) 2 Kelvin, (c) 4 Kelvin and (d) 8 Kelvin.**

Retrieved wind speed is compared to the nature run “surface truth” wind field, and the RMS differences (for the 1, 2, 4 and 8 Kelvin random error case) are plotted for both orthogonal legs (regular Fig-4 IP 90) in Fig. E.3. As noticed, as the random error increases, the RMS wind speed errors increase everywhere across the swath uniformly except at lower wind speed values where the random error effect is maximum.

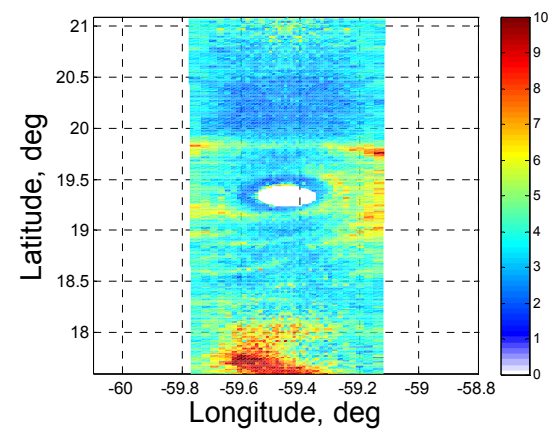
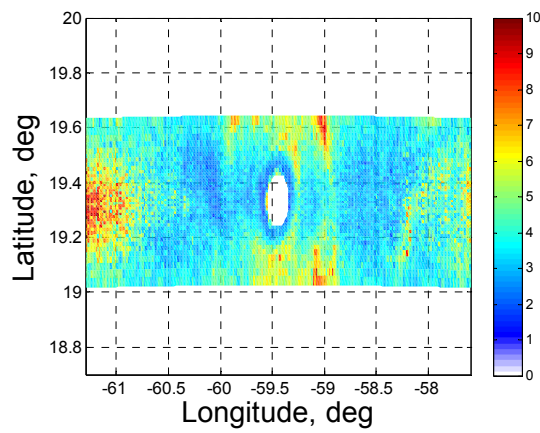




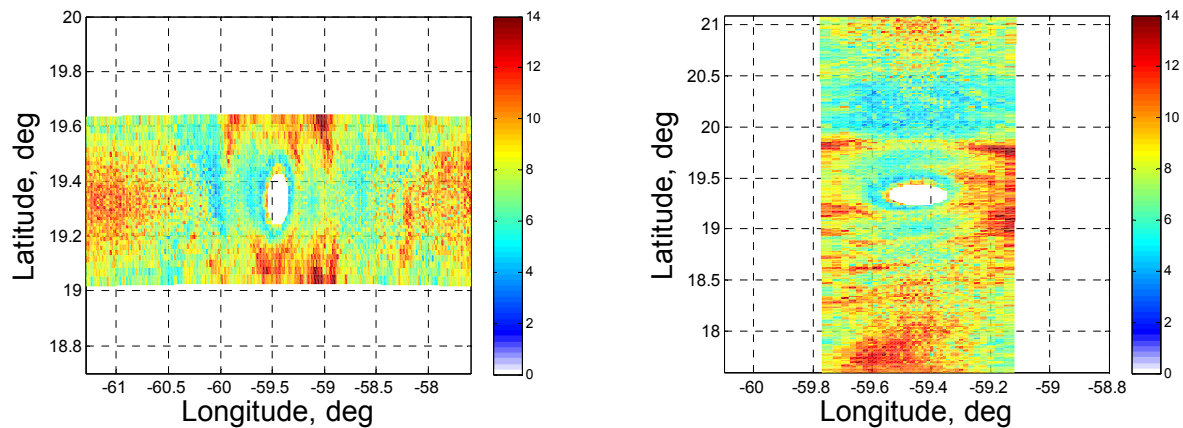
(a)



(b)



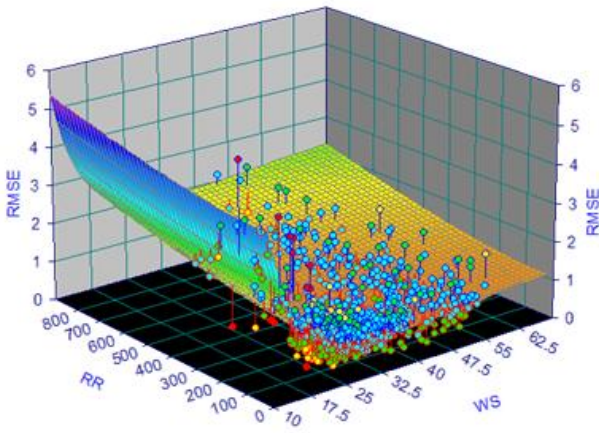
(c)



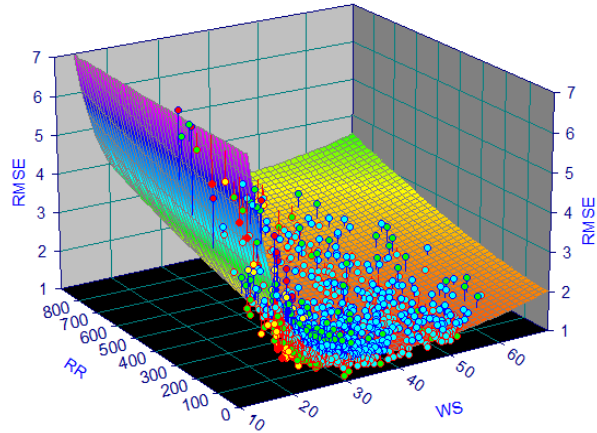
(d)

**Figure. E.3** RMS retrieved wind speed errors for Leg 1 (left panel) and Leg 2 (right panel) for random error (a) 1 Kelvin, (b) 2 Kelvin, (c) 4 Kelvin and (d) 8 Kelvin.

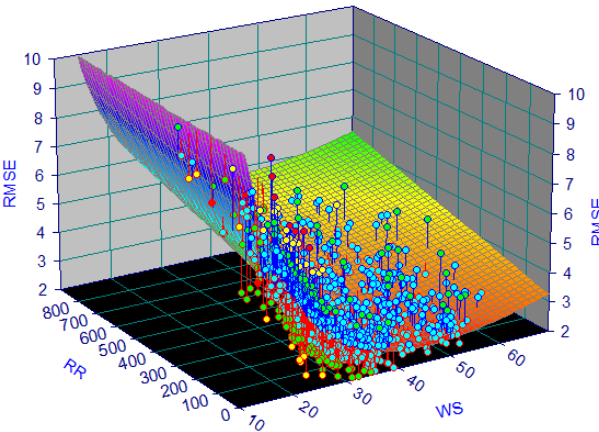
The best wind speed RMSE surface fits were computed for all random errors and at three different beam positions. Figure E.4 shows the best surface fits to the RMSE wind speed values at Nadir for all random error values. As noticed from these surfaces, at lower wind speed values, RMS wind speed errors are the greatest due to the random error effects that is dominant at lower wind speeds. Also noticed is the increase in the error as wind speed and rain rate increase. Increasing the random error results in increased wind speed RMS error as expected.



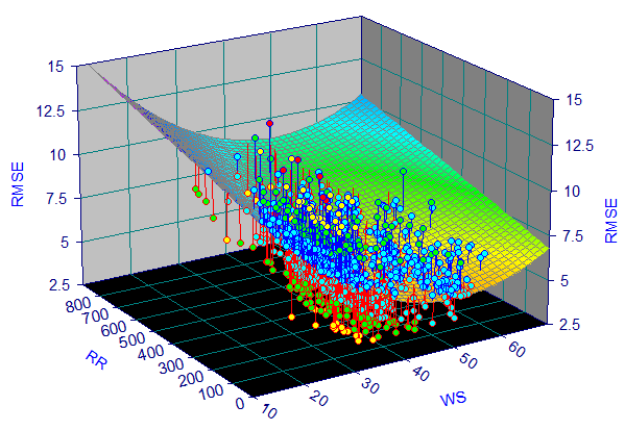
(a) 1 Kelvin



(b) 2 Kelvin



(c) 4 Kelvin

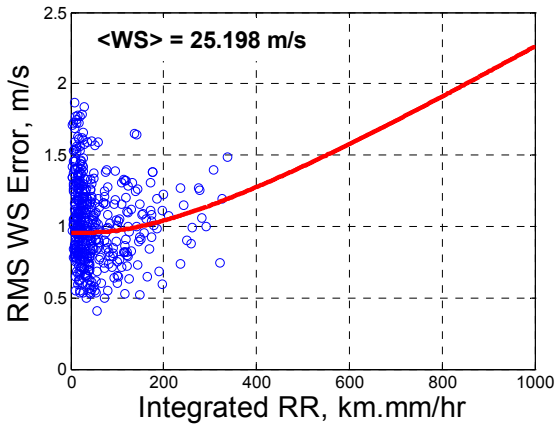


(d) 8 Kelvin

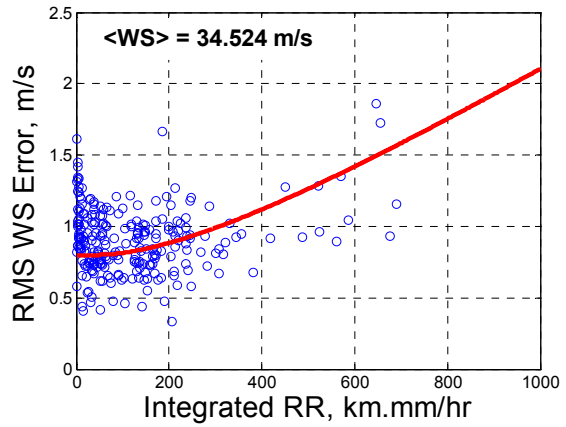
**Figure. E.4 RMS retrieved wind speed error surfaces at Nadir for random error (a) 1 Kelvin, (b) 2 Kelvin, (c) 4 Kelvin and (d) 8 Kelvin.**

The RMS wind speed errors were plotted for the Nadir beam positions as a function of integrated rain rates for  $\pm 5$  m/s wind speed bins for random errors 1, 2, 4 and 8 Kelvin as shown in Fig. E.5, Fig. E.6, Fig. E.7 and Fig. E.8 respectively, with the red lines indicating the best surface fits to the points. At Nadir, there is no X-Pol effect and the majority of the RMS wind speed errors are due to the vertical variation in rain rate and the atmosphere. As for SST contribution, its

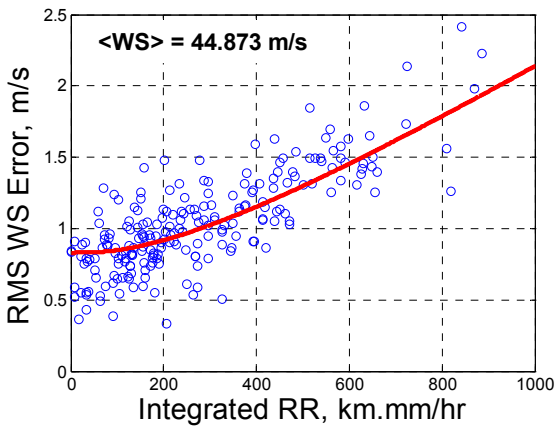
effect decreases at higher wind speed values. Increasing the random error results in increased wind speed RMS error as expected.



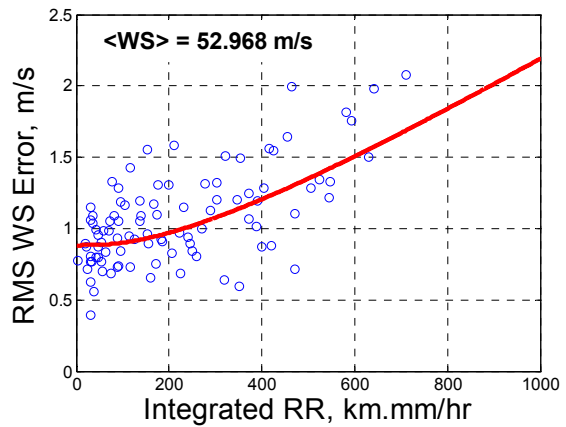
(a)



(b)

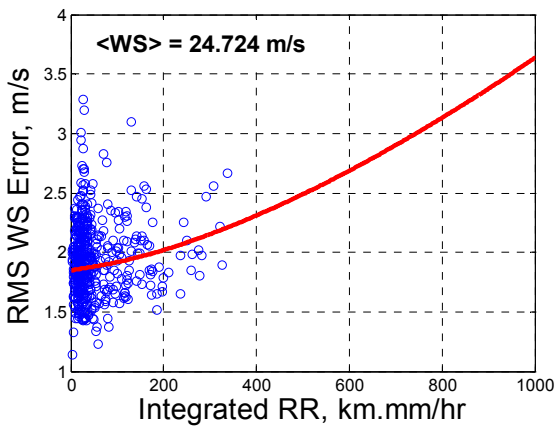


(c)

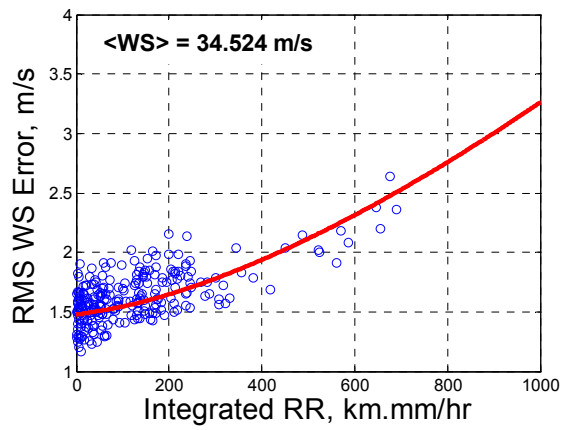


(d)

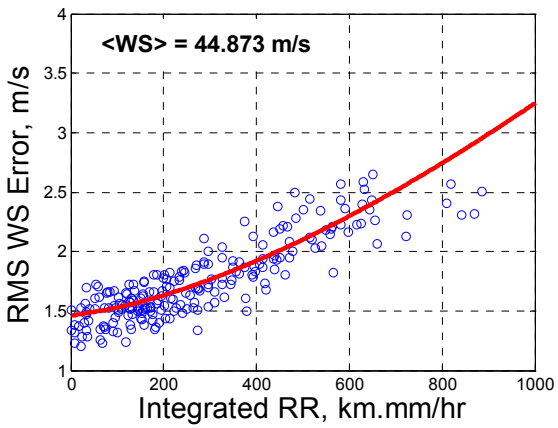
Figure. E.5 RMS wind speed errors (m/s) at Nadir for four wind speed bins  $\pm 5$  m/s for 1 Kelvin random error.



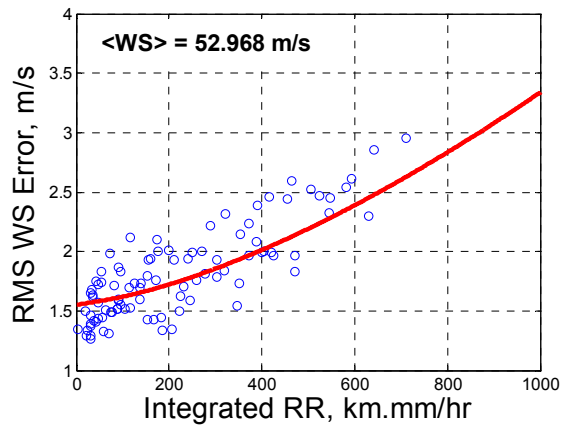
(a)



(b)

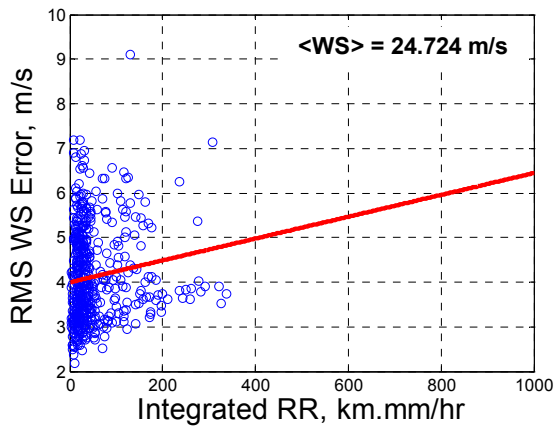


(c)

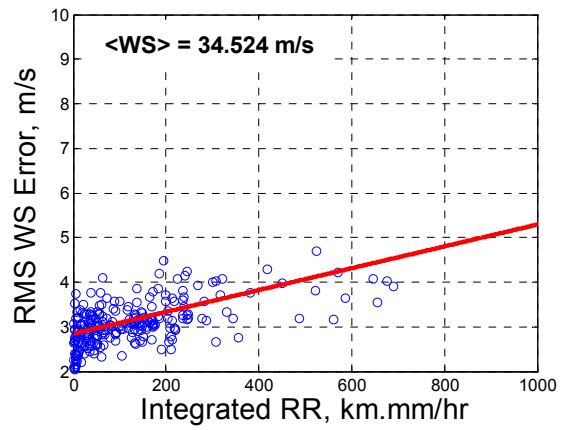


(d)

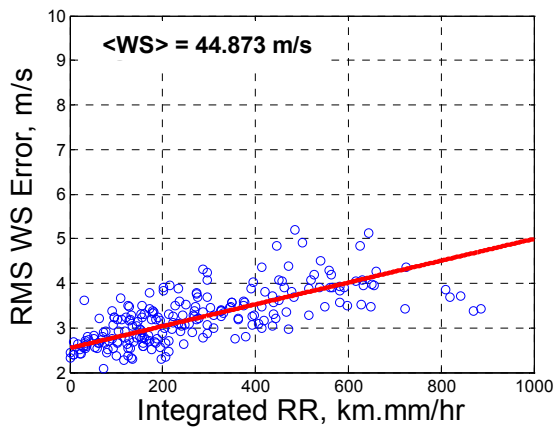
Figure. E.6 RMS wind speed errors (m/s) at Nadir for four wind speed bins  $\pm 5$  m/s for 2 Kelvin random error.



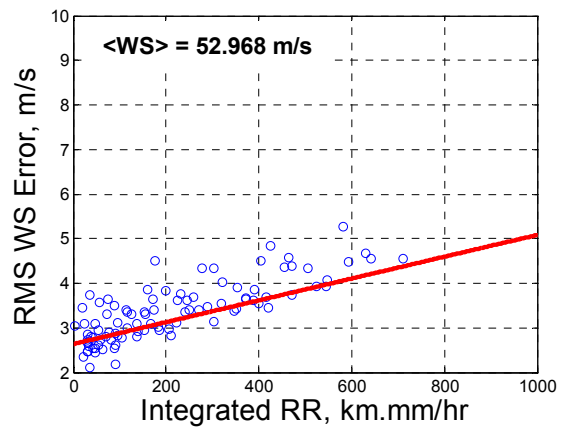
(a)



(b)

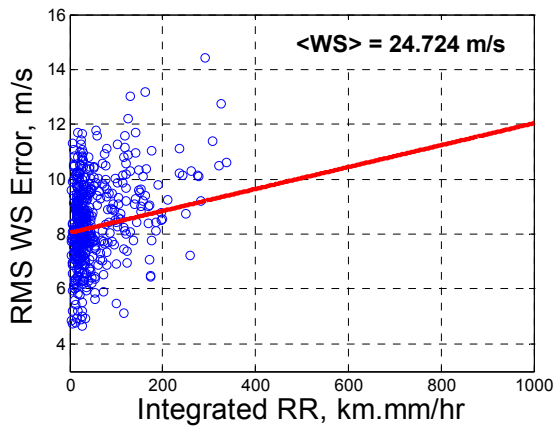


(c)

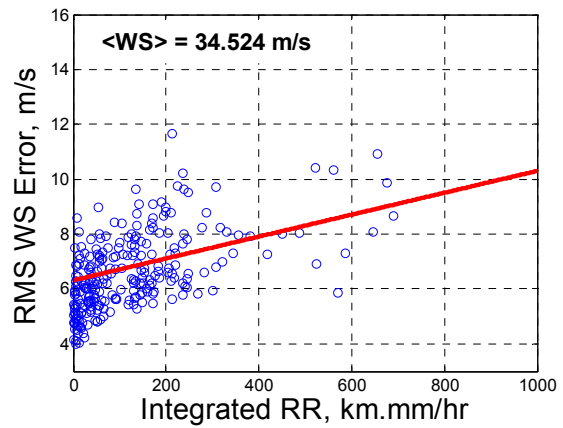


(d)

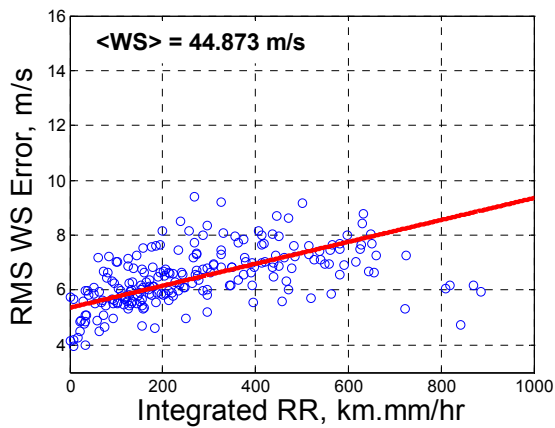
Figure. E.7 RMS wind speed errors (m/s) at Nadir for four wind speed bins  $\pm 5$  m/s for 4 Kelvin random error.



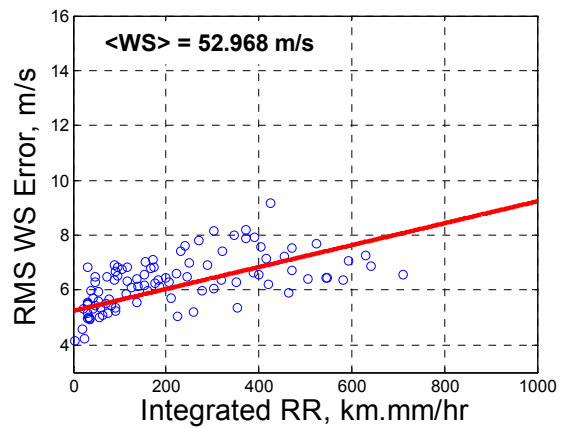
(a)



(b)



(c)



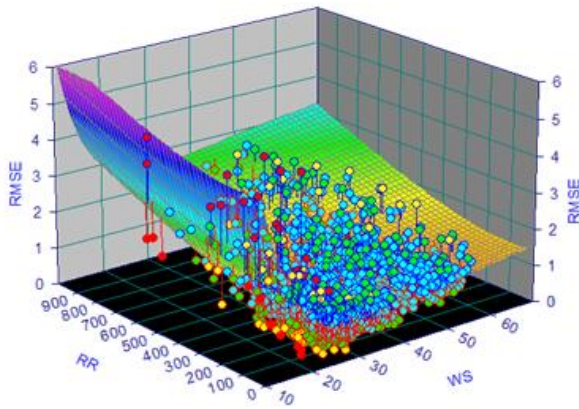
(d)

**Figure. E.8 RMS wind speed errors (m/s) at Nadir for four wind speed bins  $\pm 5$  m/s for 8 Kelvin random error.**

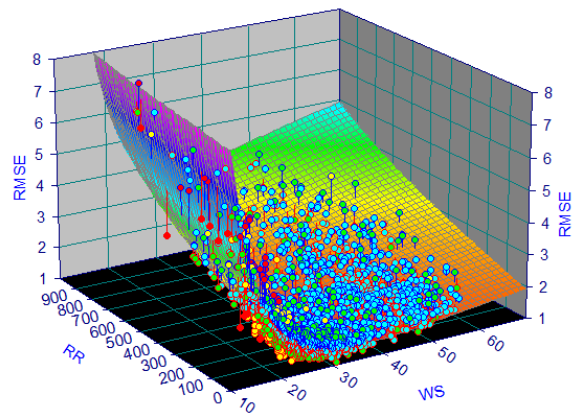
Figure E.9 shows the best surface fits to the RMSE wind speed values at  $\pm 30$  deg beam position for all random error values. Similar conclusions can be drawn in this case while noticing that RMS wind speed errors increase as EIA increases. The RMS wind speed errors also increase with integrated rain rate and with wind speeds larger than about 30 m/s. At lower wind speed

values, RMS wind speed errors are the greatest due to the random error effects that is dominant.

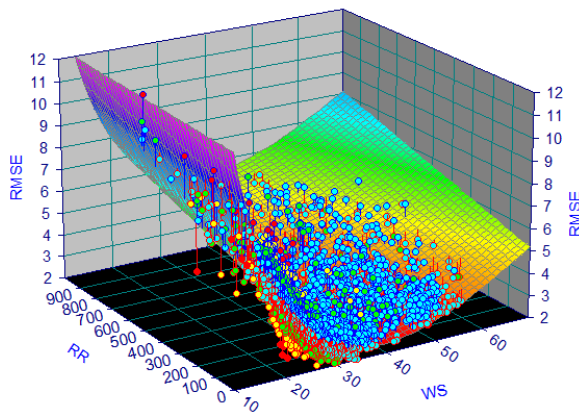
Increasing the random error results in increased wind speed RMS error as expected.



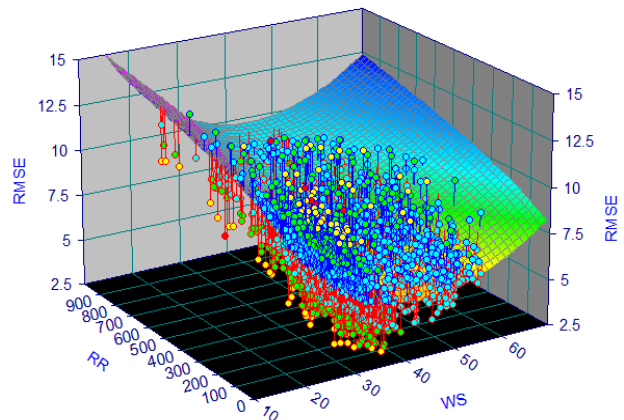
(a) 1 Kelvin



(b) 2 Kelvin



(c) 4 Kelvin

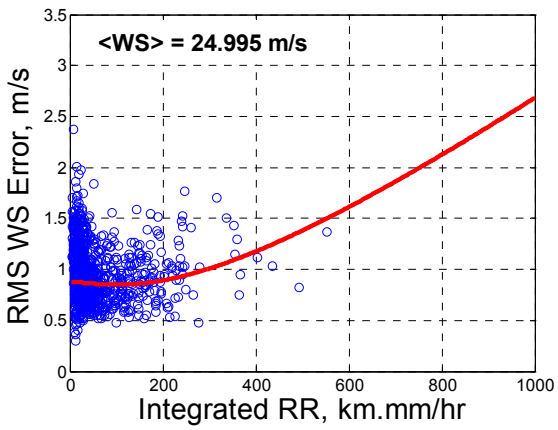


(d) 8 Kelvin

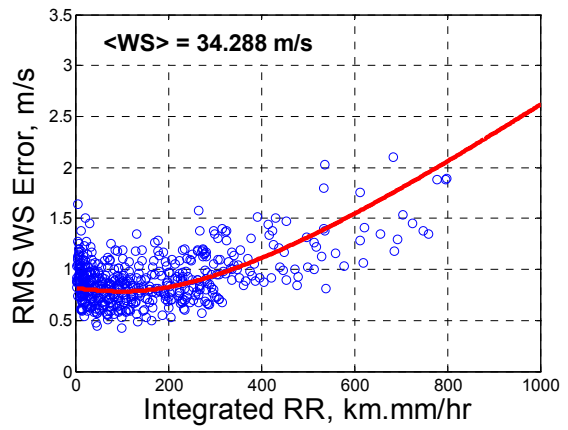
**Figure. E.9 RMS retrieved wind speed error surfaces at  $\pm 30$  deg for random error (a) 1 Kelvin, (b) 2 Kelvin, (c) 4 Kelvin and (d) 8 Kelvin.**



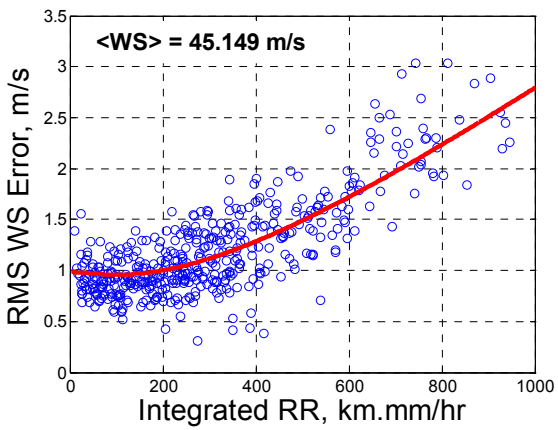
The RMS wind speed errors were plotted for the  $\pm 30$  deg beam positions as a function of integrated rain rates for  $\pm 5$  m/s wind speed bins for random errors 1, 2, 4 and 8 Kelvin as shown in Fig. E.10, Fig. E.11, Fig. E.12 and Fig. E.13 respectively, with the red lines indicating the best surface fits to the points. Again, similar conclusions regarding the behavior of the RMS wind speed errors can be observed at  $\pm 30$  deg, where the majority of the RMS wind speed errors are due to the rain rate variations, the atmosphere and the SST contribution. Increasing the random error results in increased wind speed RMS error as expected and these values are greater at  $\pm 30$  deg when compared to Nadir.



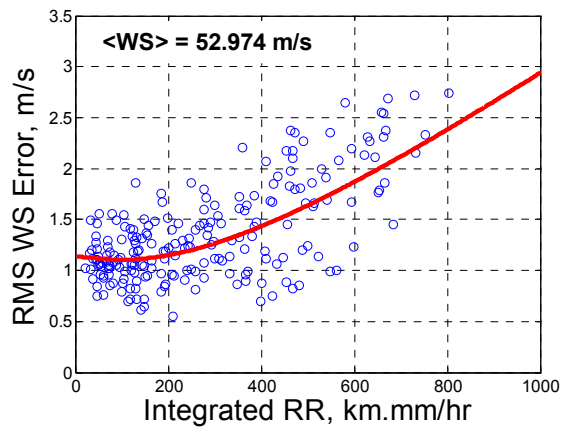
(a)



(b)

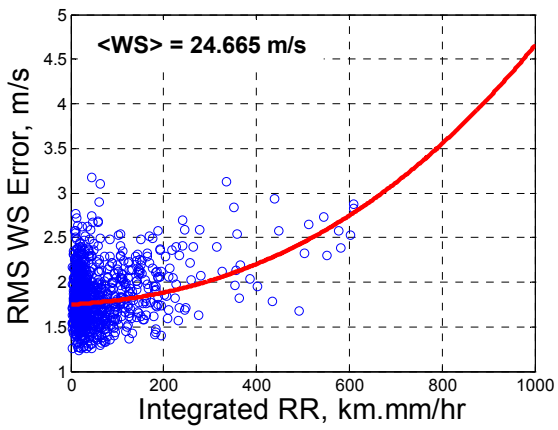


(c)

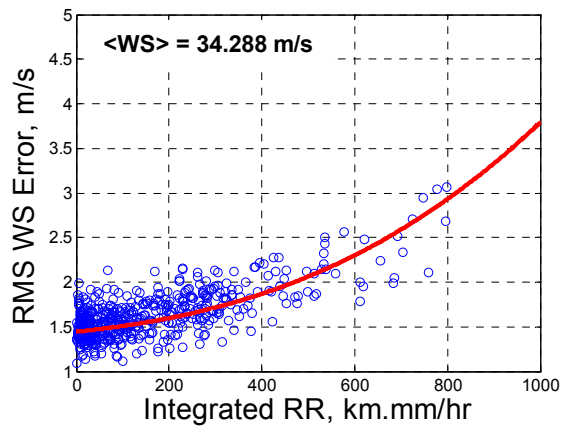


(d)

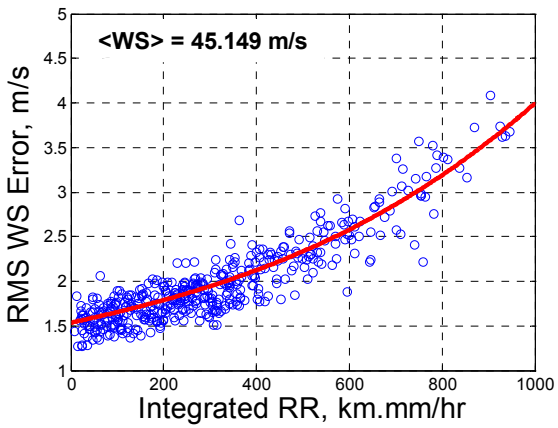
Figure. E.10 RMS wind speed errors (m/s) at  $\pm 30$  deg for four wind speed bins  $\pm 5$  m/s for 1 Kelvin random error.



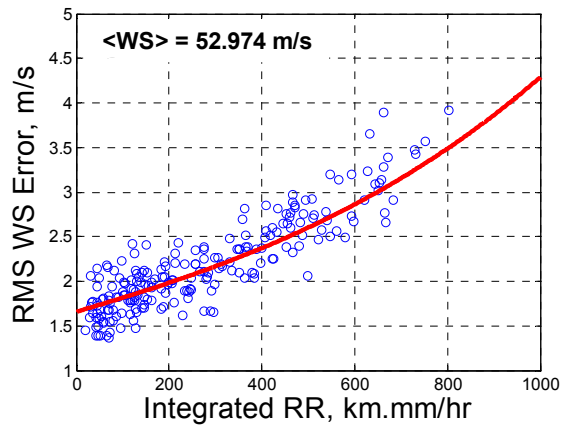
(a)



(b)

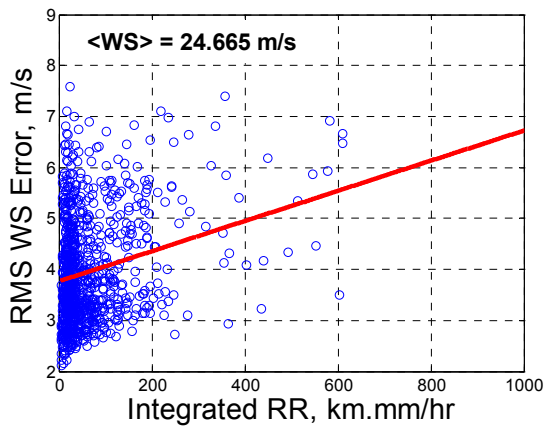


(c)

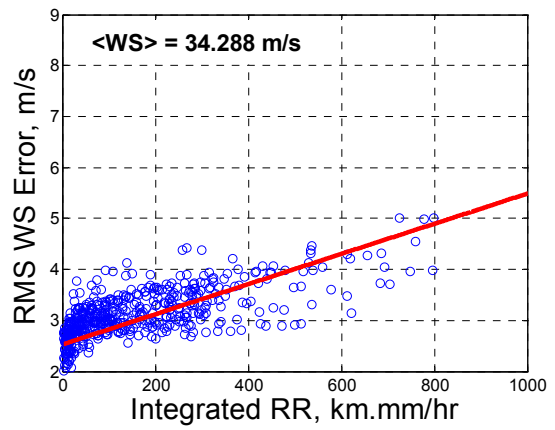


(d)

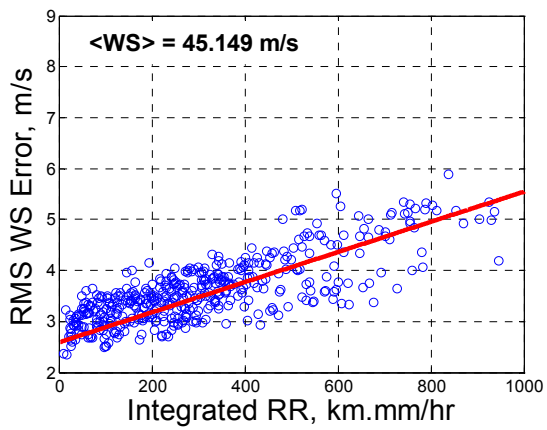
Figure. E.11 RMS wind speed errors (m/s) at  $\pm 30$  deg for four wind speed bins  $\pm 5$  m/s for 2 Kelvin random error.



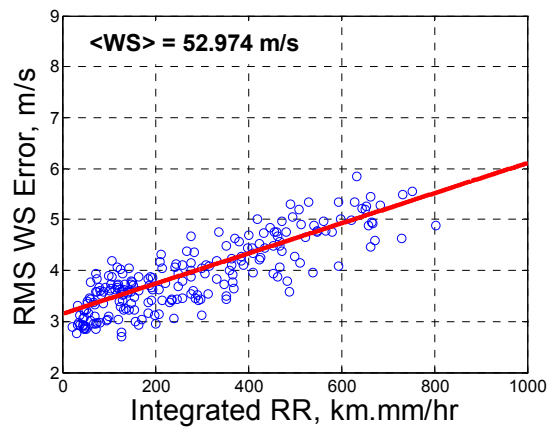
(a)



(b)

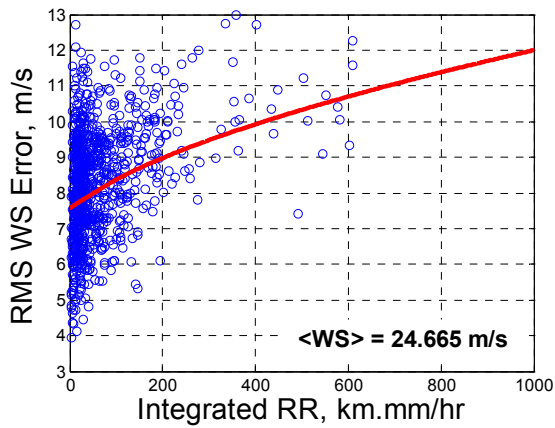


(c)

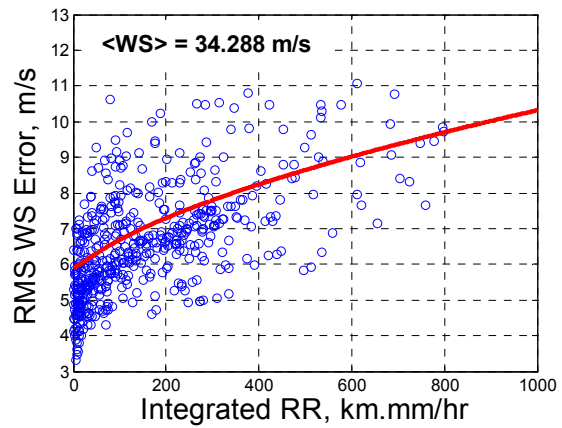


(d)

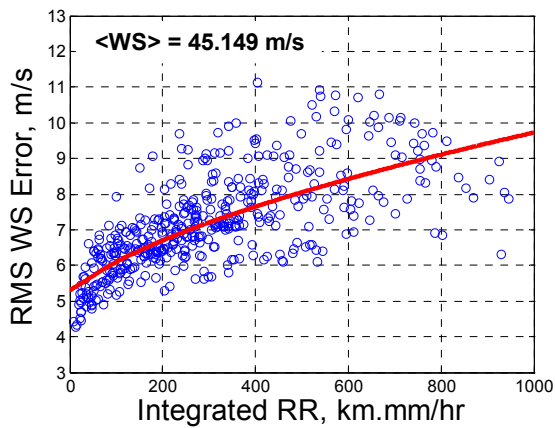
Figure. E.12 RMS wind speed errors (m/s) at  $\pm 30$  deg for four wind speed bins  $\pm 5$  m/s for 4 Kelvin random error.



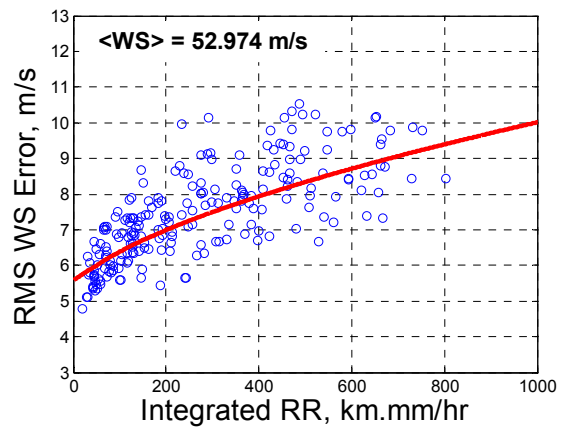
(a)



(b)



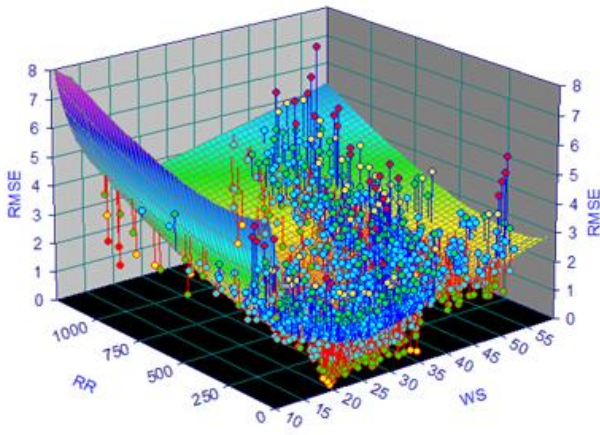
(c)



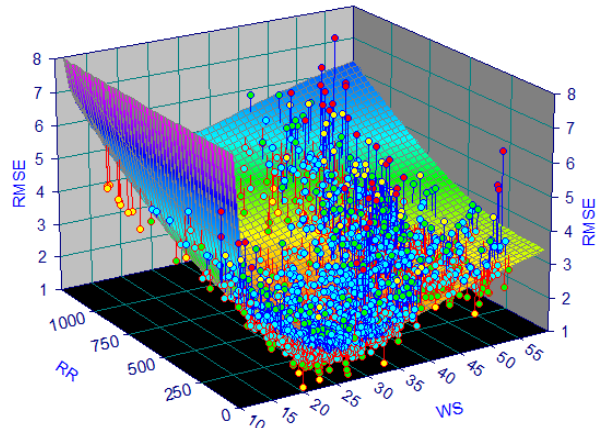
(d)

**Figure. E.13 RMS wind speed errors (m/s) at  $\pm 30$  deg for four wind speed bins  $\pm 5$  m/s for 8 Kelvin random error.**

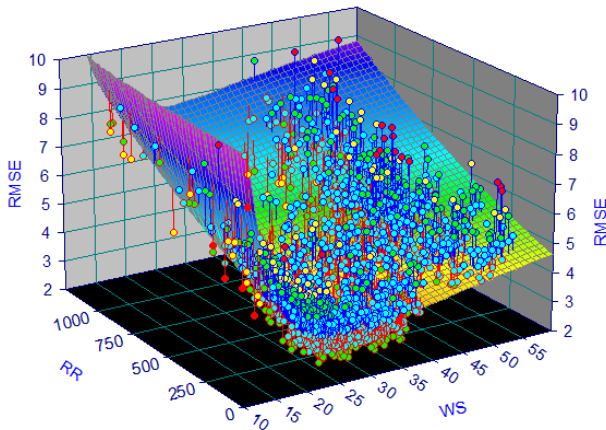
Figure E.14 shows the best surface fits to the RMSE wind speed values at  $\pm 60$  deg beam position for all random error values. As mentioned earlier, the RMS wind speed errors increase with increasing EIA, integrated rain rate and with wind speeds larger than about 30 m/s. At lower wind speed values, RMS wind speed errors are the greatest due to the random error effects that is dominant. Increasing the random error results in increased wind speed RMS error as expected.



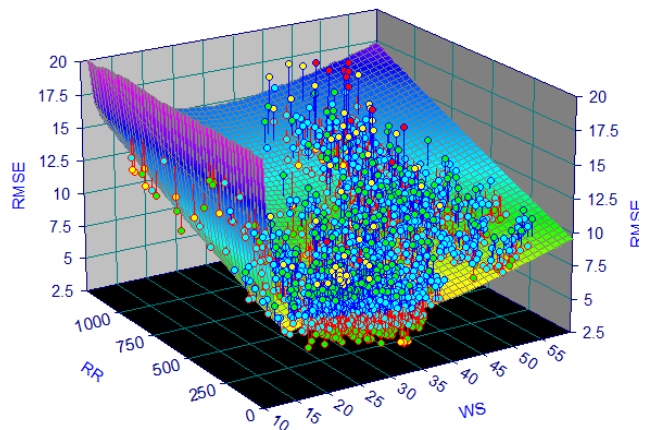
(a) 1 Kelvin



(b) 2 Kelvin



(c) 4 Kelvin

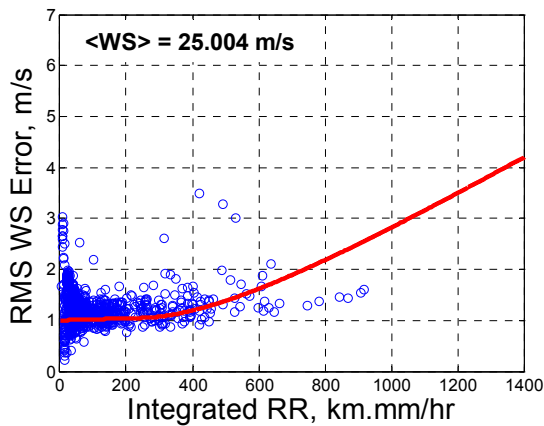


(d) 8 Kelvin

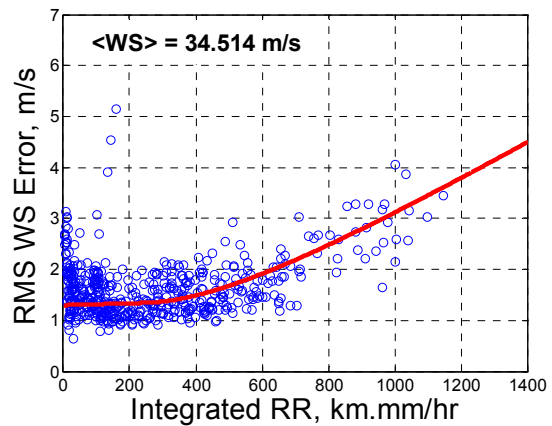
**Figure. E.14** RMS retrieved wind speed error surfaces at  $\pm 60$  deg for random error (a) 1 Kelvin, (b) 2 Kelvin, (c) 4 Kelvin and (d) 8 Kelvin.

The RMS wind speed errors were plotted for the  $\pm 60$  deg beam positions as a function of integrated rain rates for  $\pm 5$  m/s wind speed bins for random errors 1, 2, 4 and 8 Kelvin as shown in Fig. E.15, Fig. E.16, Fig. E.17 and Fig. E.18 respectively, with the red lines indicating the best surface fits to the points. At the edge of the swath, both the X-Pol and rain effects are the driver

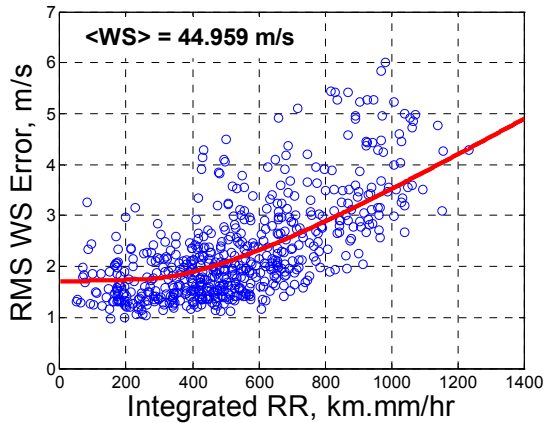
factors of the increased RMS wind speed errors. Again, the error increases with integrated rain rate and with wind speed values greater than 30 m/s. Increasing the random error results in increased wind speed RMS error as expected and these values are greater at  $\pm 60$  deg when compared to Nadir and  $\pm 30$  deg. The shape of the dependence of the error on wind speed and rain rate is similar at all EIAs.



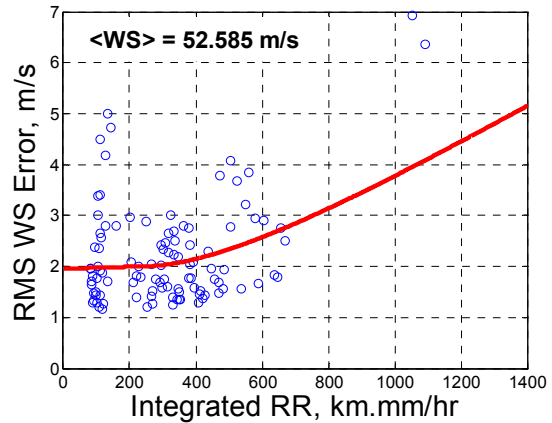
(a)



(b)

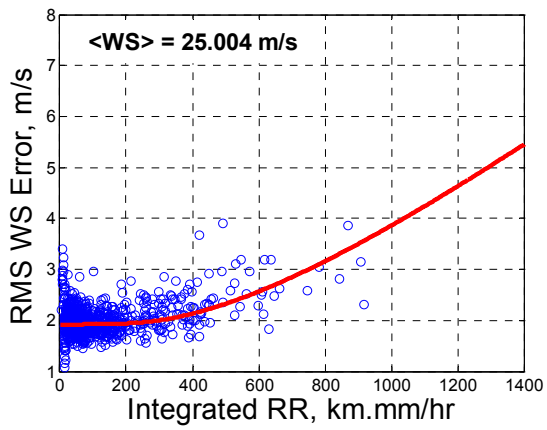


(c)

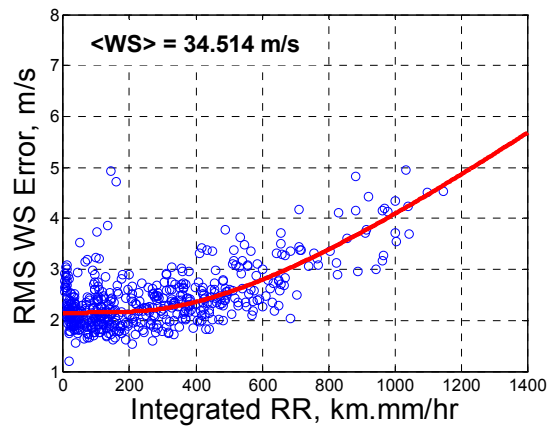


(d)

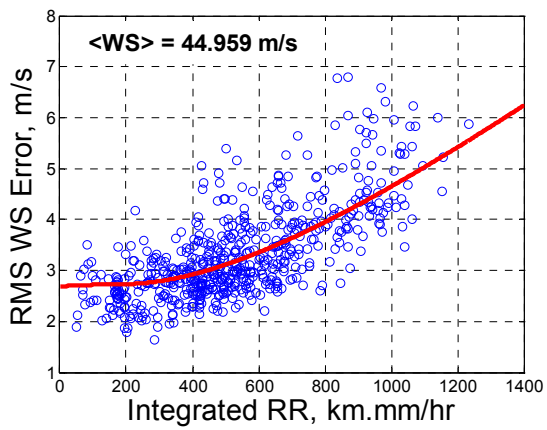
Figure. E.15 RMS wind speed errors (m/s) at  $\pm 60$  deg for four wind speed bins  $\pm 5$  m/s for 1 Kelvin random error.



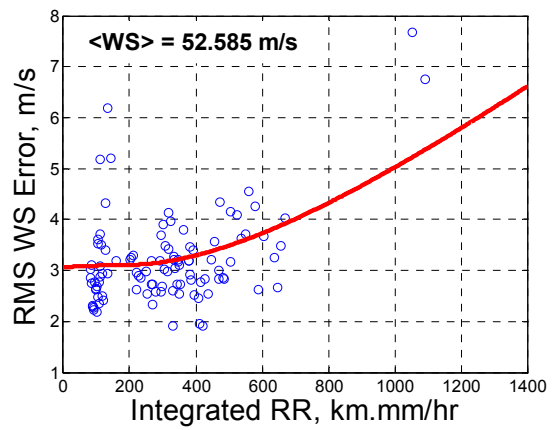
(a)



(b)



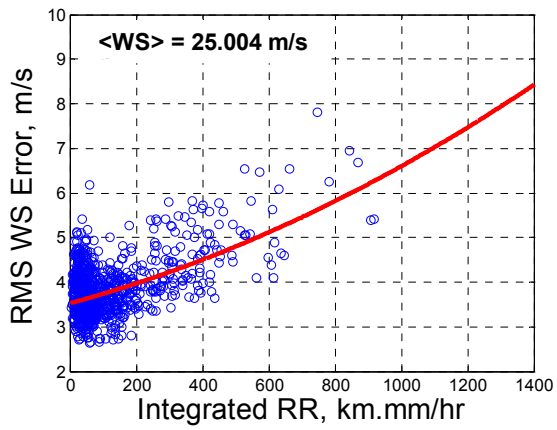
(c)



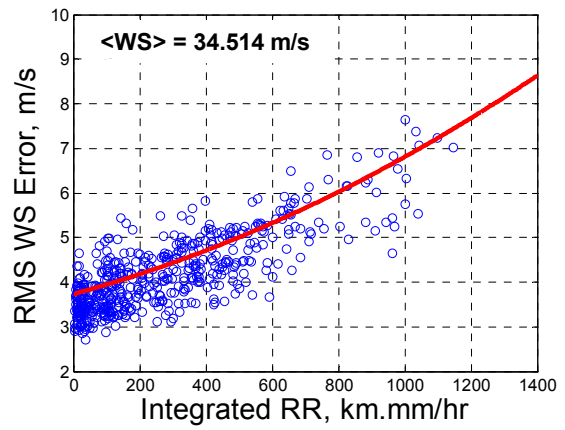
(d)

Figure. E.16 RMS wind speed errors (m/s) at  $\pm 60$  deg for four wind speed bins  $\pm 5$  m/s for 2 Kelvin random error.

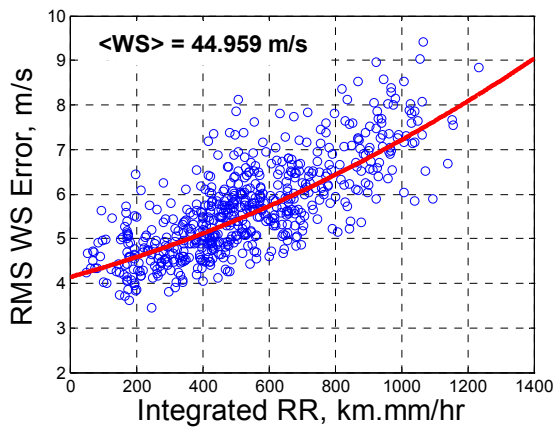




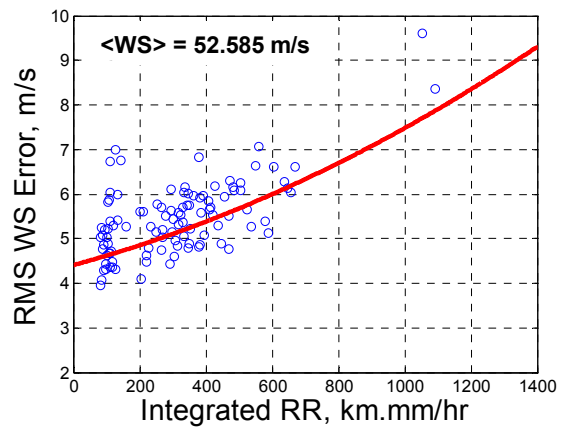
(a)



(b)

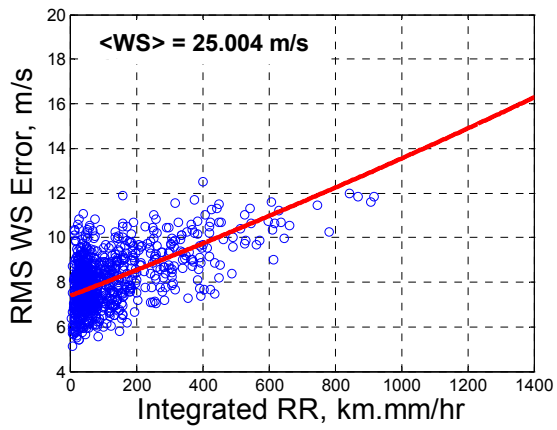


(c)

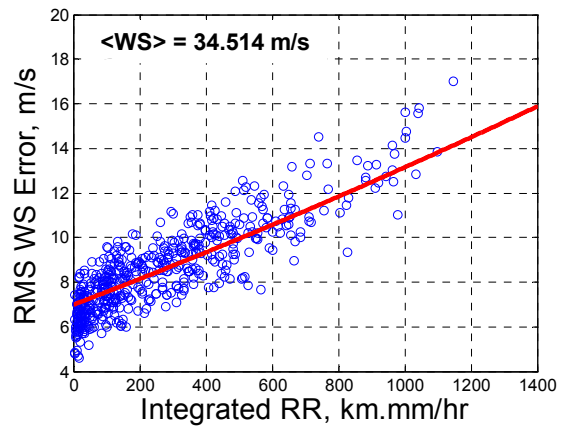


(d)

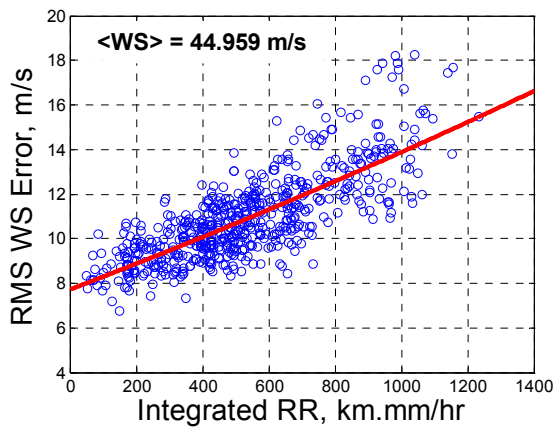
Figure. E.17 RMS wind speed errors (m/s) at  $\pm 60$  deg for four wind speed bins  $\pm 5$  m/s for 4 Kelvin random error.



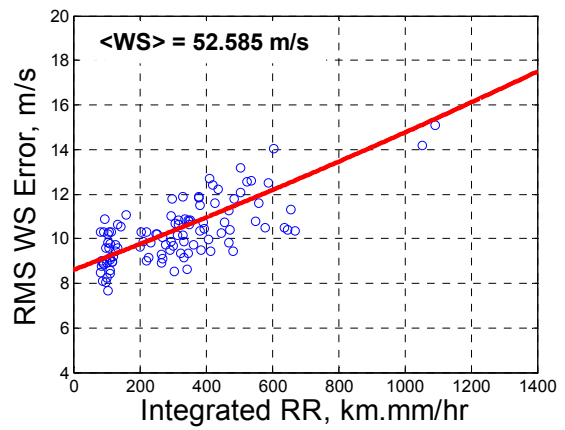
(a)



(b)



(c)



(d)

Figure. E.18 RMS wind speed errors (m/s) at  $\pm 60$  deg for four wind speed bins  $\pm 5$  m/s for 8 Kelvin random error.

## REFERENCES

- [1] E. W. Uhlhorn and P. G. Black, "Verification of Remotely Sensed Sea Surface Winds In Hurricanes," *J. Atmos. Oceanic Technol.*, pp. 100-115, 2003.
- [2] W. L. Jones, P. G. Black, V. E. Delnore, and C. T. Swift, "Airborne Microwave Remote-Sensing Measurements of Hurricane Allen," *Science*, vol. 214, pp. 274-280, 1981.
- [3] P. G. Black and C. T. Swift, "Airborne Stepped Frequency Microwave Radiometer Measurements of Rainfall Rate and Surface Wind Speed in Hurricanes," in *Second Conf. on Radar Meteorology*, Zurich, Switzerland, 1984, pp. 433-438.
- [4] E. W. Uhlhorn, P. G. Black, J. L. Franklin, and A. S. Goldstein, "Hurricane Surface Wind Measurements from an Operational Stepped Frequency Microwave Radiometer," *Mon. Wea. Rev.*, vol. 135, pp. 3070-3085, 2007.
- [5] J. W. Johnson, R. A. Amarin, S. F. El\_Nimri, W. L. Jones, and M. C. Bailey, "A Wide-Swath Hurricane Imaging Radiometer for Airborne Operational Measurements," in *International Geoscience & Remote Sensing Symposium*, Denver, Colorado, 2006.
- [6] C. Ruf, C. Principe, T. Dod, B. Gosselin, B. Monosmith, S. Musko, S. Rogacki, A. Stewart, and Z. Zhang, "Lightweight Rainfall Radiometer STAR Aircraft Sensor," in *International Geoscience & Remote Sensing Symposium*, Toronto, Canada, 2002, pp. 850-852.
- [7] C. Ruf and C. Principe, "X-Band Lightweight Rainfall Radiometer First Light," in *International Geoscience and Remote Sensing Symposium*, Toulouse, France, 2003.
- [8] D. M. L. Vine, A. J. Griffis, C. T. Swift, and T. J. Jackson, "ESTAR: A Synthetic Aperture Microwave Radiometer for Remote Sensing Applications," in *Proceedings of the IEEE*, 1994.
- [9] F. T. Ulaby, R. K. M. Moore, and A. K. Fung, *Microwave Remote Sensing, Active and Passive* vol. 1. Norwood, MA: Artech House Inc, 1981.
- [10] S. F. El-Nimri, W. L. Jones, E. Uhlhorn, C. Ruf, J. Johnson, and P. Black, "An Improved C-Band Ocean Surface Emissivity Model at Hurricane-Force Wind Speeds over a Wide Range of Earth Incidence Angles," *IEEE Geoscience and Remote Sensing Letters*, 2010.
- [11] A. B. Tanner and C. T. Swift, "Calibration of a Synthetic Aperture Radiometer," *IEEE Transactions on Geoscience and Remote Sensing*, vol. 31, pp. 257-267, 1993.
- [12] M. C. Bailey, R. A. Amarin, J. Johnson, P. Nelson, M. James, D. Simmons, C. Ruf, W. L. Jones, and X. Gong, "Multi-Frequency Synthetic Thinned Array Antenna for the Hurricane Imaging Radiometer," *IEEE AP-S Transactions on Antennas and Propagation*, 2010.
- [13] D. P. Jorgensen and P. T. Willis, "A Z-R Relationship for Hurricanes," *Journal of Applied Meteorology*, vol. 21, pp. 356-366, 1982.
- [14] R. L. Olsen, D. V. Rogers, and D. B. Hodge, "The aRb Relation in the Calculation of Rain Attenuation," *IEEE Trans. Antennas Propagat.*, vol. 26, pp. 318-329, 1978.
- [15] L. Hong, "Inter-Satellite Microwave Radiometer Calibration," in *Electrical Engineering and Computer Science*. vol. Ph.D. Orlando: University of Central Florida, 2008.
- [16] S. S. Chen, J. F. Price, W. Zhao, M. A. Donelan, and E. J. Walsh, "The CBLAST-Hurricane Program and the Next-Generation Fully Coupled Atmosphere-Wave-Ocean

- Models for Hurricane Research and Prediction," *Bull. Amer. Meteor. Soc.*, vol. 88, pp. 311-317, 2007.
- [17] P. T. Willis, "Functional Fits To Some Observed Drop Size Distributions and Parameterization of Rain," *Journal of the Atmospheric Sciences*, vol. 41, pp. 1648-1661, 1984.
- [18] T. Meissner and F. J. Wentz., "The Complex Dielectric Constant of Pure and Sea Water from Microwave Satellite Observations," *IEEE Transactions on Geoscience and Remote Sensing*, vol. 40, pp. 1836 - 1849, 2004.
- [19] B. H. Lim, R. A. Amarin, S. F. El-Nirmi, J. Johnson, W. L. Jones, and C. Ruf, "Restrictions on the Field of View for an Under Sampled 1-D Synthetic Thinned Aperture Radiometry," in *International Geoscience & Remote Sensing Symposium*, Barcelona, Spain, 2007.
- [20] S. F. El-Nimri, S. O. Alswiss, W. L. Jones, E. Uhlhorn, and J. Johnson, "Hurricane Imaging Radiometer Wide Swath Simulation for Wind Speed and Rain Rate," in *International Geoscience & Remote Sensing Symposium*, Boston, MA, 2008.
- [21] R. A. Amarin, S. F. El-Nimri, J. W. Johnson, W. L. Jones, B. H. Lim, and C. S. Ruf, "Instrument Design Simulations for Synthetic Aperture Microwave Radiometric Imaging of Wind Speed and Rain Rate in Hurricanes," in *International Geoscience & Remote Sensing Symposium*, Barcelona, Spain, 2007.
- [22] C. A. Balanis, *Antenna Theory: Analysis and Design*, 2 ed.: John Wiley and sons, inc., 1997.
- [23] M. M. a. Wisler and J. P. Hollinger, "Estimation of Marine Environmental Parameters Using Microwave Radiometric Remote Sensing Systems," DOC/NOAA/ERL/WPL, Wash. D.C Nov. 1977.
- [24] E. P. Gross, "Shape of Collision-Broadened Spectral Lines," *Phys. Rev.*, vol. 97, pp. 395-403, January 15 1955.